HIGH DENSITY BIMODAL PARTS BY THREE DIMENSIONAL PRINTING

by

Akan E. Oton

B.S. Mechanical Engineering
Columbia University, 1996

Submitted to the Department of Mechanical Engineering in Partial Fulfillment of the Requirements for the Degree of

MASTER OF SCIENCE IN MECHANICAL ENGINEERING

at the

Massachusetts Institute of Technology

June 1998

Signature of Author _____
Department of Mechanical Engineering
May 26, 1998

Certified by _____
Emanuel M. Sachs
Professor of Mechanical Engineering
Thesis Supervisor

Accepted by _____
Ain Sonin, Chairman
Graduate Committee, Department of Mechanical Engineering

HIGH DENSITY BIMODAL PARTS BY THREE DIMENSIONAL PRINTING

by

Akan E. Oton

Submitted to the Department of Mechanical Engineering on
May 26, 1998 in partial fulfillment of the requirements for the
Degree of Master of Science in Mechanical Engineering

ABSTRACT

Three Dimensional Printing (3DP) is a rapid prototyping process that allows for the fabrication of injection molding tooling from computer generated models. Due to market demands for harder, more robust tooling, improving the material properties and the geometric control of 3DP parts has been a necessary goal of the project. One path to accomplishing this task is to increase the green density of the 3DP compact prior to sintering. To accomplish this goal, the printing of fine, sub-micron Titanium Carbide slurries into a large powder bed to create a dense bimodal compact was investigated.

Experiments performed demonstrated that a uniform, defect free microstructure could be obtained by appropriately selecting 3DP process parameters. By spreading 4 mil layers, and double printing, sample coupons with estimated green densities of up to 83% were obtained. In addition, the effect of varying either the bimodal concentrations or the relative particle sizes, on fine porosity in 3DP parts after infiltration was studied.

Three bimodal ceramic-metal material systems, each based on Titanium Carbide and subsequently infiltrated with a copper-nickel-manganese alloy, were also developed. The first system, a bimodal system of large TiC and fine TiC powders exhibits good dimensional control (net shrinkage of 0.2%) and age-hardening properties (up to 43 HRC). The second system, a bimodal system of large Stainless Steel and fine TiC powders, is characterized by modest dimensional control (less than 2%), but does not exhibit any age-hardening behavior. The third system developed, a bimodal system of large Molybdenum powders and fine TiC powders, can be hardened up to 25 HRC with a 12 hour, 400°C treatment.

Thesis Supervisor: Emanuel Sachs

Title: Professor of Mechanical Engineering

ACKNOWLEDGEMENTS

I would like to express my thanks to the National Science Foundation and the members of the Three Dimensional Printing Consortium for supporting my research efforts at MIT.

In addition, I would like to single out individuals who, through their extraordinary efforts, have enriched my experience at MIT.

Emanuel Sachs, for teaching me that larger ideas spring forth from *simple* observations. Your guidance has made me a better engineer.

Sam Allen, for lending your keen insight into material science and physical metallurgy.

Jim Serdy, for seeing the world the way I wish I could ... the way we all probably should.

Dave Brancazio, the resident electronics wiz. I never had a question that you couldn't answer.

Fred Cote, Gerry Wentworth, Lenny Rigione and Laura Zaganjori, I couldn't thank each of you enough for all the times you made my job easier and more fun.

Ako Chijioke, Vedran Knezevic, Adam Lorenz, during the two years and change, it was always a pleasure.

To the rest of the 3DP gang, Costas, Pat, Bjorn, etc. I wish you success in all your endeavors.

TABLE OF CONTENTS

LIST OF FIGURES

Chapter 1

Chapter 2

Chapter 3

Chapter 4

Chapter 5

Chapter 6

Appendix B

LIST OF TABLES

Chapter 2

Chapter 3

Chapter 4

Chapter 5

Appendix B

Chapter 1: Introduction

1.1 Background

1.1.1 The Basic 3DP Process

Three Dimensional Printing (3DP) is a serial manufacturing process in which complex geometric parts are systematically created, layer by layer, in a repeating sequence of steps (Sachs, et. al). These steps are illustrated in figure 1.1. In each sequence, loose powders are spread on a piston, selectively joined by binder material deposited from a print head, and the piston lowered for a subsequent layer to be spread. The result is a "green" compact, with only the binder material maintaining the integrity of the geometry. This is the basic 3DP process.

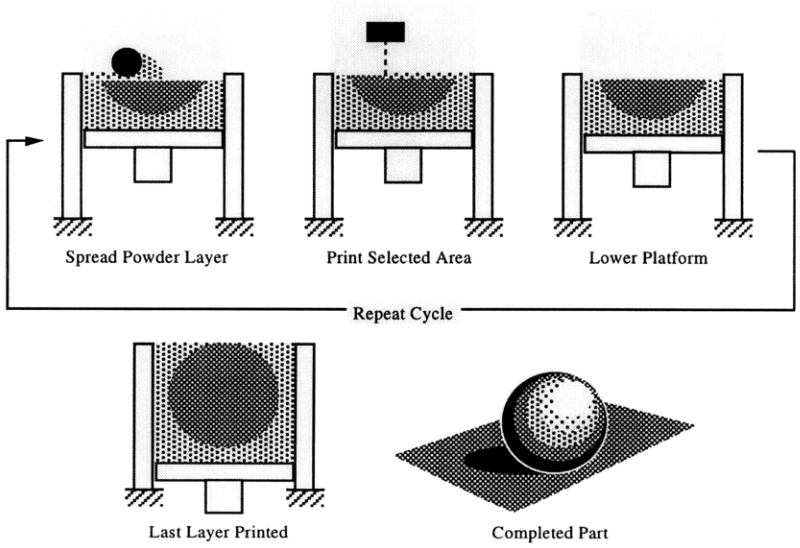

Figure 1.1 3DP Process Overview; (Courtesy Tailin Fan, 16).

1.1.2 Process Advantages

The main advantage of the 3DP process is its adaptability to multiple material systems. Essentially, parts can be produced from any materials that are commercially available as powders.

1.1.3 3DP Process Applications

A major application of the 3DP process, is the fabrication of tool sets for casting and injection molding purposes. These tools sets, typically stainless steel (sample tool image Figure 1.2), require significant post processing operations to impart the desired strength, hardness and toughness necessary for industry, while still maintaining the dimensional control achieved during the basic 3DP process.

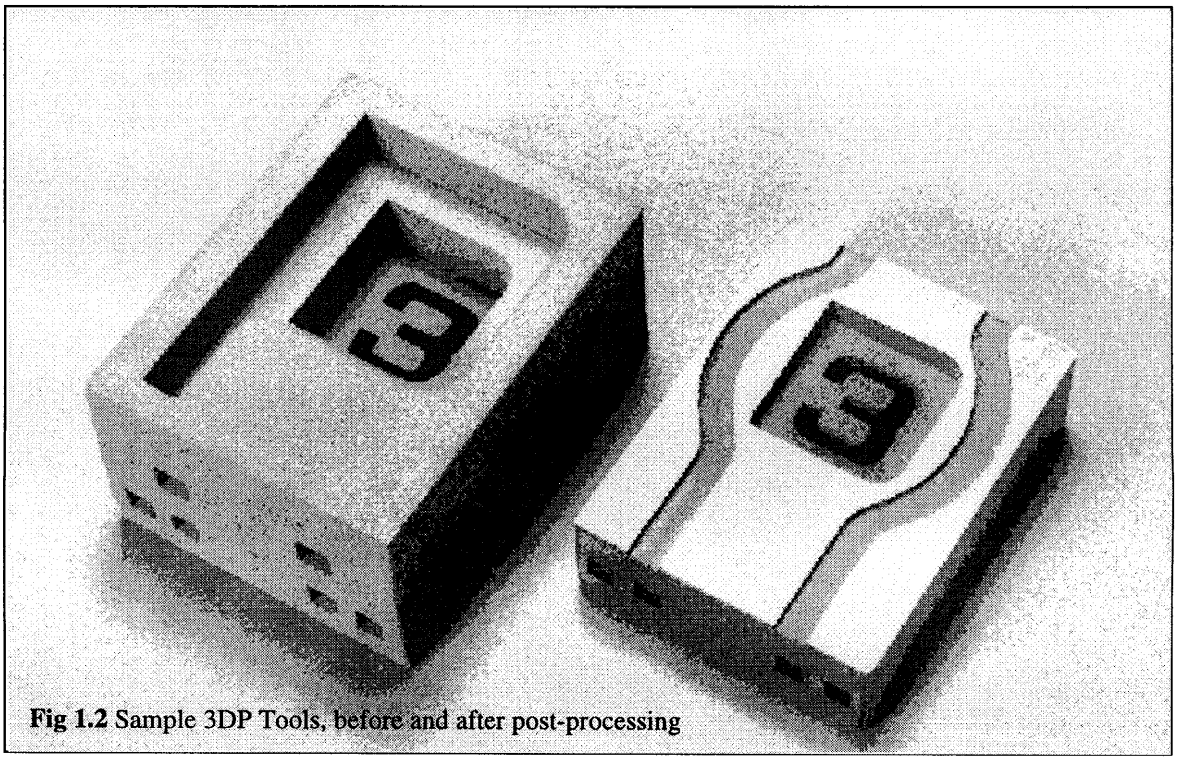

Fig 1.2 Sample 3DP Tools, before and after post-processing

1.2 3DP Post Processing at a glance

The post processing operations (Figure 1.3): sintering, infiltration, etc. adversely alter the initial geometry created during the basic 3DP process and hinder adequate control of critical dimensions.

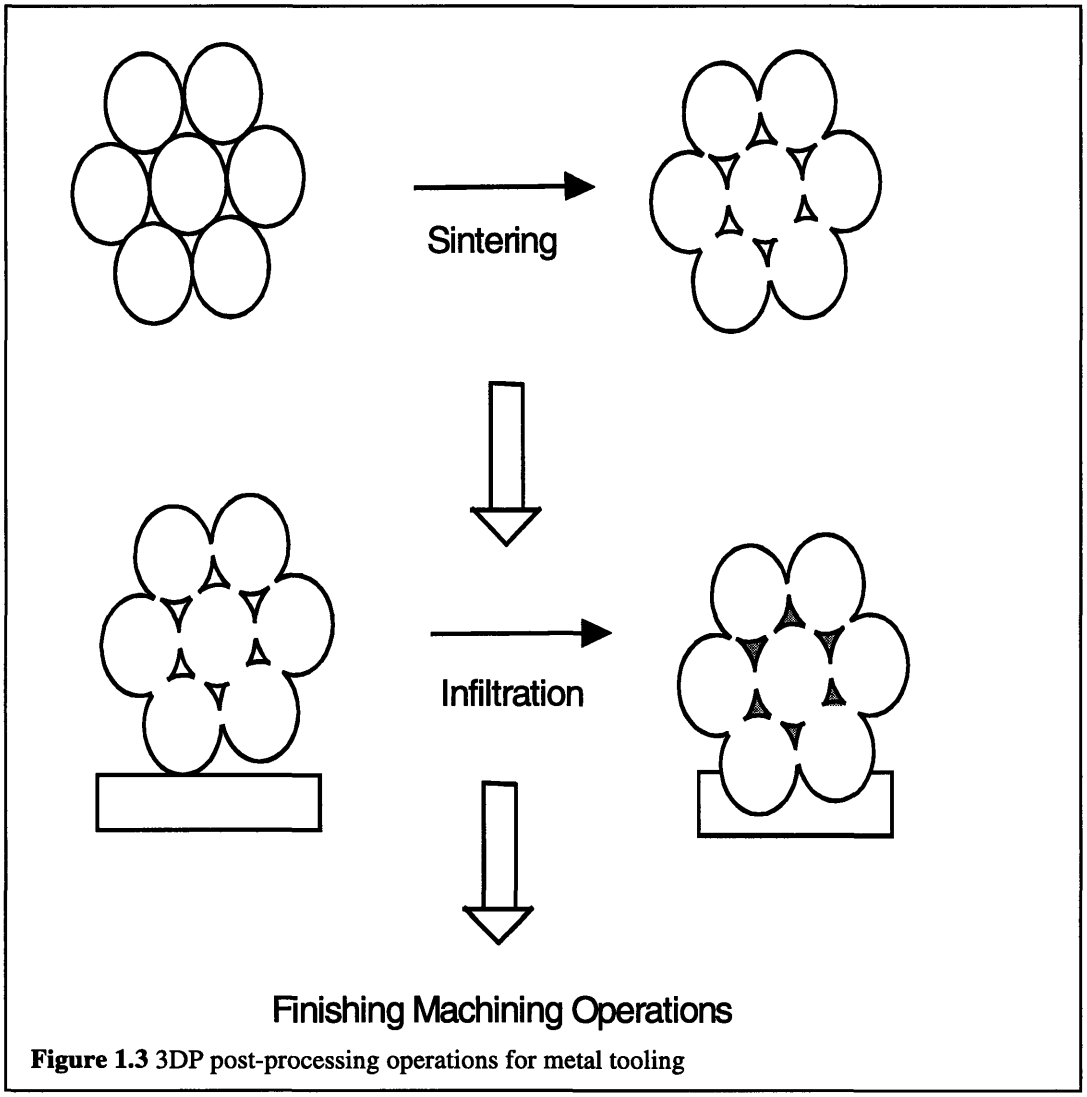

Figure 1.3 3DP post-processing operations for metal tooling

During the sintering stage, the temperature of the green compact is elevated to not only burn out the binder material but also to allow the powders to touch, diffuse across their boundaries and form strong bonds or "necks". Though the sintering and neck formation occurs at temperatures below the compact's melting point, it results in significant

shrinkage of the compact. This shrinkage is due to the neck formation that draws the powders closer as they grow.

In the subsequent infiltration step, the sintered compact is brought into contact with a molten metal (typically bronze) at elevated temperature. As a result of capillary pressure, the liquid metal infiltrates or fills the voids within the porous body. Frequently, there is a small amount of expansion associated with the infiltration step.
Following infiltration, the 100% dense body can be finished as desired via electrode-discharge machining (EDM) or other machining processes, and if necessary, heat treated.

1.3 Motivation & Goals

Due to market demands for harder, more robust tooling, improving the material properties and the geometric control of 3DP parts has been a necessary goal of the project. One path to accomplishing this task is to increase the density of the 3DP compact prior to sintering. Higher starting densities would minimize the effect of geometry altering post-processing operations and ensure a harder tool. Currently, a green density of sixty percent is the highest level possible. As a target, a seventy percent dense green body was selected as the goal of this work.

1.4 Paths to Increase Green Density

In order to achieve the desired goal of higher green densities, the work of Steve Gregorski was drawn heavily upon. Gregorski identified several paths as possible means of increasing green part density (71-75). They include (1) Spreading of bimodal powders (2) Alternative spreading & compaction techniques (3) Printing or spraying fine powder slurries to fill the void space and if possible, also serve as binder material. A slurry is a dispersion of fine powders in a liquid vehicle.

The spreading and compaction of bimodal powders was investigated by Gregorski with some success. However, the parts produced had significant interlayer defects. An interlayer defect is the absence of large powders at the interface between layers, creating an increased risk for crack propagation and eventual failure during use. Gregorski recognized this problem but was unable to eliminate the segregation of fines from larger powders during spreading and packing that caused the defects (See figure 1.4).

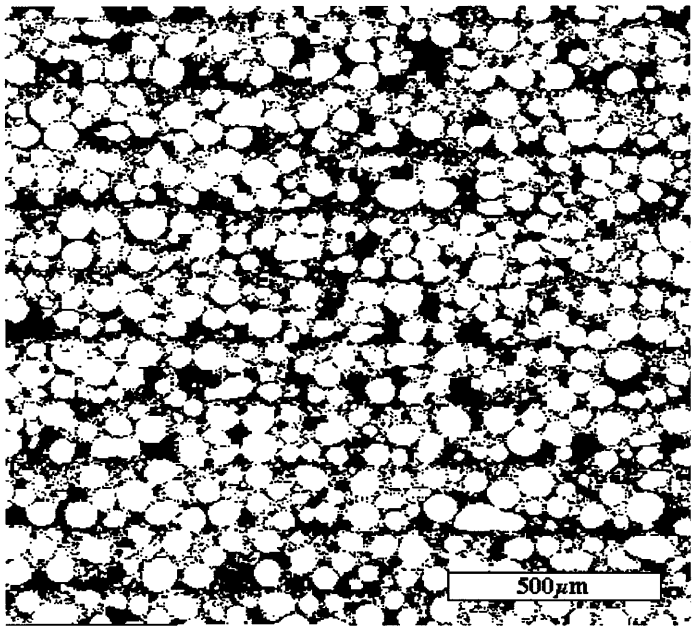

Figure 1.4 Microstructure of 71/9 μm printed bimodal baseline sample. (Courtesy: Steve Gregorski, 40)

1.4.1 The Slurry Printing Path

As a starting point, the printing and spraying of fine powder slurries was identified as a likely means of increasing green part density while minimizing the segregation of fine powders from larger powders and producing a homogeneous body. This would occur if the slurry penetrated multiple layers during each application, filling the voids in several layers and not just the recently spread layer. The benefits of multiple layer penetration would be dual: (1) to minimize any periodicity associated with spreading a powder because the penetration depth would be greater than the spread layer thickness, and (2) to eliminate segregation and settling because the fine powders would not be spread or stored.

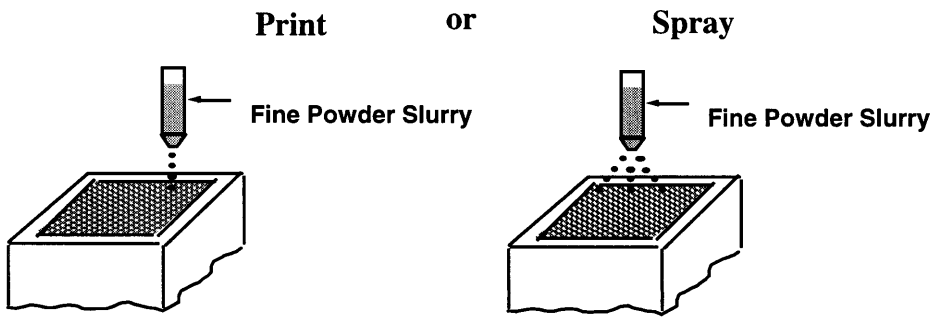

Figure 1.5 Slurry based fine powder deposition approaches.

Slurry printing had the added advantage of being readily integrated into the existing 3DP process. Furthermore, with slurry printing, control of the final part composition on a localized level was possible. As such, a wider variety of applications for 3DP would be possible.

Printing fine powders also had the potential of reducing the shrinkage associated with the high temperature post processing operations (firing, infiltrating etc) if an inert powder was used, filling void space and increasing density. This shrinkage reduction would be quite notable if the inert component had a *significantly* higher melting point than the base powder and would resist the base material's tendency to shrink during sintering. Titanium carbide, because of its higher melting point than stainless steel grades used in the process, suited quite nicely. This technique of reducing shrinkage was explored by Helen Yoo with some success. Yoo used small amounts of titanium carbide to inhibit the shrinkage of 3DP parts bonded with iron carbonyl (73-85).
The decision to use Titanium Carbide as the printed particle also opened up the possibility of fabricating Cermets, or ceramic-metal composites, with the 3DP process.

As such, the printing of fine powders seemed to offer the beneficial density improving effect of using bimodal powders, without the adverse segregation effects encountered by spreading a bimodal mixture.

1.4.2 Issues Associated with Printing Slurries

Despite the obvious benefits associated with printing fine slurries, pursuing this path raised several basic questions:

1) How would the printing be undertaken, i.e. should we print in multiple passes and/or dry between passes?
2) What ultimate green density could we reach?
3) Where would the fine powders end up? Would they end up at the junctions between powder and how would this affect sintering? Would we see similar interlayer defects that Gregorski had noted?
5) How do we bind the part? Do we sinter the fine powders or do we add an additional binding agent?
6) How do bimodal mixtures infiltrate (assuming a non-reactive system)? Is there any trapped gas phenomena? How would the varying infiltration rates of large and fine powders affect the resulting part? What is the effect of local density changes on infiltration?

To answer these questions, a case study or model system approach was used were ever possible. However, the analysis and conclusions reached are intended to be general enough to be applicable to other 3DP systems.

1.5 Thesis Organization

A brief synopsis of the organization of this thesis is as follows:

Chapter 2: Modeling Bimodal Densification by Slurry Printing – Serves as a discussion of process modeling issues including densification effects due to bimodal mixtures and slurry printing models.

Chapter 3: Development of Titanium Carbide Slurries - A summary is presented of the work involving slurry characterization, jetting experiments, and slurry formulation.

Chapter 4: Slurry Printing Deposition Patterns - Further Study of Bimodal Densification via slurry printing with emphasis on fine particle deposition, infiltration of bimodal parts, and a systematic study of printed bimodal coupons.

Chapter 5: Development of Bimodal Systems – Summary of the materials development of three bimodal systems based on Titanium Carbide. The sintering and infiltration of these systems is discussed at length. Shrinkage and Macro Hardness characterization are also included.

Chapter 6: Conclusions – A summary of research conclusions is presented and ideas for future work are presented.

Appendices: Appendix A is a database of powders used in the course of this work. Appendix B is a summary of the sintering map technique use to predict shrinkage in sintered TiC compacts.

Chapter 2: Modeling Bimodal Densification by Slurry Printing

2.1 Bimodal Packing Models

2.1.1 Traditional Bimodal Modeling

Traditional modeling of bimodal powders has been idealized as the uniform packing of two disparate sized monomodal spherical powders. As illustrated in figures 2.1a and 2.1b, the smaller monomodal powders evenly fill the void space between the larger powders, and as such increase the density of the compact.

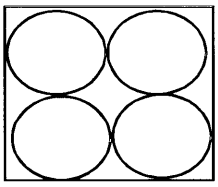

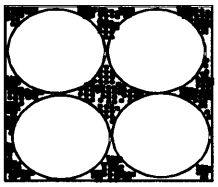

Figure 2.1 a) Monomodal mixture **b)** Bimodal mixture

In this idealization, the smaller particles fit neatly into the void space without altering the position or spacing of the larger particles. As such, maintaining the spacing between the larger particles is key to realizing a higher pack density. Using significantly finer small particles is the most efficient means of ensuring that the spacing between large particles remains unaltered.

2.1.1.1 Calculation of Bimodal Packing Fraction (Traditional Model)

To calculate the theoretical packing fraction of a bimodal mixture, you need to know the packing fractions of the individual monomodal distributions. The packing fraction is defined as the actual percent of a given volume that the powders occupy. The bimodal fraction is defined as follows:

$$\phi_{Bimodal} = \phi_l + \phi_s(1-\phi_l) \qquad 2.1$$

Here $\phi_{Bimodal}$, ϕ_l, and ϕ_s refer to the packing fractions of the bimodal mixture, large powders, and small powders respectively.

For practical purposes however, expressions that relate the packing fraction of the monomodals to their mass fractions and bulk densities are more useful.

$$v_l = \frac{\rho_l \phi_l}{\rho_l \phi_l + \rho_s \phi_s (1 - \phi_l)} \qquad 2.2$$

$$v_s = 1 - v_l \qquad 2.3$$

Here v_l, v_s, ρ_l, ρ_s refer to the mass fractions and density of the large and small powders respectively. The mass fraction of a particular component in a mixture is the ratio of the component's mass to the total mass of the mixture.

2.1.1.2 Optimal Bimodal Concentrations (Traditional Model)

The traditional bimodal framework allows us to predict the optimal concentration ratio of large particles to small particles. Implicit in this prediction is the assumption of an infinite difference in the average particle sizes of the monomodals. This to ensure that there is no alteration in the spacing between the larger powders that would inhibit densification. However, German has relaxed this specification to a particle size ratio of at least 7:1 (170). For idealized spherical powders of similar densities, with a pack density of 63.7%, equations 2.2 and 2.3 predict an optimal concentration of 73.44% large particles and 26.56% small particles. This translates to a maximum packing fraction of 86% for spherical bimodal mixtures.

2.1.2 Bimodal Modeling of Densification via Slurry printing

Unfortunately, the traditional model fails to be an accurate representation of the process if the bimodal distribution is not formed by mixing two monomodal powder distributions simultaneously.

To develop an adequate model of bimodal mixtures achieved by printing fine powder slurries into a base powder, it is necessary to consider the printed region (Figure 2.2).

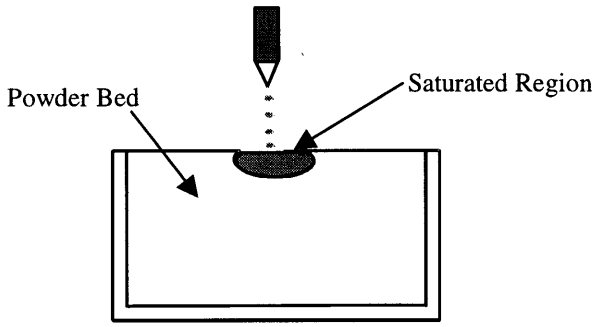

Figure 2.2 Idealization of Saturated region during Printing

The resulting packing density in the printed region can be expressed as follows,

$$\phi_{Bi\,\mathrm{mod}\,al} = \phi_l + f \cdot \phi_{pr\,\mathrm{int}} \qquad 2.4$$

were f is the volume fraction of solid particles in the slurry and ϕ_{print} is the ratio of the volume of slurry printed to the total volume of the printed region.

Assuming that the printed region is fully saturated by the slurry and that the deposition of fine powders is uniform, equation 2.4 readily simplifies, giving us an initial estimate of the densification achievable via slurry printing.

$$\phi_{Bi\,\mathrm{mod}\,al} = \phi_l + f \cdot (1 - \phi_l) \qquad 2.5$$

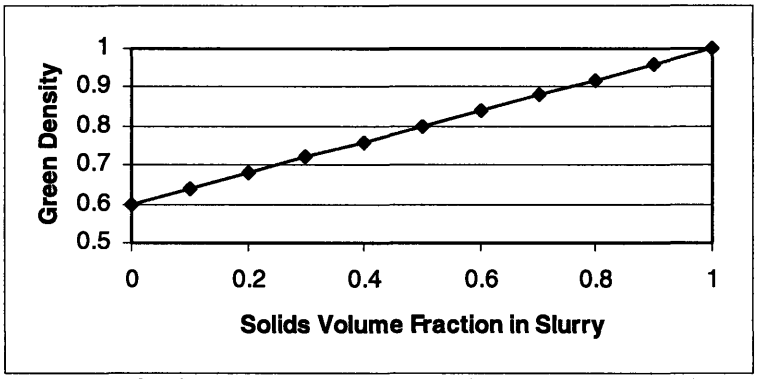

Figure 2.3: Plot of estimated Green density as a function the volume fraction of solid particles in a slurry, assuming a monomodal packing fraction of 0.60 and a saturated powder bed.

Figure 2.3 also shows how this estimate of the resulting packing fraction varies with the volume fraction of solids in the slurry. This figure is plotted for a spherical powder with a monomodal packing fraction of 0.60, the typical 3DP situation.

The green densities estimated in figure 2.3 are quite low, and require quite high solids loading before significant densification is achieved. Prior experience with tungsten carbide slurries led to the view that solid volume percentages on the order of 30- 40% were quite high (Caradonna, 124-154). Using this as a guide, a maximum fractional density of only 73-80% could be expected. Much less than the estimate of 86% fractional density attained using the traditional bimodal model.

Luckily, expression 2.5 and figure 2.3 do not take into account densification that can be achieved by printing in multiple passes and subsequently drying at each layer. More significantly, they fail to consider the fact that in the 3DP process it is possible to print into previously spread layers if the penetration depth of the slurry is greater than the layer thickness. As such, further densification could be achieved than the levels predicted by expression 2.5 and figure 2.3.

2.1.2.1 Characterization of Particle Deposition using a Model System

This ability to print into multiple layers and in multiple passes was an obvious key to significantly increasing the fractional density of 3DP parts via slurry printing. However, to incorporate these effects into a model, it was necessary to determine a characteristic or generic profile for the slurry deposition as a function of depth. The shape of this curve, it was felt, would be fairly material independent and be widely applicable. Only parameters such the magnitude of the concentration, penetration depth etc. would depend on the wetting characteristics and rheology of the slurry and the base powder.

Following this line of reasoning, glass beads and alumina slurries were selected as a model system for determining this characteristic profile. Soda lime glass beads were selected because of they would be the closest commercially available realization of perfect spheres and were available over a wide range of sizes. Alumina slurries were selected because they had been extensively studied by the 3DP group in previous years and their characteristics were well understood. Another important factor in the selection of glass and Alumina, was the density difference between the two (Alumina = 4.99 gm/cc, Glass = 2.45 gm/cc). This density difference was critical because the experiment as conceived would involve weighing thin slices of a sintered powder bed and back calculating the various weights of the constituents. The significantly larger density of alumina would increase the sensitivity of the experiment to detecting the presence of alumina in the bed.

2.1.2.1.1 Experimental Setup to Determine Slurry Deposition Profile

The particulars of the experiment are as follows. A 20 volume % alumina slurry (0.5 μm average particle size) was jetted through a 120 μm nozzle, in a continuous stream, into a spheriglass© powder bed (42 μm average particle size). The nozzle was then rastered across the entire powder bed in adjacent lines to evenly deposit alumina onto the bed. The flow rate and line spacing was set sufficiently high to saturate the bed to a depth of at

least 1 mm, to produce a sample of decent thickness. The thickness was in fact observed to be larger (about 2-3 mm), due to the penetration of the slurry.

The glass-alumina powder bed was subsequently fired in a tube furnace at 700°C for 10 minutes. This was done to trap the alumina particles in the glass matrix and create a rigid structure. The temperature was chosen because it was significantly below the softening point of the glass and approximately at the onset of sintering of the glass powders. This minimized possible dimensional changes and shifting of particles. The resulting porous compact demonstrated adequate strength and could be handled.

After sintering, the compact was slowly dipped into a bath of liquid Techwax© at elevated temperature (90°C). The wax wicked into the compact, filling the remaining voids. A 2 x 2 cm square portion of the infiltrated body was then encased in epoxy to allow for easy handling and fixturing. The square sample was then placed in an Okamoto precision grinder for subsequent machining. The grinder allowed for material to be removed with a depth of cut as small as 0.00001 inches. Systematically, cuts of 0.0012 inches were made and the remaining sample weighed. Thus, the weight of the compact was determined as a function of depth. A simple difference was then taken between subsequent measurements to obtain the weight of each slice. With this information, it was relatively straightforward to back calculate the concentrations of glass, alumina and wax in the compact.

2.1.2.1.2 Determination of Constituent Concentrations

The total weight in a single slice could be expressed as the sum of the individual weights of the constituents, which could in turn be expressed in terms of the relative volume fractions:

$$W = \rho_a f_a V + \rho_g f_g V + \rho_w f_w V \qquad 2.6$$

were ρ_a, ρ_g, ρ_w, f_a, f_g, f_w are the densities and volume fractions of alumina, glass and wax in the sample. V is the total volume of the slice.

The volume fractions of the constituents could also be expressed as an identity, assuming that few voids were present in the sample.

$$1 = f_a + f_g + f_w \qquad 2.7$$

Fracture surface sections of previously wax infiltrated glass compacts appeared to validate the assumption of void free samples, with typically much less than 1% inclusions (see figures 2.4 a and b). The darker section of the sample indicate the void sections, with the lighter regions indicating the wax covered glass beads.

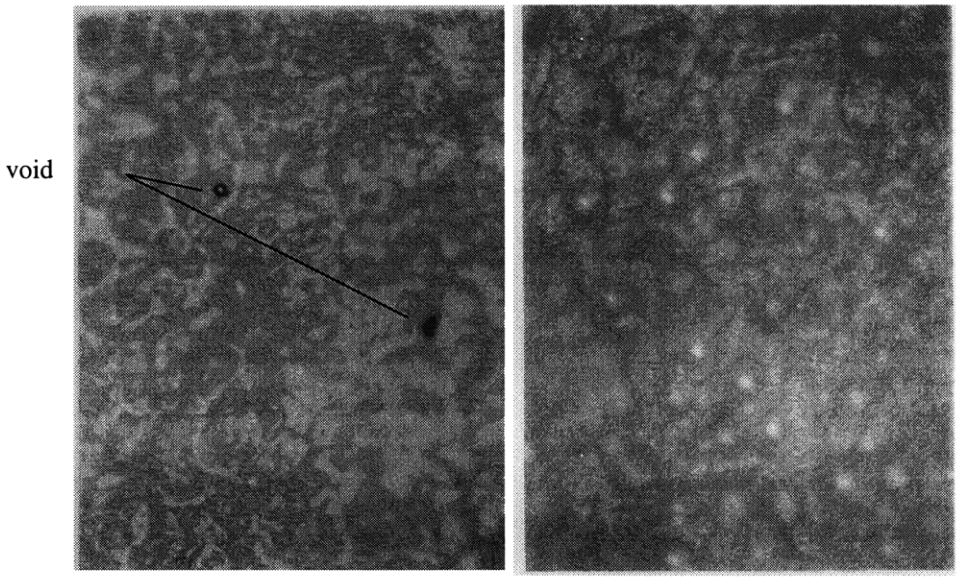

Figure 2.5 Cross sections of wax infiltrated, sintered glass compacts
a) 75x Magnification b) 150x Magnification

As a result, it was only necessary to determine the volume fraction of one of the constituents and use equations 2.6 and 2.7 in concert to determine the volume fraction of the two remaining constituents.

Also, since the volume fraction of the glass in the sample is essentially the packing fraction of glass spheres, it could easily be determined apriori by measuring the volume of a given weight of spheres in a graduated cylinder and calculating the bulk density. The ratio of the bulk density and the actual density corresponds to volume fraction of the glass in the sintered compact.

Using equations 2.6 and 2.7, the following curves were generated, illustrating the appropriate weights in the compact as a function of depth. Figure 2.5 a) represents the combined wax and alumina weight in a slice as a function of depth, while figure 2.5 b) illustrates the alumina weight in a slice as a function of depth. As a check, upper and

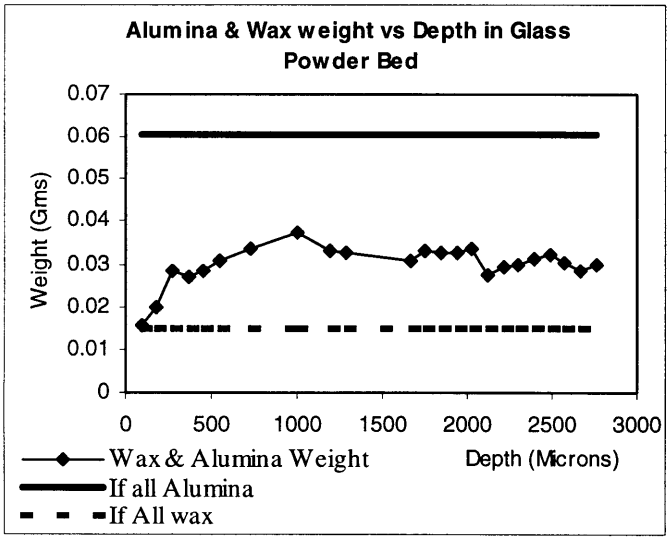

Figure 2.5 a) Alumina and Wax weight as a function of depth in an infiltrated glass compact.

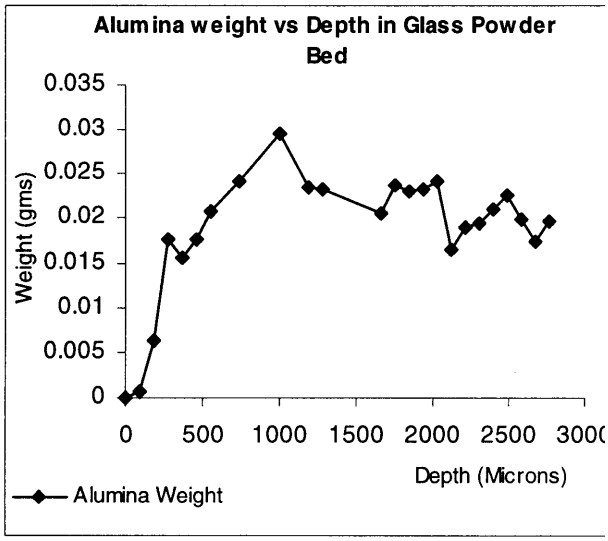

Figure 2.5 b) Alumina Weight as a function of depth in an infiltrated glass compact.

lower bounds for the data were also plotted in figure 2.5a. The upper boundary depicts the case were the void space is completely filled with Alumina (the If all Alumina case), while the lower boundary represents the case were the sample is devoid of alumina and contains only glass and wax (the If all Wax case). Note that each data point in the plots is a slice of thickness 1.2 mils.

2.1.2.2 Constant vs. Ramp Deposition Models

The results of the slicing experiment (Figure 2.5b) were interpreted as a combination of two linear deposition patterns: an initial ramp segment, followed by a constant deposition of material up until the penetration depth of the slurry (see Figure 2.6a).

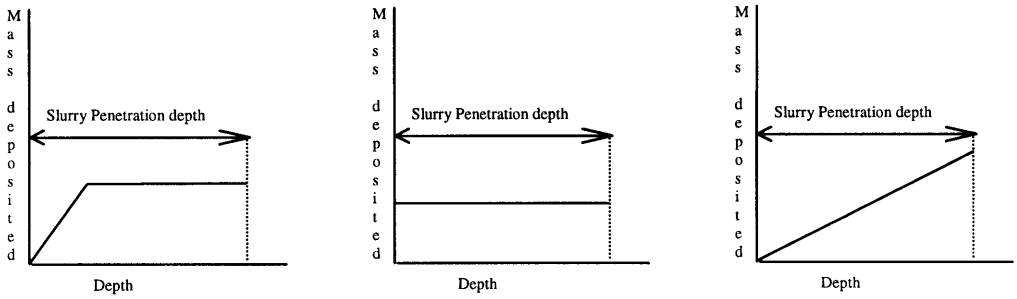

Figure 2.6 a) Ramp-Constant Deposition Model **b)** Constant Deposition Model **c)** Ramp Deposition Model

However, there was a bit of uncertainty about the accuracy of the data during this ramp portion. This uncertainty stemmed from observations during the jetting of the alumina slurry into the glass powder bed. During jetting, there was significant ballistic ejection as the slurry impacted the powder bed surface. This would result in a fewer glass and alumina powders close to the surface and hence a greater wax concentration inferred than in fact was the case. Considering this uncertainty, two models were developed. A constant deposition model (Figure 2.6b) and a ramp deposition model (Figure 2.6c). These two models would in effect "bracket" the actual deposition pattern, giving high and low estimates. For later work however, constant deposition was assumed.

2.1.2.3 Layer by Layer Densification Macro

Armed with these two models of the deposition profile, the next step was to develop an algorithm, and subsequently, a computer based macro that would mimic the actual 3DP printing process, and predict the actual densification.

The mechanics of the algorithm depends on treating the deposition profile as discrete sums instead of as a continuous profile. Using the constant profile as an example, the total amount of material deposited in a given layer varies with the penetration depth as shown in figure 2.7b.

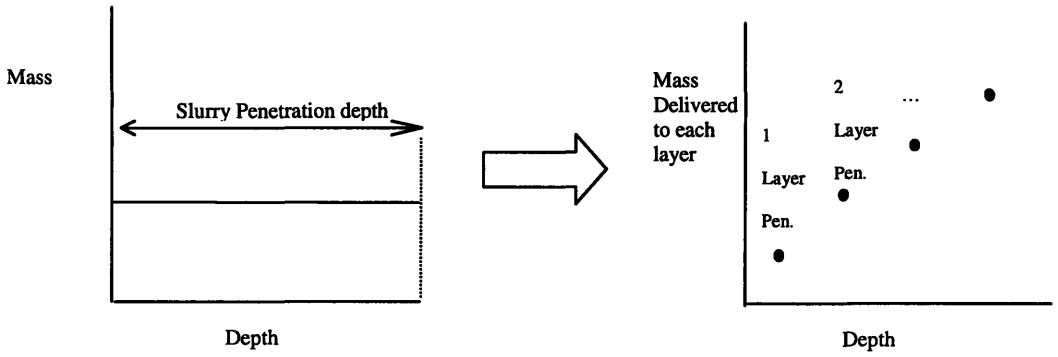

Figure 2.7 Conversion of constant deposition pattern to layer based, point-wise representation.

For example, if the penetration depth is two layers, each layer would be printed into twice, and receive essentially double the material. Refinements to the program include options associated with drying and layer saturation information.

2.1.3 Theoretical Bimodal Packing Fractions via Slurry Printing

With this scheme in place, two different matrices were generated for a base powder with an initial packing fraction of 60%. These matrices predicted the maximum densification achievable by printing a highly loaded slurry into a powder bed. The two matrices also represented the varied approaches to higher density.

The first approach was predicated on moving to a finer layer thickness to allow the slurry to penetrate into multiple layers. The key parameter in this case is (κ), the ratio of the slurry penetration depth to the layer thickness. Values of κ greater than one can be achieved in two ways: by using a sufficiently high flow rate, or spreading thinner layers. The latter was more desirous because using higher flow rates ran the risk of causing bleeding and geometry alteration.

κ = Penetration depth/Layer Thickness	Slurry volume fraction (f) = 0.10	Slurry volume fraction (f) = 0.15	Slurry volume fraction (f) = 0.20
1	0.64	0.66	0.68
2	0.68	0.72	0.76

Table 2.1 Densification Table for Thinner Layers

To generate table 2.1, saturation conditions were assumed for the starting case, were the penetration depth is equivalent to the layer thickness.

The second approach involved multiple applications, with the slurry penetration depth equal to the layer thickness.

# of Applications	Slurry volume fraction (f) = 0.10	Slurry volume fraction (f) = 0.15	Slurry volume fraction (f) = 0.20
1	0.64	0.66	0.68
2	0.68	0.72	0.76
3	0.72	0.78	0.84

Table 2.2 Densification Table for multiple application printing

Tables 2.1 and 2.2 bring to light the duality of both approaches. Simply put, you eventually add the same amount of liquid/material per volume of part. In the first case, the additional material is introduced to the layers below the top layer because of the increased penetration caused by using thinner layers. In the second case, the additional material is introduced to the top layer only, by printing in multiple applications.

An expression for the achievable green density in terms of 3DP process conditions is given below.

$$Green\_Density = PD + N\frac{f \cdot q}{LS \cdot LT \cdot Speed} \leq 86\% \qquad 2.8$$

Were PD, N, f, q, LS, LT and Speed are the initial packing fraction, number of print applications, slurry volume fraction, slurry flow rate, line spacing, layer thickness and fast axis print speed respectively. The upper limit of 86% determined by the maximum achievable densification for bimodal powders (See Section 2.1.1.2)

Consequently, both paths led to a seventy percent dense compact and could even be combined to further increase densification. The lingering question however, was which path would prove better.

2.2 Summary

A discussion of traditional bimodal modeling methods is briefly presented in Chapter 2. In addition, a more accurate model is introduced to simulate the densification mechanism of slurry printing fine powders into 3DP powder beds. As part of this development, a generic deposition profile in slurry printing was experimentally determined and the maximum achievable densification based of process parameters was expressed.

Chapter 3: Development of Titanium Carbide Slurries

3.1 Motivation

The next hurdle in the development of the fabrication of high density bimodal mixtures with the 3DP process, was the creation of stable suspensions of titanium carbide particles that could be printed through the 3DP "boa" jet nozzles. Titanium Carbide particles had previously been identified as ideal candidates because of their low density (4.93 gm/cc), chemical inertness, and also their availability in sub-micron size ranges. The titanium carbide suspensions or slurries would have to be designed to ensure a minimal settling rate, viscosity and average particle size.

A low settling rate was necessary not only for the delivery of a predictable concentration of titanium carbide particles to the powder bed, but also to minimize the very real problems of nozzle clogging and particle agglomeration that often hamper printing of solid particles. The practical consideration of jettability and insufficient line pressure was at the heart of the desire for selecting a dispersant that would result in low viscosity suspensions. As a rule of thumb, slurries with a viscosity greater than 10 centipoise would prove difficult to jet using the 3DP process and would not be considered (Serdy, personal communication).

Two other restrictions or guidelines quickly set for the characteristics of the slurries had to do with the nature of the solvent and the solids loading involved. In an effort to minimize health, handling and drying (after printing) difficulties, a judgment was made to limit the scope of the study to aqueous dispersions. Also, to minimize the number of printing applications necessary to deliver a desired final concentration of titanium carbide into the powder bed, dispersions of at least 10 volume percent would be necessary, with at least 20 volume percent being desirous. This decision was based on the layer densification matrices that had previously been generated (See tables 2.1 and 2.2).

3.1.1 Dispersing Mechanisms at a Glance

As the study began, two basic classes of dispersants or dispersing mechanisms were considered. The first mechanism, electrostatic stabilization, was already employed in existing 3DP binder and slurries (colloidal silica and alumina slurry). It depended on the dispersant increasing the charge of the individual particles causing them to maintain an electrical repulsion for each other and hence remain in suspension. As a rule, electrostatic stabilization of slurries is especially effective with oxides, unfortunately titanium carbide is not an oxide. Thus this means of stabilization was not looked favorably upon. The second mechanism, a characteristic of polymeric dispersants, is successful when the dispersant coats the individual particle and effectively alters the surface characteristics and energy of the particles to increase stability. Both methods are effective only after several hours of ball milling the slurry.

3.1.2 Candidate Dispersants

Based on earlier work (Caradonna, 124-157 and Stefan Koch, 14-31), two polymeric dispersants were selected for trial – Vanderbilt's Darvan C and Rohm and Haas' Duramax 3007. In addition, a literature search unearthed specific work on electrostatically dispersing titanium carbide slurries with polyoxyethylene (POE) in the presence of sodium nitrate electrolytes (Eremenko et al, 23-30).

3.1.2.1 Dispersing Titanium Carbide with Polymer dispersants (Darvan C, Duramax 3007)

The following recipe was used to produce the slurries dispersed with Duramax 3007 and Darvan C for comparison:

1. Start with an appropriate amount of deionized water (usually 100 cc lots).
2. While stirring, add an amount of dispersant equivalent to 1.5% of the dry weight of the powder. Note: A correction must be made for the actual polymer concentration in the

dispersant itself - example: Duramax 3007 is only 45% solids, Darvan C is only 25% solids.

3. Slowly add TiC powders, pausing to allow for proper wetting as the solution is stirred.

4. Stir for 15 minutes.

6. Mill for 24 hrs with Tungsten carbide media that has been vigorously washed in deionized water to remove possible contaminants.

7. After removing mixture, add a couple drops of octanol if any significant foaming is noticed.

Sample Amounts for 100 cc's of 20 vol. % TiC Slurry with Duramax 3007

Mass of TiC – 121.18 gms.

Mass of Duramax 3007 (as received) – 4.04 gms.

3.1.2.2 Dispersing Titanium Carbide with PEO (a.k.a. PEG or PEO) in the Presence of Electrolytes:

The recipe for dispersing titanium carbide with PEO and sodium nitrate ($NaNO_3$) is listed below:

1. Start with 100 cc of Deionized water.

2. While stirring, add 0.05 gms of PEO (500,000 MW).

3. Slowly add 55 gms of TiC (10% by volume solution), pausing to allow for proper wetting of powders as the solution is stirred.

4. Add 0.51 gms of Sodium Nitrate (MW of Sodium Nitrate = 85 gms/mole, add 60mm/litre).

5. Stir for 30 minutes.

6. Mill overnight with Tungsten carbide media that has been vigorously washed in deionized water to remove possible contaminants etc.

3.1.3 Characterization by Settling Velocity

To evaluate the effectiveness of each type of dispersant, a series of settling tests were performed using slurries of varying solid volume fractions. The slurries were allowed to settle under the influence of gravity in graduated cylinders. As soon as a clear interface formed, its progression over time was recorded to obtain a velocity estimate. The velocity estimates were then used to predict the average particle agglomerate size using Stokes' law.

$$V = \frac{d^2(\rho_p - \rho_l)g}{18\mu_l} \qquad 3.1$$

Stokes' law relates the settling velocity of a spherical particle in a fluid to the particle diameter (d), the particle density (ρ_p), the fluid density (ρ_l), and the fluid viscosity (μ_l). As such, the Stokes diameter is indicative of the average size of the agglomerates in the slurry. If the slurry is well dispersed, the Stokes diameter is indeed the average particle size.

Two qualifiers must be discussed regarding equation 3.1. Stokes law is primarily for spherical particles and no correction was made for the coarser shape of the titanium carbide particles (See Appendix for SEM of TiC particles). Also, Stokes law is applicable only to a single particle in a fluid, and not highly loaded suspensions were inter-particle interaction inhibits the settling rate. For such highly loaded slurries, Richardson and Zaki's extension of Stokes' law is more appropriate (Barnes, 231-245).

$$V = \frac{d^2(\rho_p - \rho_l)(1-f)^v g}{18\mu_l} \qquad 3.2$$

The additional parameters in the Richardson and Zaki relationship are the solid volume fraction of the suspension (f) and a constant that varies with particle size (v = 5.25 for sub-micron particles, 4.65 for large particles).

With these settling relationships in mind, the data was tabulated and Rohm and Haas' Duramax 3007 was identified as the best candidate (See Table 3.1).

Dispersant Name	Slurry Volume Fraction	Settling velocity (cm/hr)	Stokes Diameter (μm)	Richardson -Zaki Diameter (μm)
Duramax 3007	15%	0.06	0.28	0.43
	20%	0.06	0.29	0.52
	25%	0.09	0.34	0.73
	30%	0.06	0.29	0.71
Darvan C	15%	0.26	0.52	0.95
	20%	0.56	0.85	1.53
Polyethylene Oxide w/Electrolytes	10%	0.44	0.75	1.93

Table 3.1 Settling behavior of aqueous Titanium Carbide slurries with various dispersants.

3.1.4 Slurry Viscosity and Shear rate dependence

After identifying Duramax 3007 as the dispersant of choice, further work was necessary to characterize the slurries. A key parameter to be determined was the viscous response

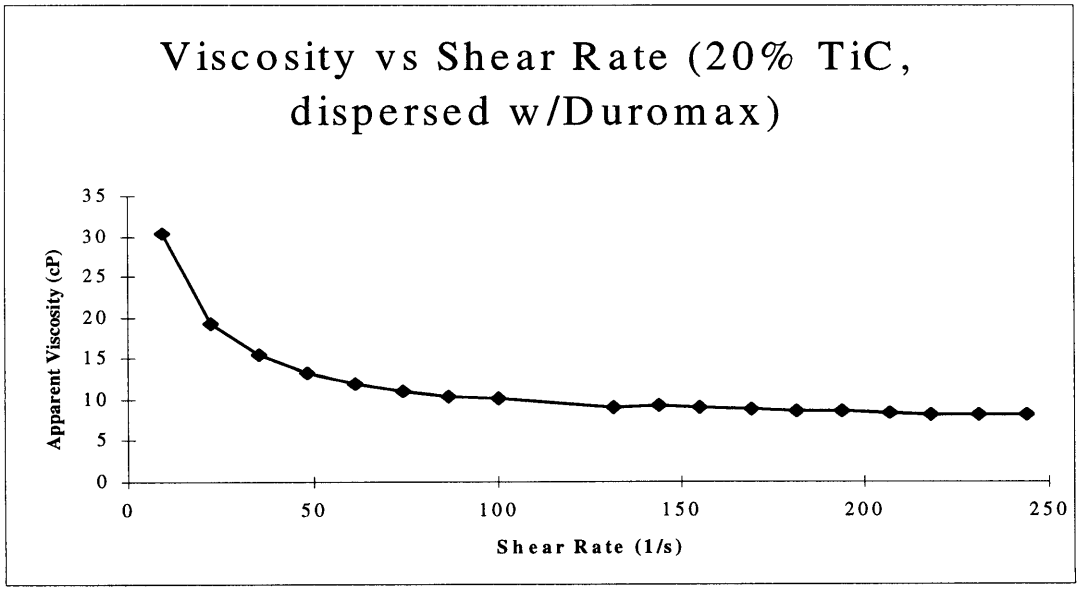

Figure 3.1 Titanium Carbide Slurry Viscosity vs. Shear Rate

of the slurry to shear. Using a Haake RV 100 viscometer, the apparent viscosity of the slurries was determined as a function of shear rate (See Figure 3.1).
The viscosity appeared to level off as the shear rate increased, a positive indication that the dispersion could be stable during jetting through the 3DP boa-jet nozzle. However slurry stability would have to be experimentally confirmed through actual jetting tests because the shear rate at the boa-jet nozzle is on the order of 300,000 per second, well out of the range of the Haake viscometer.

3.1.5 Binder Incorporation into the Slurry Formulation

The path to incorporate a "binder" into the optimized Titanium Carbide slurry began after a fortuitous observation. It was observed that after dropping a few drops of the slurry into 420 stainless steel powder, the green strength was surprisingly high. This strength was magnified after drying. Obviously the dispersant also had some binding properties. A quick test was hastily performed with the concentrated dispersant. Drops of pure Duramax 3007 were allowed to wick into loose 420 powder and the body subsequently dried out. The result was an exceeding strong body that couldn't be broken by hand. Further properties of the dispersant/binder were investigated, notably its response when placed in water. When placed in water, the bound tic/steel body redisperses and looses any binding properties.

To take advantage of Duramax's unique properties, a series of experiments were performed to determine the minimum amount of additional dispersant necessary for binding. Varying mixtures of Duramax and water were pipetted into 420 powder and the results qualitatively compared with the typical 3DP parts bound with Acrysol. Proceeding in this manner, it was determined that approximately 7.6 grams of Duramax per 100 ml of water would be sufficient. This translated to about a two-fold increase in the concentration! The magnitude of the increase was quite troubling at first, but there proved to be little change in the slurry performance during subsequent use besides a slightly higher viscosity. It is important to emphasize however, that it became increasingly important that the slurry be filtered below a 10 micron level before use because of an

increased tendency to agglomerate and buildup on the 10 micron filter after storage for a day while stirring.

Sample Amounts for 100 cc's of 20 vol. % TiC Slurry with Duramax 3007

Mass of TiC – 121.18 gms.

Mass of Duramax 3007 (as received) – 7.6 gms.

Note that a similar procedure with 20,000 MW PEG was attempted, beginning with water and attempting to find the minimum concentration necessary for binding. These trials were unsuccessful because the water-PEG mixture became too viscous for jetting before any binding properties were evident.

3.2 Jetting of Titanium Carbide Slurries

For jetting experiments, the following setup was used (See figure 3.2). A Nalgene bottle containing the TiC slurry was placed in an aluminum pressure vessel. The vessel was subsequently pressurized by a regulated air supply, only 10 –15 psi was necessary, as the fluid lines were relatively short – two feet in total. A cap filter containing a 20 micron nylon mesh filter was placed inline. Note that the 10 micron filter was not extensively used inline because the pressure drop frequently could not maintain the jet, and the slurry would merely drop out of the nozzle.

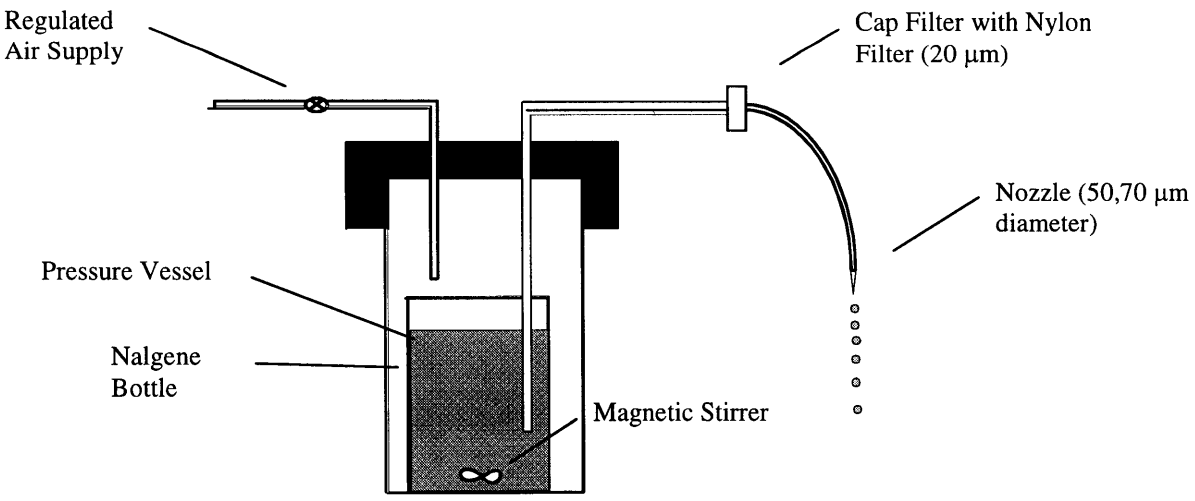

Figure 3.2 Basic Experimental Jetting Setup

Slurries of various volume percentages (10%, 15%, 20%) were prepared and subsequently pre-filtered in stages beginning with a 30 micron nylon mesh filter. Pre-filtering was continued until the slurry was able to pass through a 10 micron nylon filter, though with great difficulty and frequent cleaning of the filter. Rigorous pre-filtering is a key to any successful jetting of slurries. For each volume percentage, the maximum time of jetting was recorded and observations recorded regarding nozzle clogging, slurry concentration changes and miscellaneous issues (See Table 3.2). Note that slurries of 25 volume % and above were not able to be pre-filtered finer than the 20 micron filter level and were not included in this particular study.

Slurry Volume %	Jetting Time (70 μm nozzle)	Notes (70 μm nozzle)	Jetting Time (50 μm nozzle)	Notes (50 μm nozzle)
10%	N/A	N/A	1 hr 5 min	Uninterrupted jetting. Constant slurry concentration.
15%	1 hr 15 min	Clogging at jet startup, subsequent uninterrupted jetting. Constant slurry concentration.	1 hr 10 min	Clogging at jet startup, subsequent uninterrupted jetting. Constant slurry concentration.
20%	1 hr 20 min	Clogging at jet startup, subsequent uninterrupted jetting. Constant slurry concentration.	1 hr 19 min	Clogging at jet startup, subsequent uninterrupted jetting. Constant slurry concentration.

Table 3.2 Summary of Jetting Experiments

The basic knowledge gleaned from the jetting experiments was that jetting the titanium carbide slurries was straight forward, with the major hurdle being random clogging during startup. Once the jet was started and became stable, it would run without interruption.

Feeling fairly satisfied with the results of the jetting experiments and confident that the titanium carbide slurries were "jet-able", the next order of business was to determine if the slurries could in fact be stored and reused. Storage in this case meant, leaving the slurry overnight while stirring. The fear was that the particles would re-agglomerate to such an extent that the slurry could not be reused or after a day or so, the chemical stability of the slurry would degrade.

To determine if this type of phenomena was occurring, a series of jetting experiments were conducted over four days. The goal of the experiment would be to detect any agglomeration of the slurry over this period, and to determine if the slurry could be jetted and re-used after a period of time. To begin, a 20 volume percent slurry was made and pre-filtered in stages (40, 30, 20, and 10 micron nylon filters). The slurry was then jetted through a 50 micron nozzle using the test stand. After day 1 jetting, the slurry was continuously agitated using a magnetic stir bar during storage. On day 2, the slurry was passed through a 10 micron filter to detect any build up of agglomerates (in the filter) and subsequently jetted. This procedure was repeated on Day 3 and 4. A summary of results and observations is listed below in Table 3.3.

	Filtering Observations	Jetting Observations
Day 1	No buildup detected in 10 micron filter, slurry passes with no additional difficulty	Clogging at jet startup, subsequent uninterrupted jetting.
Day 2	No buildup detected in 10 micron filter, slurry passes with no additional difficulty	Clogging at jet startup, subsequent uninterrupted jetting.
Day 3	No buildup detected in 10 micron filter, slurry passes with no additional difficulty	Severe Clogging at startup, unable to maintain jet after several attempts.
Day 4	No buildup detected in 10 micron filter, slurry passes with no additional difficulty	Clogging at jet startup, subsequent uninterrupted jetting.

Table 3.3 Summary of Slurry re-useability experiments

Similar to the previous experiment, it was observed that the critical phase in jetting is the startup, and once this phase is passed, little difficulty is faced. This is validated by the Day 3 and 4 results. If the stability of the slurry was the cause of the inability to jet on

Day 3, this trend would have continued and in fact been amplified in Day 4. As it stands, careful attention must be paid to equipment handling and setup for any jetting to be successful.

3.2.1 Drop on Demand Printing of Titanium Carbide slurries

Convinced that the slurry was quite stable and chemically sound over a time period (at least four days), another form of printing was briefly explored, notably Drop on Demand (DOD) printing. DOD printing employs a self contained cartridge that releases a single droplet based on an electrical impulse. This brand of printing is employed in Hewlett Packard inkjet printers and had previously been adapted to the 3DP process (Peter J. Baker). The advantage of DOD over the traditional Continuous Jet Process is that finer drops can be generated producing a smaller minimum feature size. However, since the build rates of DOD as currently used in 3DP are quite low, exploring this line of research was intended merely to demonstrate the process capability. Working in concert with another researcher (Vedran Knezevic), a 10 volume % titanium carbide slurry was produced and subsequently printed on a glass substrate (See figure 3.3).

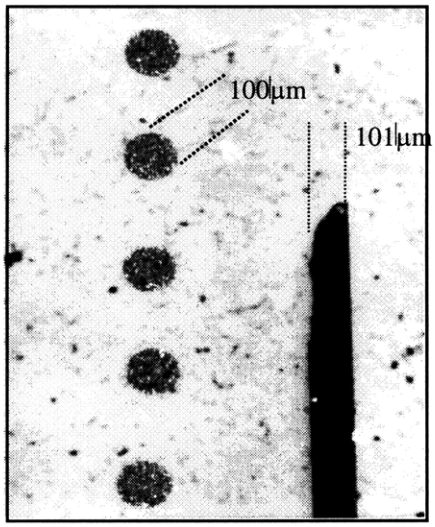

DOD Printing Parameters

Droplet generation rate:	166 hz
Droplet Spacing:	300 μm
Mean Diameter of TiC primitive:	100 μm

Figure 3.3 DOD printed Titanium Carbide on Glass substrate, Diameter of marker is 0.004 inches or 101μm

In addition to printing droplets onto the glass substrate, TiC lines were printed into a powder bed of large TiC particles and Sintered at 1100 °C for 30 minutes as per a technique discussed later in this thesis (Section 5.2.3.1). The resulting strength of the lines was poor due to the low concentration of sintered fine TiC particles holding the line together. Further work was discontinued in lieu of other paths.

3.2.2 Slurry Stability, Break-off and Charging/Deflection issues

The next step in investigating the viability of the slurry printing path was to study the droplet formation process employed during printing. In the 3DP process, the binder

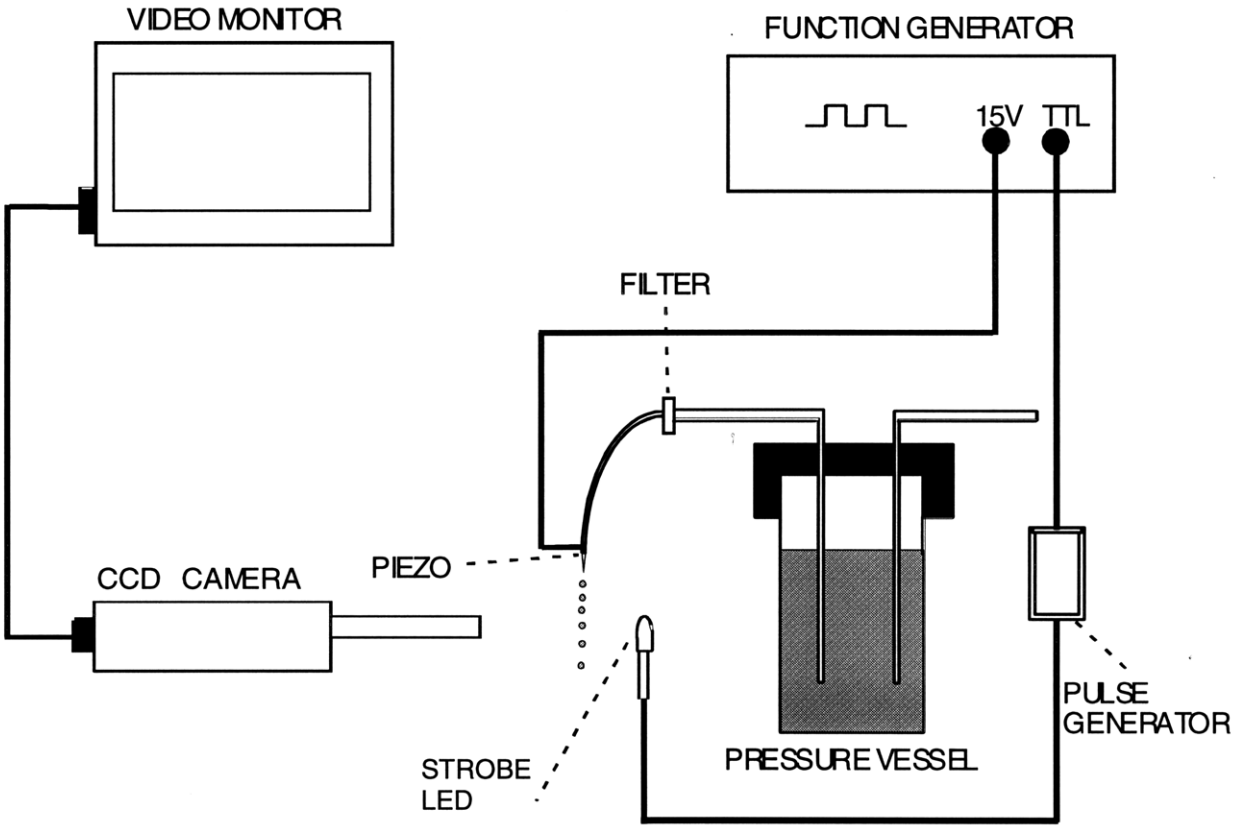

Figure 3.4 Droplet Visualization Setup

stream is excited by a piezoelectric element vibrating at a characteristic frequency. The "Rayleigh" frequency, in addition to the flow rate, determines the distance (referred to as break-off) the stream travels before it breaks up into tiny droplets. The droplets are subsequently charged via a charging cell and then deflected as desired to control their

landing position in the powder bed. The key to any successful printing is the ability to maintain a stable flow rate and suspension of slurry particles during the droplet formation stage. To study the break-off phenomena of the slurry, a droplet visualization test platform was devised (See figure 3.4).

The setup works as follows. The continuous stream is broken up into separate drops by the piezo-electric element at a frequency determined by the function generator. At the same time, a signal varying at the same frequency is fed into a pulse generator, causing the LED to flash at a similar rate. If the slurry is stable during this process, the drops are effectively strobed or "frozen" in flight. The individual droplets can then be viewed and accessed qualitatively utilizing a monitor and a CCD camera with an appropriate lens attachment.

The qualitative assessment of break-off is straightforward: *the droplets must remain frozen throughout printing at a given frequency.* No disruptions in the flow, random merging of droplets, or sudden continuous streams can be tolerated.
That said, both slurry formulations (with and without binder) were studied with these factors in mind. All experiments were performed using a 70 micron nozzle, and repeated later with a 50 micron nozzle. The results are summarized in table 3.4.

	TiC Slurry 20 volume fraction with binder	TiC Slurry 20 volume fraction without binder
Filtered through 20 micron nylon filter	1. Occasional Disruptions in flow. 2. Random merging of droplets. 3. Occasional variation in break-off.	1. Occasional Disruptions in flow. 2. Random merging of droplets. 3. Occasional variation in break-off.
Filtered through 10 micron nylon filter	1. No disruptions in flow 2. Droplets frozen during entire jetting period (25 minutes). 3. Stable break-off of droplets.	1. No disruptions in flow 2. Droplets frozen during entire jetting period (26 minutes). 3. Stable break-off of droplets.

Table 3.4 Summary of Break-off and droplet generation experiments

It was evident from the results of the droplet generation study that an important factor in jetting sub-micron slurries, is the removal of 10-20 micron sized agglomerates from the slurry. Even a tiny amount of agglomerates of this size hamper stable droplet generation. It should be noted that agglomerates of this size do not seem to hamper jetting, as there was no significant clogging, but they do affect stable droplet generation, and therefore printing. Filtering below a 10 micron level was regarded after this as a go-no-go condition for printing TiC slurries. For this reason the practice of not stirring the tank (see Figure 3.4) was started, a departure from the setup employed in previous work (Figure 3.2). With this scheme in place, agglomerates in the 10-20 micron range would settle out and not disturb steady droplet formation. This remains a temporary fix however, and limits the jetting to only a couple of hours before the slurry begins to noticeably settle. Using a 10 micron filter in-line was the most obvious solution, but the pressure requirements for a steady jet proved too high in practice. For long runs to be possible, this hurdle must be overcome.

3.3 Summary

The development of stable aqueous dispersions of titanium carbide is chronicled in chapter 3, with the spotlight on slurry properties and jetting considerations. Two slurry formulations were developed, a binder-less TiC slurry with a low concentration of Duramax 3007, and a slurry with a higher concentration of Duramax to serve as the binder.

Chapter 4: Slurry Printing Deposition Patterns - Infiltration effects and ensuring a uniform microstructure.

4.1 Analysis of Bimodal Fracture Surfaces.

A basic question that had been left unanswered to date, but was necessary in order to characterize the densification mechanism at play was *where do the fine powders end up?* This was important for two reasons. The first reason had to do with the fear that the fine powders would preferentially gather at the necks between the large powders, be non-uniformly distributed throughout the matrix, and hinder subsequent infiltration. An excess of fine channels would raise the infiltration time and increase the possibility of trapping gas within the body. Such trapped gas would manifest itself as voids within the compact. The second fear was that the deposition pattern would vary within the layer, and in the worst case, result in more material close to the surface, effectively introducing periodicity as subsequent layers were spread.

4.1.1 Sintered Bimodal Samples Without Binder

To see if this was indeed an issue, fracture surfaces of lightly sintered 316L-TiC bimodal compacts were observed (See figure 4.1). These samples were created by pipetting in the

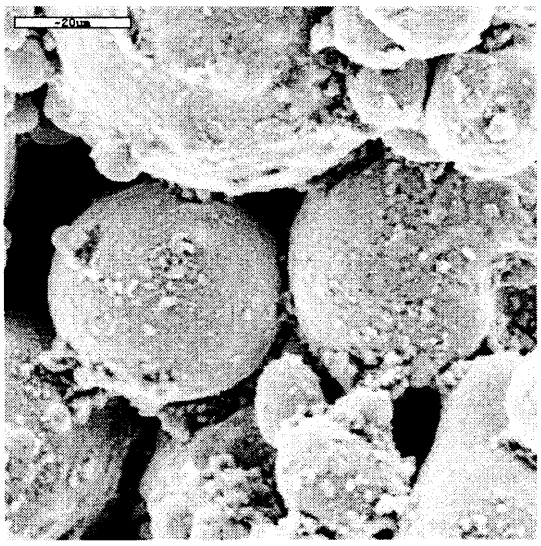

Figure 4.1 Sintered Bimodal 316L-TiC primitives, 20 micron scale bar.

fine TiC slurry (without binder), in an effort to mimic a printing application. The tiny pucks, were subsequently removed and sintered at 1250°C for 30 minutes. Observations of the TiC-316L fractures led to two inescapable conclusions about the deposition pattern. (1) The fine TiC particles tend to gather or collect at the necks or interfaces between large powders and, (2) adhere themselves to the surfaces of the large powders. This often leads to empty regions that could be filled in successive applications if the multiple printing option was employed in concert with drying.

4.1.2 Green Bimodal Samples With Binder

The next step was to consider the case when a binder was present in the slurry - *would this affect the general deposition trends?*

Before repeating the experiments however, a further refinement made to the procedure in order to more accurately mimic printing. In lieu of pipetting the slurry into the powder bed, 15 Volume % TiC slurry (with additional Duramax as binder) was jetted into a 316L powder bed that was mounted on a rotating disk, using a 70 micron nozzle. This produced a large ring that could be removed, fractured and studied. The fact that the rings could be removed was also encouraging. It confirmed the efficacy of the modified slurry formulation containing binder. A schematic of the setup is illustrated below in

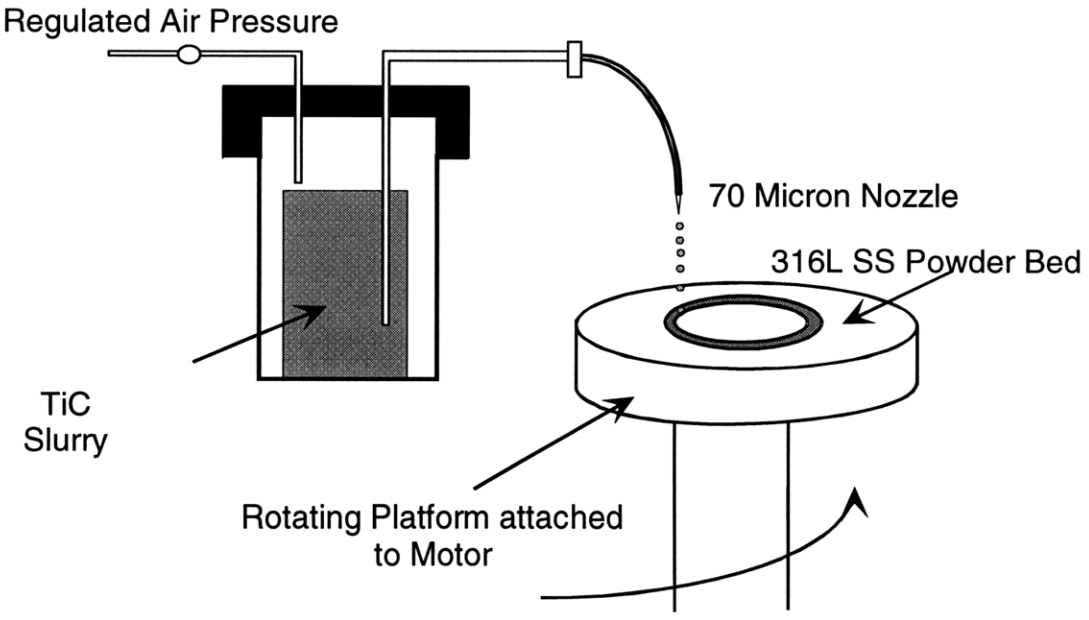

Figure 4.2 Schematic of rotating disk apparatus

figure 4.2.

The resulting images appeared to correlate the findings of the sintered samples, with a similar deposition pattern observed, i.e. gathering at necks and some empty regions (See figure 4.3).

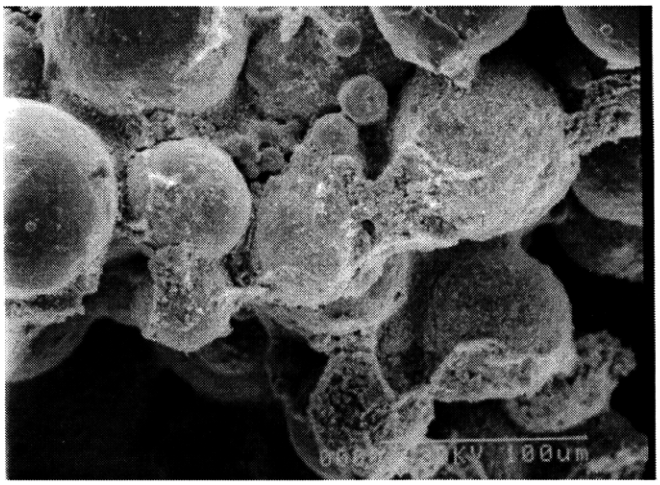

Figure 4.3 Fracture of 316L-TiC Ring Sample, 100 micron scale bar.

The down side of the deposition pattern, was of course the tendency of the fine powders to gather at the necks of the large powders. This forced us to consider the possibility that subsequent infiltration of bimodal compacts could be hindered.

4.2 Infiltration Study of Bimodal powders

The primary source of concern when it came to infiltrating bimodals, was the possibility of trapping gas due to differing rates of infiltration in a porous body. A common expression of the infiltration rate or velocity is the Washburn equation (Washburn, 273-283). Washburn related the liquid velocity, V, to the pore radius (r), liquid surface tension (γ), viscosity (μ), and infiltration depth (h):

$$V \propto \frac{r\gamma \cos\theta}{\mu h} \qquad 4.1$$

This expression brings to light the problem, the liquid infiltrant could, in effect, encircle the gas as it was pushed out of a small sized pore because of the faster infiltration rate in an adjacent large pore.

4.2.1 Forming gas vs. Vacuum Infiltration experiments

To get a sense of whether such phenomena would occur, a qualitative experiment was designed. Sintered bimodal TiC (74-105 microns, and sub-micron mixtures) samples would be infiltrated in forming gas and compared to samples infiltrated under vacuum. It was felt that if gas was indeed being trapped, it would appear as excessive porosity in the forming gas samples. The decision to use a pure bimodal, i.e. no steel present, eliminated complications associated with dissimilar materials. Appropriate concentrations of the big to fine powders, 73.5:26.5, were selected in order to yield the maximum packing density (See section 2.1.1.2 for explanation). The TiC samples were infiltrated with a copper-nickel-manganese alloy for 30 minutes at 1120°C.

In addition, bimodal Tungsten carbide (70 micron avg., and sub-micron mixtures) of similar concentration, infiltrated with pure copper were observed. This was done to correlate the results with a less complex material system (i.e. pure infiltrant, pure bimodal). Concurrent materials system development work done with TiC had ruled out infiltration with pure copper (See Section 5.2.3.1). The bimodal WC samples were infiltrated for 30 minutes at 1200°C.

The results of the experiments are as follows. In the samples infiltrated in forming gas, porosity was evident at interface regions in both the TiC and WC samples. By interface regions, I am referring to regions where the average pore size changes dramatically, i.e. between sub-micron and large powders, and at infiltrant-powder interfaces (see figures 4.4 a, b).

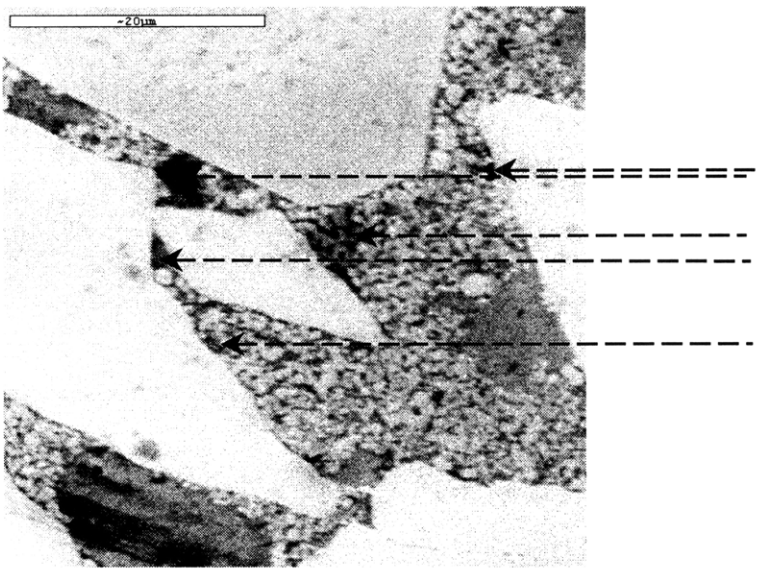

Figure 4.4a) WC-Cu Infiltrated Sample, 20 micron scale bar Arrow lines are drawn to indicate the location of porosity.

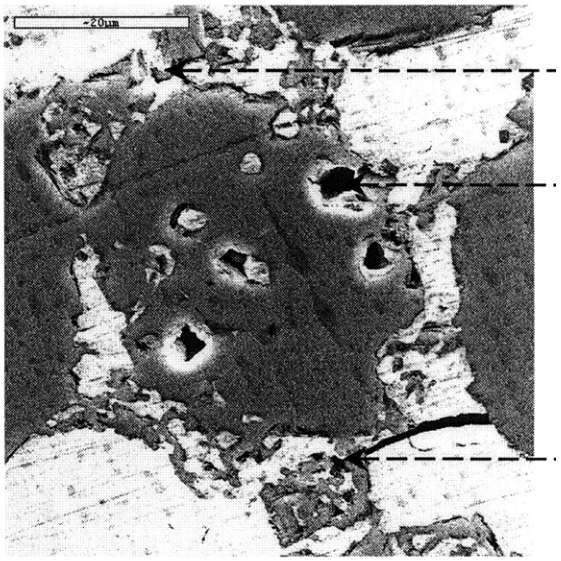

b) TiC infiltrated with Cu-Ni-Mn, 20 micron scale bar.

The vacuum infiltrated samples failed to demonstrate similar consistent patterns in porosity at the interface regions. Figures 4.5 a,b are high magnification images taken of the interface regions between the infiltrant and the large and small powder region. The WC sample did however exhibit some occasional porosity at the interface region, though not as systematic as the forming gas samples.

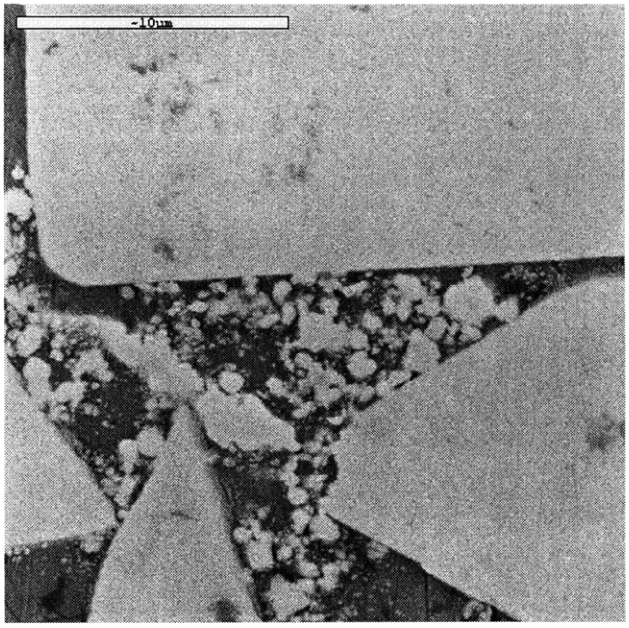

Figure 4.5a) Vacuum Infiltrated WC-Cu Sample at max Bimodal concentration. (10 micron scale)

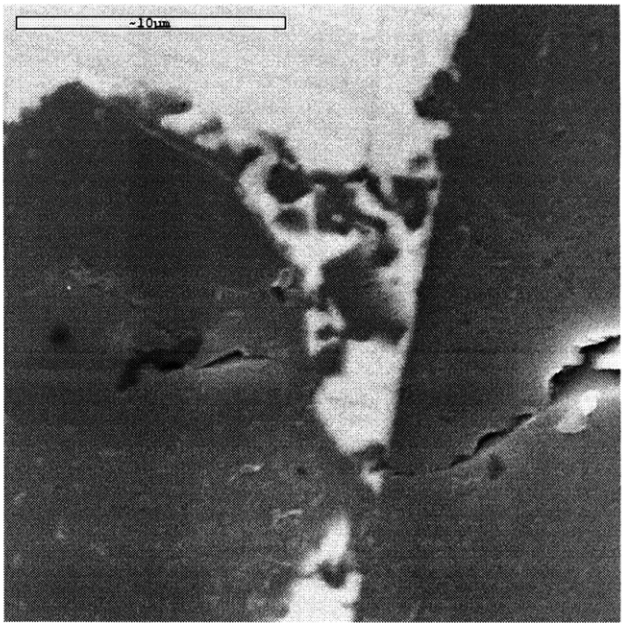

b) Vacuum TiC Infiltrated with Cu-Ni-Mn at max Bimodal concentration (10 micron scale).

There was however some evidence of holes within the large TiC particles themselves (figure 4.5b). Since these holes were within the particles, infiltration of this region would be impossible (with or without vacuum). The feeling was that the craters were either introduced during diamond polishing of the samples or during manufacturing. Inquiries with the manufacturer failed to shed light on the source of the intra-particle holes.

4.2.2 Effect of Bimodal Concentration and Size Ratio on Porosity.

The next issue to be flushed out was whether the presence of voids had anything to do with the relative concentration of fine powders in the matrix or the relative sizes of the powders. As a result, vacuum infiltration experiments were performed with two relative sizes of TiC powders in the bimodal mixture. As cast mixtures (Wet mixing with water) of sub-micron and 74-105 micron TiC powders was compared with similar mixtures of sub-micron and 10 micron powders. This comparison was conducted at two levels of fine-to-big concentrations, the maximum packing concentration (26.5:73.5), and approximately one-half of the maximum concentration (13.25: 86.75). The decision to infiltrate the samples under vacuum was to eliminate the trapped gas issue as the cause of any resulting porosity.

The experiments were conducted under vacuum conditions and repeated with the tungsten carbide-copper system. The sizes of the Tungsten Carbide particles were comparable; sub-micron, 10 micron and 70 micron averages. All samples were sectioned, diamond polished to a 1 micron finish, and subsequently observed with a scanning electron microscope. A summary of the observations from the experiments is provided below along with the representative images.

4.2.2.1 Bimodal TiC Samples infiltrated under Vacuum.

No discernable pattern was observed with regards to the pattern of porosity in the vacuum infiltrated TiC Samples (See figures 4.6a-d). Little porosity was observed in these

samples, other than the previously seen intra-particle porosity. This was encouraging as it indicated the processing route of Bimodal TiC parts, i.e. infiltration under vacuum. Inexplicably, there was little fine TiC evident in the samples with the smaller size ratio.

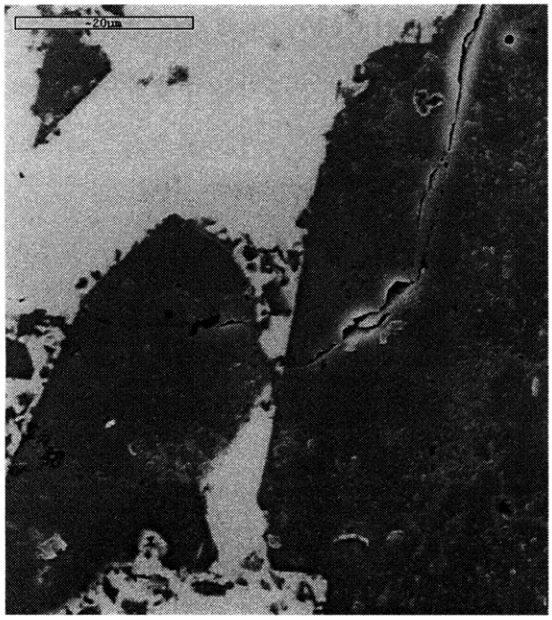

Figure 4.6a) 74-105 micron & Sub-micron TiC; 73.5:26.5, Large to small powder concentration ratio (20 micron scale bar).

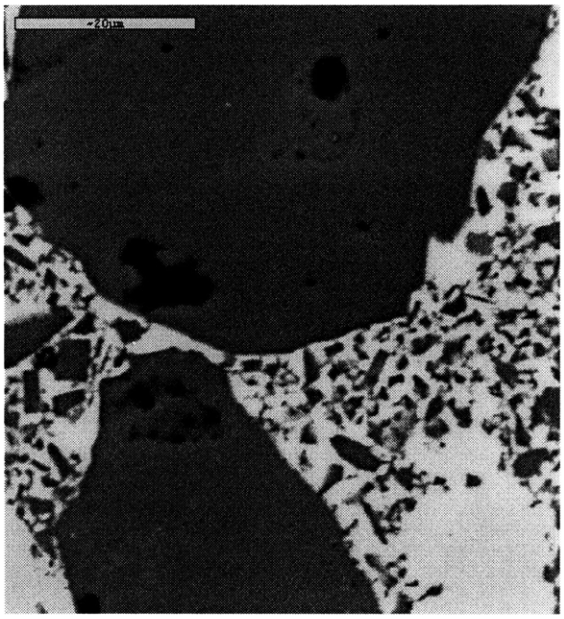

Figure 4.6b) 74-105 micron & Sub-micron TiC; 86.5:13.5, Large to small powder concentration ratio (20 micron scale bar).

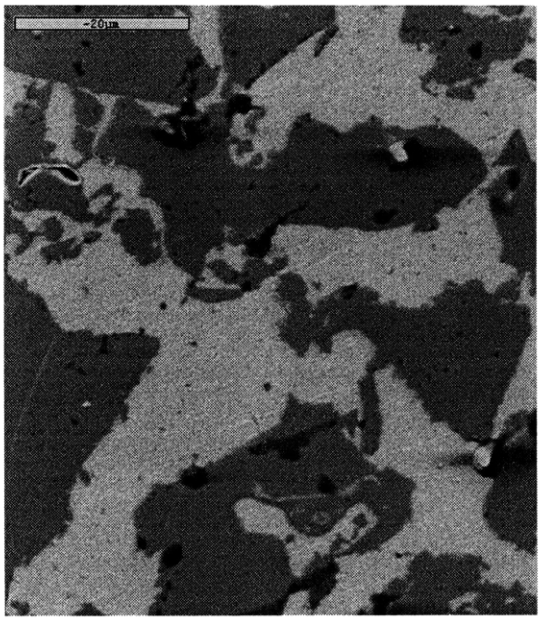

Figure 4.6c) 10 micron & Sub-micron TiC; 73.5:26.5, Large to small powder concentration ratio (20 micron scale bar).

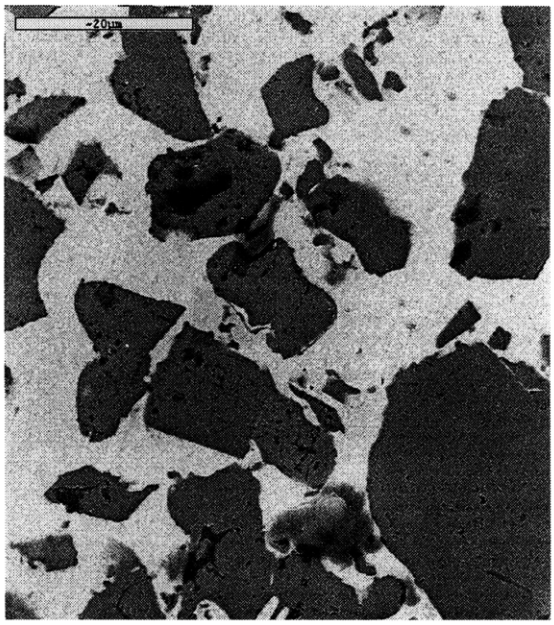

Figure 4.6d) 10 micron & Sub-micron TiC; 86.5:13.5, Large to small powder concentration ratio (20 micron scale bar).

4.2.2.2 Bimodal WC Samples Infiltrated under Vacuum.

The results obtained from the infiltrated bimodal WC samples are as follows. Slight porosity was evident in all samples with the large size ratio (70 micron avg.: sub-micron). This porosity appeared to be primarily consigned to the interfaces between the fine and large WC powder regions (See figures 4.7 a, b). Little or no interface porosity was

Figure 4.7a) 70 micron avg. & Sub-micron WC; 73.5:26.5, Large to small powder concentration ratio (50 microns scale bar).

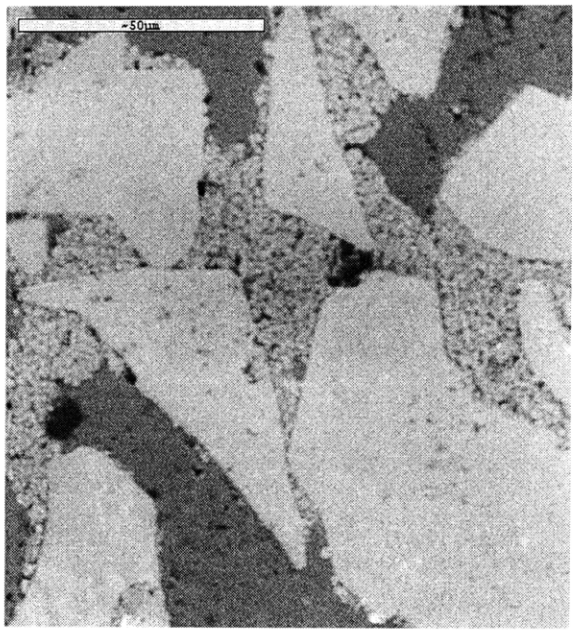

Figure 4.7b) 70 micron avg. & Sub-micron WC; 86.5:13.5, Large to small powder concentration ratio (50 micron scale bar).

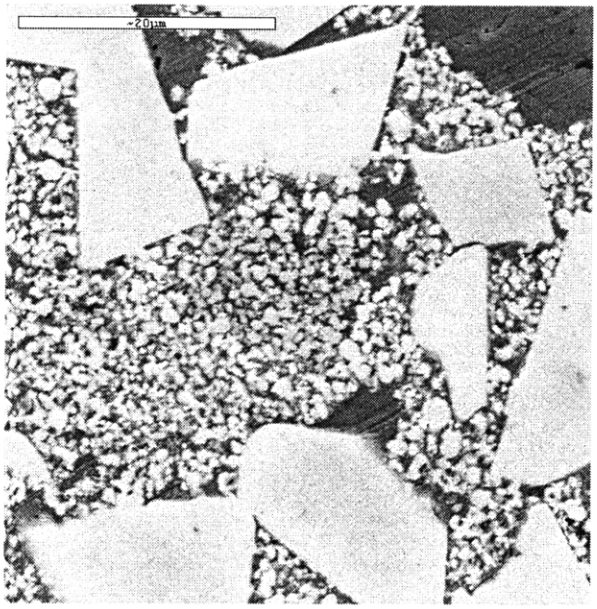

Figure 4.7c) 10 micron avg. & Sub-micron WC; 73.5:26.5, Large to small powder concentration ratio (20 micron scale bar).

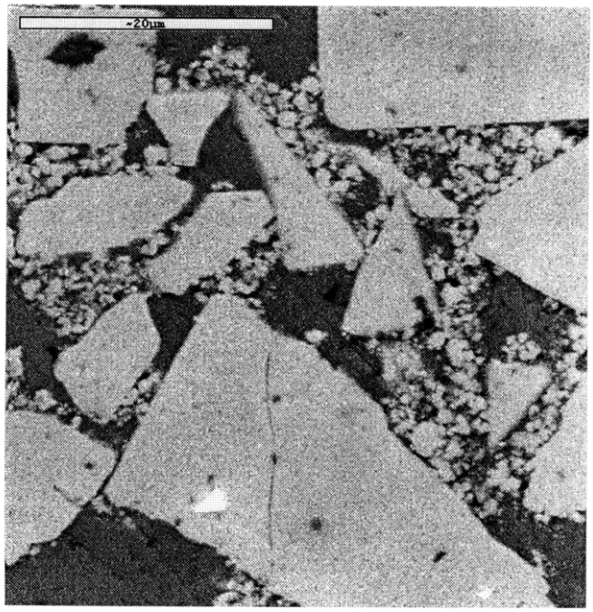

Figure 4.7d) 10 micron avg. & Sub-micron WC; 86.5:13.5, Large to small powder concentration ratio (20 microns scale bar).

observed in the samples with the smaller size ratio (See figures 4.7c,d). These results were in keeping with the general assumption that as the powder sizes became more dissimilar, achieving complete infiltration became more difficult. It however did not agree with the premise that this was caused by the trapping of gas due to contrasting infiltration rates, as there was no gas to be trapped. Some other mechanism was at play that was not fully understood.

The difference in bimodal concentration did not appear to have a substantial effect on porosity. In the case of WC, the more dominant variable is the difference in size ratio.

4.3 Assessment of Printed Bimodal Parts and Densification Mechanism.

The next step in the development of bimodal parts was determining the optimal printing parameters for increasing the green density via slurry printing. The key issue was which parameters, i.e. line spacing and layer thickness, would yield the most dense and homogeneous microstructure. To do this, several test coupons would have to be generated and the microstructure examined under magnification.

4.3.1 Design of Mini Rotary 3DP Machine

In order to provide an easy means of generating bimodal coupons for study in a relatively short amount of time, a scaled down 3DP machine was necessary. The machine, nicknamed "Quickee", (See figure 4.8) was designed to have the functionality of the alpha machine, except for charging and deflection to control the geometry. The Quickee machine would be able to print coupons of at least 8-10 layers. To do this, a simple scheme of rotating the powder bed at a desired speed (fast axis) and slowly indexing the nozzle (slow axis) in order to print adjacent lines was concocted.

A summary of the six key functional requirements of the mini rotary machine is listed below:

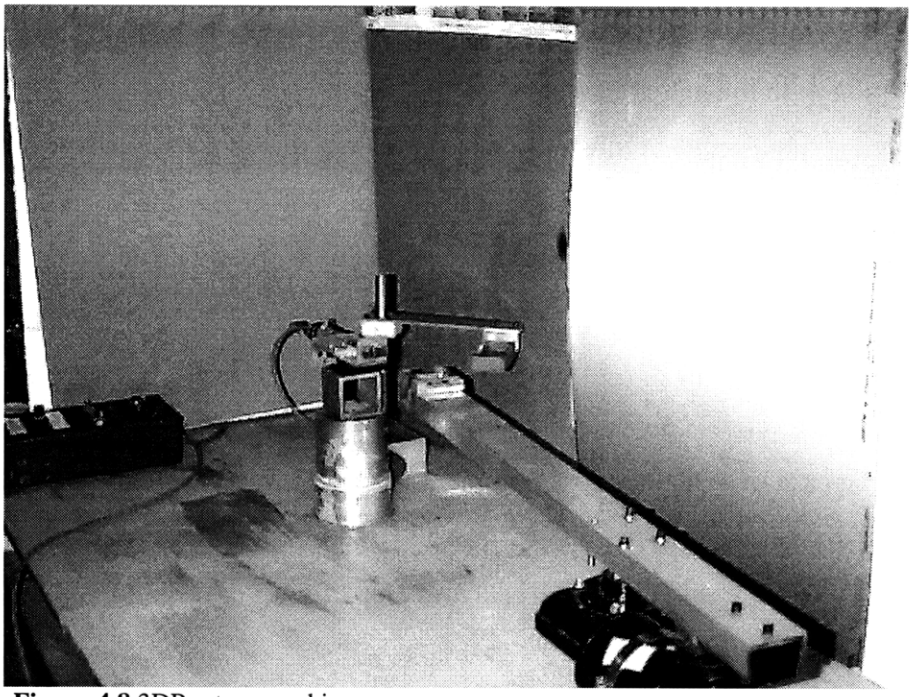

Figure 4.8 3DP rotary machine

FR1: Ability to jet suspension of particles and make droplets.

FR2: Move the powder bed at a speed of 1.5 m/s

FR3: Print droplets over a range of line spacings (130- 230 microns)

FR4: Ability to build a part of at least 10 layers (layer thickness' of 100-230 microns)

FR5: Define at least one edge of the coupon.

FR6: Ability to inspect the droplets.

To satisfy the functional requirements, six corresponding design parameters (DP's) were selected:

DP1: A pressurized fluid system and nozzle with piezo element.

DP2: A rotating platform attached to a variable speed motor.

DP3: A motorized micrometer platform with a stage for the nozzle holder.

DP4: A powder bed with slots for removable gauge pins to modify the bed height manually.

DP5: A removable manual catcher, and associated electronics to synchronize the start of the nozzle motor with the angular position of the rotating platform.

DP6: A strobe LED attached to a hand held microscope.

Specific issues related to the critical DP's are investigated below:

The fluid system and droplet generation

The design of the fluid system had been previously completed. The setup to visualize

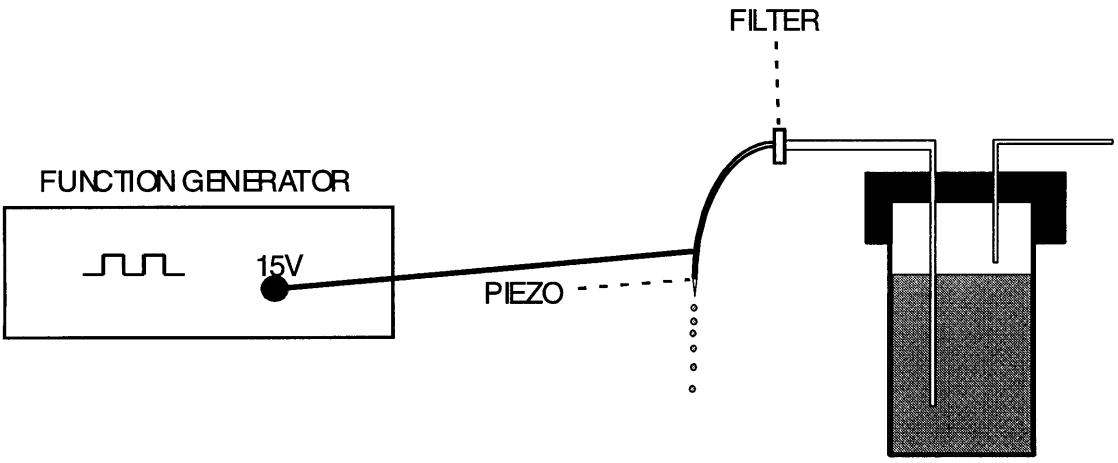

Figure 4.9: Fluid system and droplet generation scheme for rotary machine

droplets (see section 2.2.9) was recreated without the CCD camera attachment for this purpose.

Rotary platform and motor:

The key issues when it came to designing the rotary platform were (1) rotational speed of the motor and (2) the length or radius of the platform. Two constraints aided in the selection. To maintain similarity to the alpha machine, the linear speed would have to be 1.5 m/s. And to prevent the powder bed from shifting, centripetal accelerations would have to be less than 0.5g (Akobuije Chijioke, personal communication). The governing physical relationships are listed below:

$$V = \omega R = 1.5 m/s$$
$$a = \omega^2 R \leq 0.5g \qquad \text{4.2 a, b}$$

With these relations, it was straightforward business to specify that the powder bed be mounted at a radius of 0.45m with the motor rotating at 31 rpm.

Motorized platform with nozzle holder

To control the line spacing, a 12 Volt DC motor with a gear reduction ratio of 187.7:1 and an output shaft rpm of 24 was coupled to a 500 micron/turn micrometer stage. This would allow us to set the starting position at each layer and move the nozzle at a given traverse rate. The traverse rate, was easily related to the line spacing and the rotational speed of the powder bed motor:

$$V = linespacing \cdot \frac{\omega}{2\pi} \qquad 4.3$$

The desired rotational speed of the Nozzle DC motor was determined in a similar manner, in terms of the rotational speed of the powder bed (ω):

$$Nozzle\_motor\_rpm = 60 \cdot linespacing \cdot \frac{\omega}{2\pi} \frac{turns}{travel} \qquad 4.4$$

With this structure in place, voltage applied to the DC motor (which determined the rpm) could easily be calibrated to the line spacing.

Applied Voltage (DC)	Line spacing =37.4*Voltage – 35.6 (Microns)
4.5	132
5	155
5.6	172
6	192

Table 4.1 Nozzle Motor Calibration chart

Removable Catcher and synchronizing electronics

To effectively define one edge in a repeatable manner, it was necessary to perform two distinct actions: (1) begin printing each layer at the same position indicated by the micrometer stage and (2) engage the traverse of the nozzle at the same angular position of the rotor platform at the beginning of each layer. To accomplish the latter task, an electronic scheme utilized by a previous graduate student (Peter J. Baker, 63) was adapted as illustrated in figure 4.10.

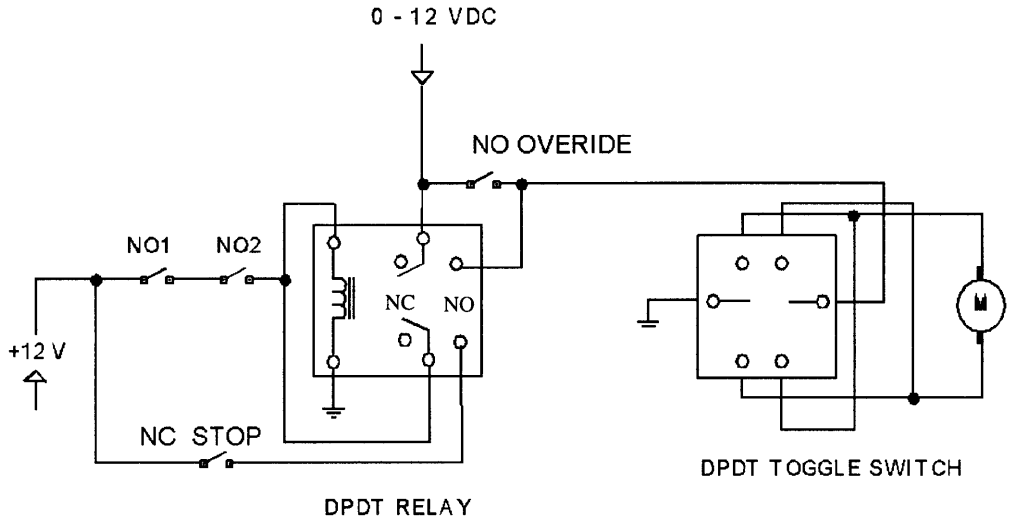

NOTE: NO1 is the normally open switch on the rotary machine.
NO2 is the normally open manual pushbotton (Start/synch).
NC OVERIDE is a manual overide switch to position the nozzle motor.
NC STOP is normally closed stop switch.
The DPDT Toggle switch is used to change direction of motor (forward/reverse).

Figure 4.10 Rotary 3DP machine Circuit Diagram

This scheme involved mounting a normally open switch, (NO1) that was automatically engaged at a given angular position, as the powder bed rotated. The switch was placed in series with a manual normally open switch (NO2) that the user throws. When both switches are simultaneously engaged, 12 volts is latched across the DPDT relay and the motor engages. The motor remains in motion until the user manually stops the traverse by opening the normally closed halt switch (NC STOP). The DPDT toggle switch, is used to set direction of the motor carrying the nozzle. An "over-ride" switch was also included to set the start position of the nozzle.

To complete the synchronization, a manual catcher was added. This catcher was swung out of the way during the rotation prior to the engaging of the switch, allowing the droplets to strike the powder bed.

Strobe LED and handheld microscope

To provide a mechanism for quickly checking that droplets were in fact being generated at the start of each layer, a strobe LED was attached to a handheld microscope (60x magnification). The LED was subsequently strobed at the same frequency as the piezo element in the nozzle, and could be conveniently removed from the path of the rotor during printing.

4.3.2 Printing of Molybdenum-TiC Coupons

Once the Quickee machine was operational, the decision was made to generate Molybdenum-TiC coupons as the representative case study. This was done for a couple of reasons. First, the Molybdenum powder was available in a uniform spherical size (approximately 52 micron avg.), and second, the project was moving away from the flagship 420 Stainless Steel – Bronze infiltrant material system in lieu of newer Molybdenum based systems. This was due to the age hardening properties exhibited by the copper-nickel-manganese infiltrant used to infiltrate Molybdenum parts. Similar hardening properties were seen in the infiltrated Molybdenum-TiC samples (Section 5.4.4).

4.3.2.1 Experimental Strategy

As discussed in Section 2.1.3, two approaches to densification were to be examined using 50 micron nozzles: (1) multiple application printing and (2) using thinner layers to increase the effective slurry penetration depth. To simultaneously explore both alternatives and determine the printing parameters that would yield the maximum

densification with the least layer defects and inhomogeneity, a systematic strategy was developed to minimize the number of necessary experiments (See figure 4.11).

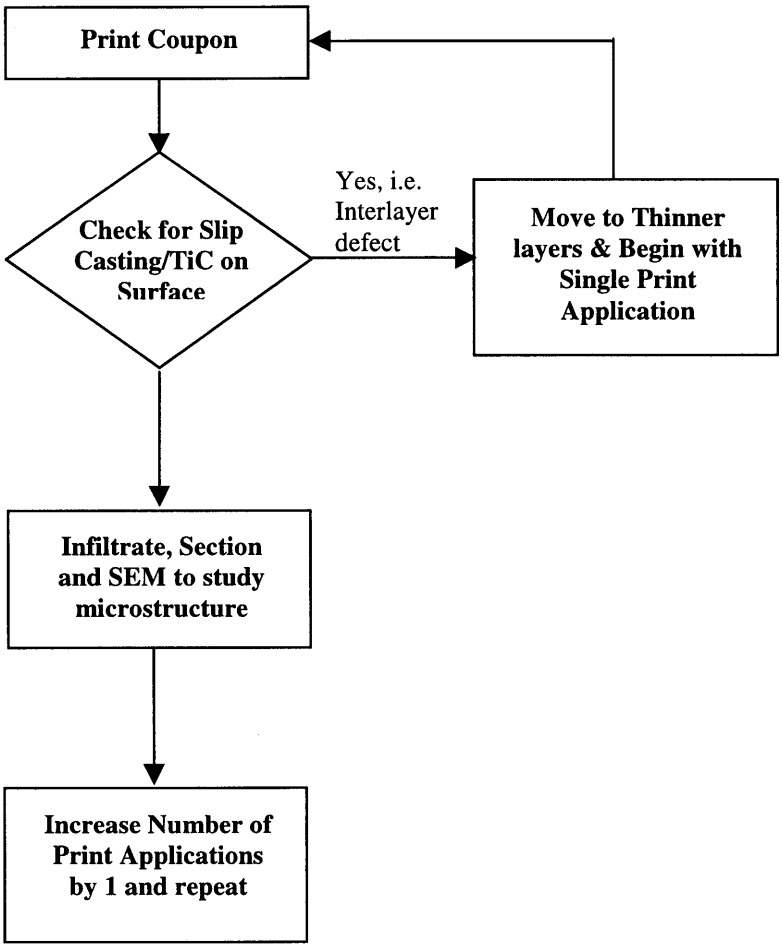

Figure 4.11 Experimental Process flowchart

The strategy was simple: print a sample at a given layer thickness and check for slip casting on the surface. As long as no slip casting is observed, increase the number of applications per layer (multiple printing). Once casting is observed, that establishes the maximum number of applications per layer. Subsequently, move to a finer layer and repeat the process. The samples would then be sectioned and checked for uniformity.

The method outlined in figure 4.11 arose from observations of slip casting phenomena during some test runs using the larger 70 micron nozzle and some built-in 3DP process

constraints. With a 70 micron nozzle and standard 3DP conditions (170 micron line spacing and 170 micron layer thickness), the higher flow rate causes saturation conditions, and TiC is easily observed on the surface of the bed after printing. Logically, any presence of TiC on the surface would result in an interlayer defect because the TiC would occupy the space were the next layer would be spread. An interlayer defect is the absence of large powder particles at the interface between layers.

With the interlayer defect check in place, the next issue was which process variables would be altered, besides the layer thickness. In the 3DP process, the flow rate is typically fixed, at 0.8-1 cc when using a 50 micron nozzle. The only two other "real" variables were the layer thickness and the line spacing. Lowering the line spacing would lead to a saturation condition because the current parameters (170 micron spacing and 170 micron layer thickness) are basically at the saturation point. Raising the line spacing would move us away from the goal of higher densities since less material would be deposited in a region. As such, the only tangible variable was the layer thickness. Moving to finer layers would yield higher densities with little fear of saturation (fixed flow rate) because the excess liquid would migrate downwards, into previously spread layers, and not sideways because the line spacing had also been left unchanged.

Regarding the achieved green density, it could easily be calculated since the flow rates and starting packing fraction would be known apriori.

4.3.2.1.1 Printed Sample Preparation Procedure

The other piece of the puzzle was the microstructure of the printed samples themselves. How homogenous were they? This could only be answered by viewing cross section s of the samples under high magnification. To do this, a sample preparation procedure followed by Steve Gregorski for Stainless Steel was adapted (Gregorski, 326-327).

All printed Molybdenum-TiC samples were sintered at 1300°C for 45 minutes in forming gas. The samples were then infiltrated at 170°C with a high strength 3M one part epoxy

(3M PR-500). This was done to fill the void space and trap the particles in place for subsequent sectioning and polishing.

After the samples were sectioned with a low speed diamond saw, they were subsequently potted for polishing. Polishing involved beginning with wet grinding on a 15 micron alumina diamond wheel, and subsequent lapping with diamond paste. The polishing sequence, including pressures, times, and diamond paste particle sizes is listed below (Table 4.2).

Diamond Paste Size (microns)	Polishing Time (min)	Polishing Pressure (psi)	Platter rpm
9	5	10	120
6	5	10	120
3	5	10	120
2	5	10	120
1	5	10	120
¼	5	10	120

Table 4.2 Polishing procedure for Molybdenum-TiC samples infiltrated with epoxy.

Using this lapping procedure with diamond paste as opposed to the traditional silicon carbide wet/dry paper is important because of the hardness of the fine TiC particles. With Silicon Carbide, the TiC particles would not be sheared, but dislodged and smeared. And as a result, SEM's of the microstructure would not accurately represent the "as printed" location of the TiC particles. The only drawback with utilizing the diamond paste is the higher than usual number of pullouts of Molybdenum particles from the matrix. This however is not a major concern because the shapes of the pullouts would be the same as the spherical particles. Thus when observed under an SEM, an accurate representation of the microstructure could be inferred even from a sample with multiple pullouts.

4.3.2.2 Results and Analysis of Quickee Machine Printing

All experiments performed on the Quickee machine were performed using a 20 volume fraction TiC slurry (with added Duramax to serve as binder), with the flow rate held fixed at 0.89 cc/min or 1.25 gms/min. The first order of business was to establish the maximum # of times a given layer could be printed into before TiC could be observed on the powder bed surface. Beginning with the approximately the standard 3DP process conditions, 170 micron line spacing and 7 mil layer thickness, layers were spread and printed into the desired number of times (with drying in between each application). After two layers were spread and printed into (one foundation layer), the powder beds were then observed under a microscope for evidence of slip casting. After the third printing application, the powder beds consistently exhibited evidence of slip casting on the surface. This established the upper limit for the multiple application option, only two applications were possible. The results with thinner layers, 5 mils and 4 mils, were similar as expected. This was consistent with the 86% upper bound for bimodal densification discussed in Section 2.1.1.2. All triple printed samples except the 7 mil layer thickness case would be above this ceiling and expectedly, slip casting would ensue.

After flushing out the maximum number of applications issue with the TiC slurry, the next step was to examine samples printed at various process conditions, i.e. single printing vs. double printing, and thinner layers. The samples would be studied under a Scanning Electron Microscope for evidence of obvious interlayer defects and periodicity in the particle deposition.

Three layer thickness' were selected for experimentation: 7 mils, 5 mils and 4 mils. Representative SEM images of some of the cross sections are included below (See figure 4.12 a-d) along with a summary tabulation of the observations recorded about each cross section (See Table 4.3). In the SEM images, the larger, lightly colored spherical powders are the Molybdenum powders, while the fine, gray powders are TiC particles. The dark region in the images is the epoxy infiltrant. The pullouts are the dark circular "holes",

typically with a light outline. Note that the scale bar in each image measures 200 microns.

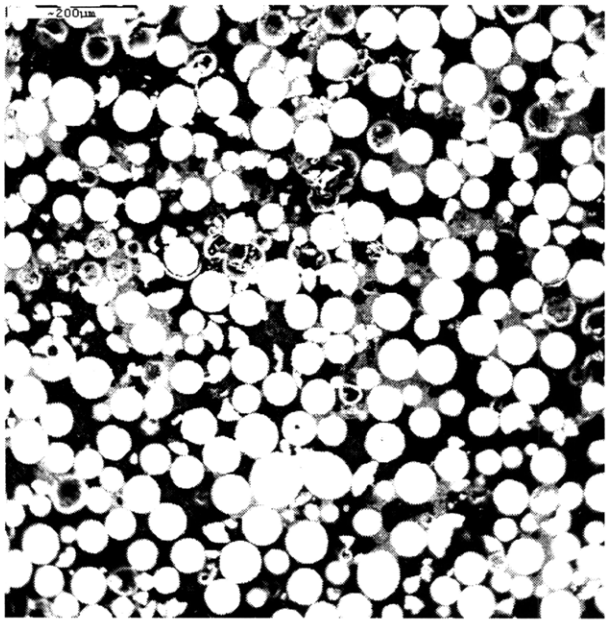

Figure 4.12 a) 7 mil, Single Printed Molybdenum-TiC Section

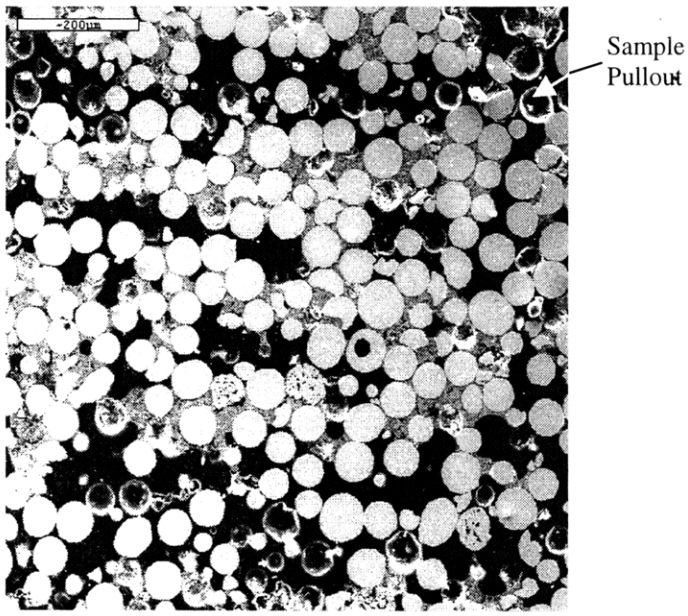

b) 7 mil, Double Printed Molybdenum-TiC Section

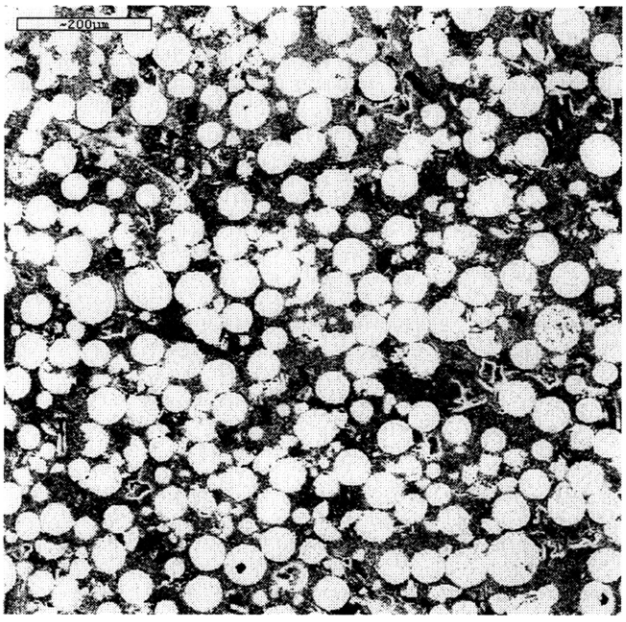

Figure 4.12 c) 5 mil, Double Printed Molybdenum-TiC Section

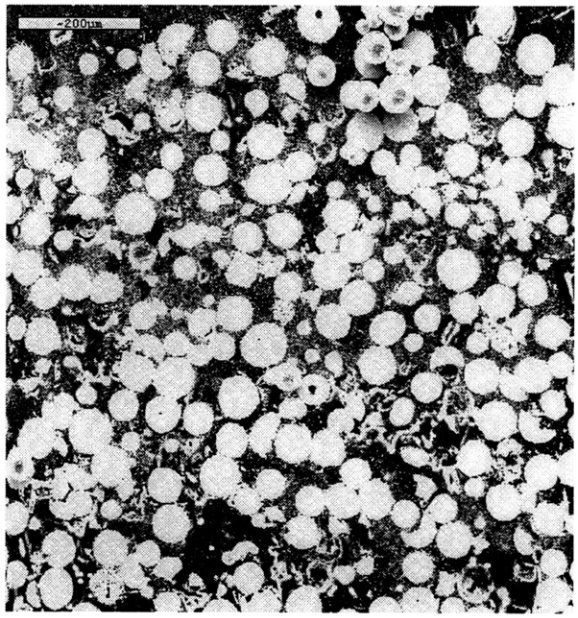

d) 4 mil, Double Printed Molybdenum-TiC Section

(All Samples Printed at 172 micron line spacing).

Sample Process Conditions	Estimated Green Density (assuming initial 60% packing)	Pullouts Observed?	Obvious Periodicity?	Comments
7 mil, Single Print	0.66	Several Pullouts	Yes	No apparent interlayer defects
7 mil, Double Print	0.73	Several Pullouts	Yes	No apparent interlayer defects, but uneven packing.
5 mil, Single Print	0.68	Few Pullouts	Yes	No apparent interlayer defects
5 mil, Double Print	0.77	Few Pullouts	Unable to discern if periodic	No apparent interlayer defects
4 mil, Single Print	0.71	Few Pullouts	No apparent periodicity	No apparent interlayer defects, difficult to spread layers during printing.
4 mil, Double Print	0.83	Few Pullouts	No apparent periodicity	No apparent interlayer defects, difficult to spread layers during printing.

Table 4.3 Summary of Results from Study of Printed Molybdenum-TiC Sections

The comments made regarding the absence of apparent interlayer defects, should be prefaced, because of the poor and sometimes uneven packing of the samples produced on the Quickee machine. Uneven packing would not allow for a clear demarcation between the layers.

4.3.3 Alpha Machine Printed Coupons

The samples fabricated on the Quickee machine had demonstrated that layer thicknesses

of 5 mils or below were the most likely to be homogeneous. With this in mind, the decision was made to print samples on the 3DP alpha machine at various conditions, but with the emphasis on coupons of 4 mil layer thickness. Moving to the Alpha machine also provided the additional benefit of ensuring an initial packing density of 60 percent (for the estimated green density calculation). The samples printed on the Quickee machine were spread by hand with a roller bar supported by gauge pins. Not only did this not afford for repeatable spreading, but it was also impossible to simulate the high frequency vibration of the alpha machine roller that would compact the powder as it traversed. It is this vibratory compaction that produces repeatable pack densities of 58-60% for spherical powders.

4.3.3.1 Printing Issues on Alpha Machine (evolved gas and bubbling)

In the process of printing the Molybdenum-TiC coupons on the alpha machine, several problems were encountered, chief amongst them was a bubbling phenomena. After several minutes of printing, bubbles of air would periodically exit the nozzle. In addition, when the nozzle capillary was observed under a microscope, several tiny bubbles were seen clinging to the inner walls. The presence of these bubbles made it impossible to reliably charge and deflect the slurry droplets into the catcher as was frequently necessary for continuous jet printing. In CJ printing, each droplet is charged, fully deflected into the catcher if it not supposed to strike the bed, or not deflected at all if it is supposed to strike the bed. There were two possible sources of the bubbles: (1) air introduced to the slurry chamber during refills, and (2) dissolved air within the slurry being released as the slurry experienced the pressure drop across the fluid lines. The latter reason seemed more likely because similar phenomena had not been observed on the Quickee machine. The capillary lengths used on the Quickee machine were about one foot long as opposed to the eight foot length employed on the Alpha machine. The longer lines meant a substantial increase in the pressure drop, and an increased likelihood of bubbling.

To eliminate as many causes of bubbling as possible and at the same time still obtain some samples, the following precautions were taken:

1. No refills: start with a fixed volume and fail to introduce new material and possibly gas.
2. Degas the slurry in the pressure vessel by pulling a vacuum.
3. Use helium instead of air to pump fluid. This was done because of the lower solubility of helium in water, as compared to air.
4. Employ mask printing instead of charge and deflection, in case 1-3 fail to eliminate the bubbling phenomena. Mask printing involves placing a supported aluminum plate with a rectangular hole over the powder bed during printing in order to define the geometry (See figure 4.13).

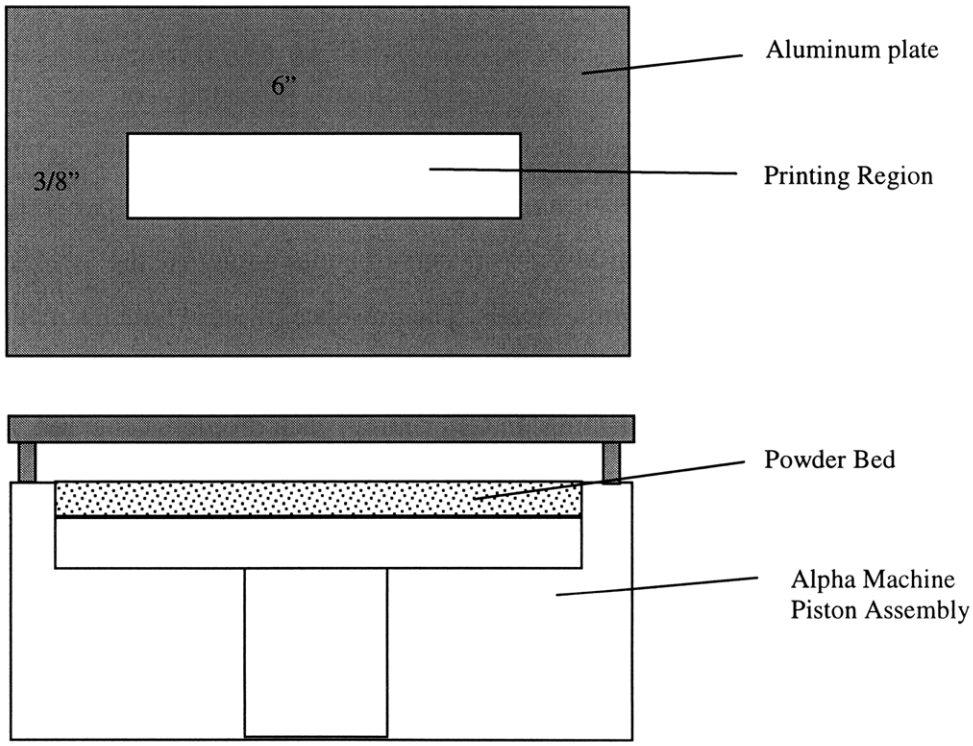

Figure 4.13 Mask and Piston Assembly

The decision to use the mask to produce the coupons essentially meant that we would be using the alpha machine in very much the same fashion as the Quickee machine, with the benefit of vibration and large samples.

4.3.3.1.1 Effect of Pressurized Helium and Slurry Degassing on Slurry Bubbling.

As printing commenced, observations were made regarding occurrence of bubbles and the use of pressurized helium as opposed to air. There was a marked improvement; the frequency of observed air bubbles lowered from approximately every 5 minutes to about every half –hour.

4.3.3.1.2 Final Printing Setup for Slurry Dispensing.

Although benefit was achieved for the helium-degassing procedure with no refilling, it was abandoned because some settling was observed in the vessel after several hours of printing. For long runs, refilling would be necessary. In addition, there seemed to be an unexplained increase in the frequency of clogging. As such the following setup was used in an effort to minimize the introduction of air into the slurry (See figure 4.14). In this setup, the slurry was not in contact with air, and could still be refilled with the aid of a pinch valve and refill line.

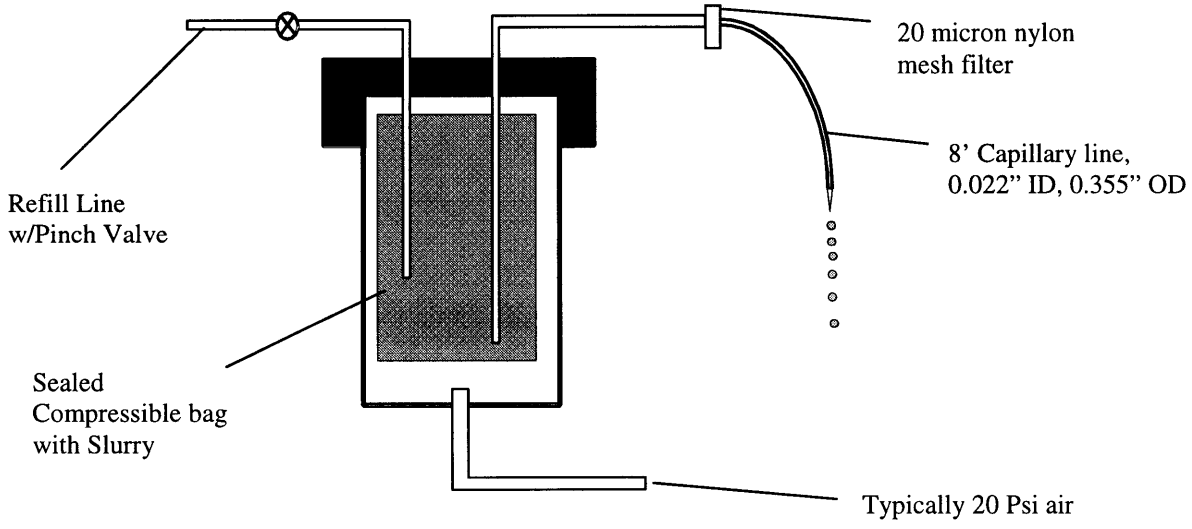

Figure 4.14 Final Slurry Dispensing Setup

With this scheme in place, there was little evidence of bubbling phenomena, though it was still occurring. In addition, the persistent clogging was not a problem with this setup.

Only the usual initial startup clogs were experienced. The clogging observation however doesn't reveal much, as the previous helium-no refill procedure was not used with the same slurry.

4.3.3.2 Part shifting and Layer Compaction Problems during Printing.

Another problem observed when printing samples with thin layers, i.e. 100 (approx. 4 mils) and 132 microns (approx. 5 mils), was part shifting. As a new layer was being spread, the part would shift in the bed. Upon closer inspection, it was determined that the roller was striking the part (See figure 4.15).

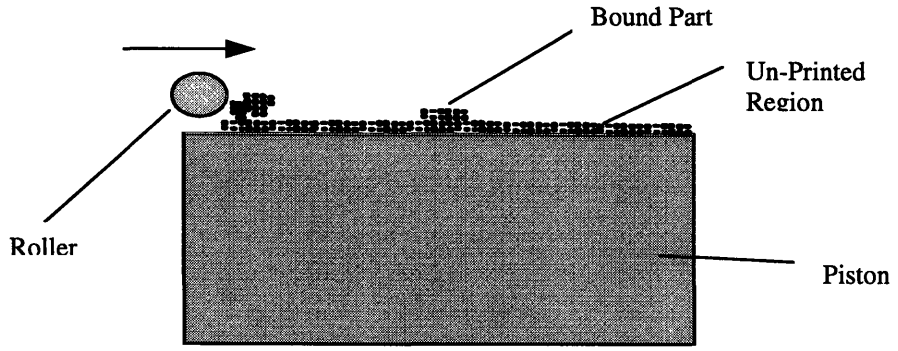

Figure 4.15 Non-uniform layer compaction

This was because that the layers were so thin (2 –3 particle diameters) that the powders comprising the bound printed region could not be compacted effectively to define a uniform layer height. On some samples, after only two or three layers, the part would dramatically shift in the bed as the roller struck it. This usually resulted in the part cracking severely on the subsequent layer. The part shifting problem effectively limited builds to only a few layers. This limitation must be overcome before larger parts are printed. One solution is to use finer powders, but for the purposes of this work, this was not extensively explored as the penetration characteristics of the slurry would be quite different and would not correlate with previously printed samples. However, some builds were large enough (at least 10 layers) for some process conditions examined on the

Quickee machine to be duplicated. The analysis of their cross sections is discussed in the following section.

4.3.3.3 Results and Analysis of Alpha Machine Coupons

As on the Quickee machine, experiments on the Alpha machine were performed using a 20 volume fraction TiC slurry (with added Duramax to serve as binder), with the flow rate held fixed at 0.89 cc/min or 1.25 gms/min. The samples were then processed in the same manner as before for SEM imaging. A summary of the observations regarding the surviving samples is presented below (Table 4.4), along with representative images (figures 4.16 a-j). For each condition, special care was taken when observing the tops of the samples. The absence of TiC at the surface would serve as added assurance that the sample was free of interlayer defects.

As expected, the Alpha machine samples demonstrated higher large particle packing than the Quickee machine samples, with increased uniformity. This was evident after visually comparing the microstructures. Aside from the compaction issue, the 4 mil-Double print sample demonstrated the most uniformity in fine particle deposition and no periodicity could be observed. This is because it was closest sample to the maximum bimodal densification limit of 86% (See section 2.1.1.2), i.e. as good as it gets. In effect, the closer to this upper limit, the more uniform the structure.

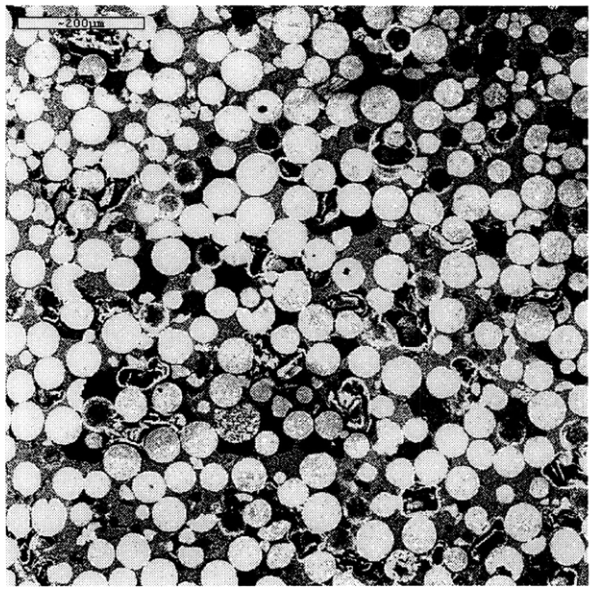

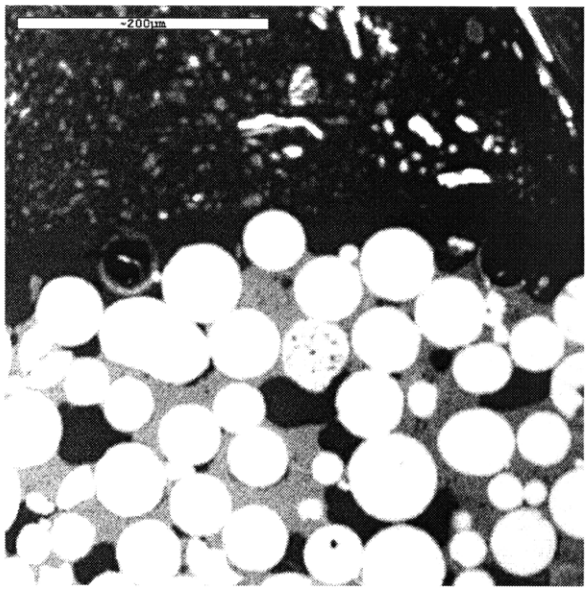

Figure 4.16 a) 4 mil, Double Printed Molybdenum-TiC Section; 200 micron scale bar. **b)** Top Surface of 4 mil, Double Printed Molybdenum-TiC Section; 200 microns scale bar.
(All samples printed at 170 micron line spacing)

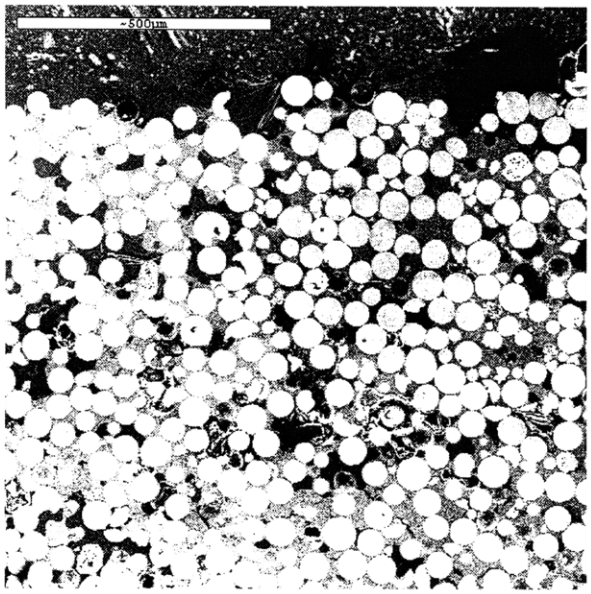

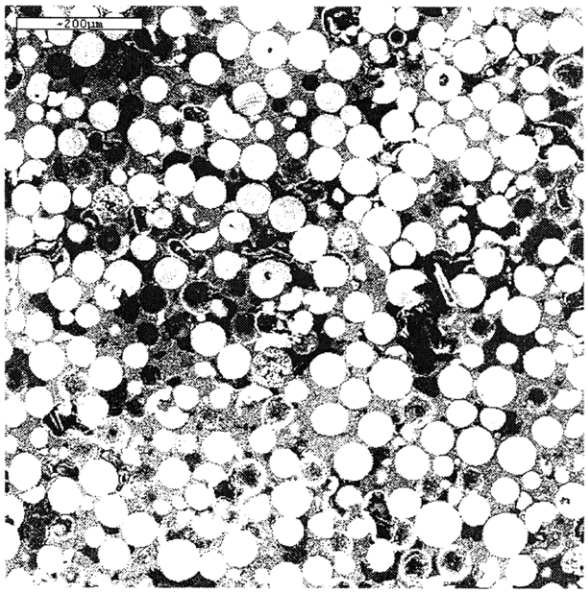

Figure 4.16 c) 4 mil, Double Printed Molybdenum-TiC 500 micron scale bar. **d)** 4 mil, Double Printed Molybdenum-TiC Section; 200 microns scale bar.
(All samples printed at 7 mil/170 micron line spacing)

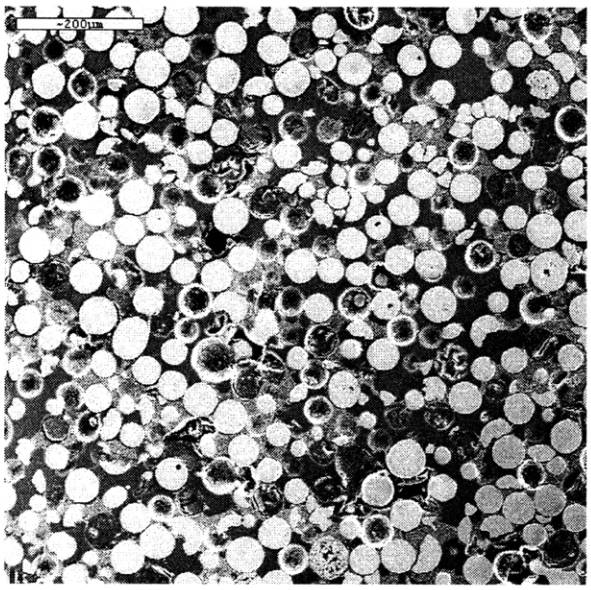

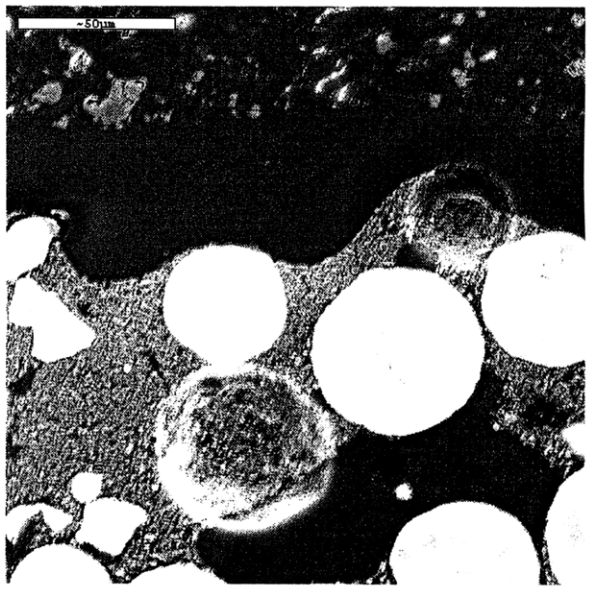

Figure 4.16 e) 5 mil, Single Printed Molybdenum-TiC Section; 200 micron scale bar. **f)** Top Surface of 5 mil, Single Printed Molybdenum-TiC Section; 50 micron scale bar.
(All samples printed at 170 micron line spacing)

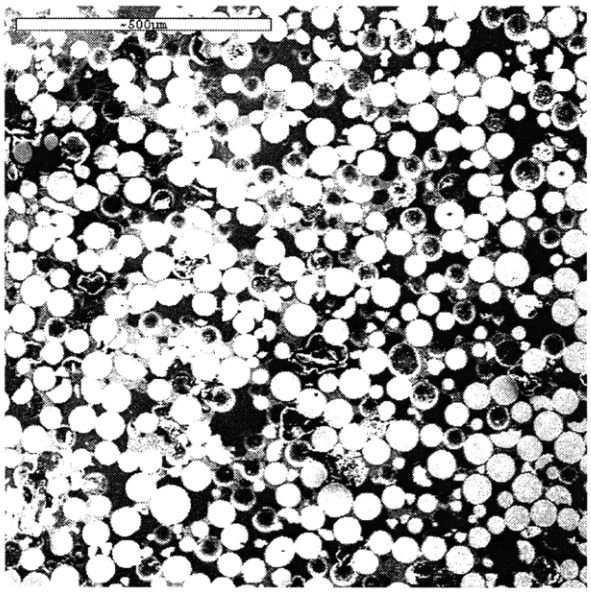

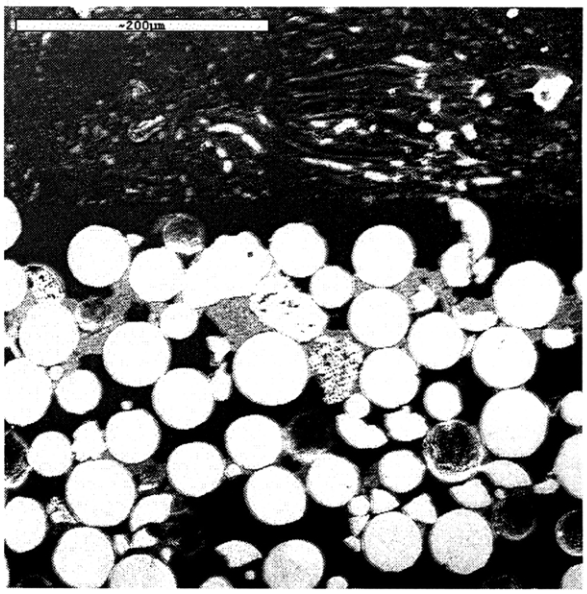

Figure 4.16 g) 7 mil, Single Printed Molybdenum-TiC Section; 500 micron scale bar.

h) Top Surface of 7 mil, Single Printed Molybdenum-TiC Section; 200 microns scale bar.

(All samples printed at 170 micron line spacing)

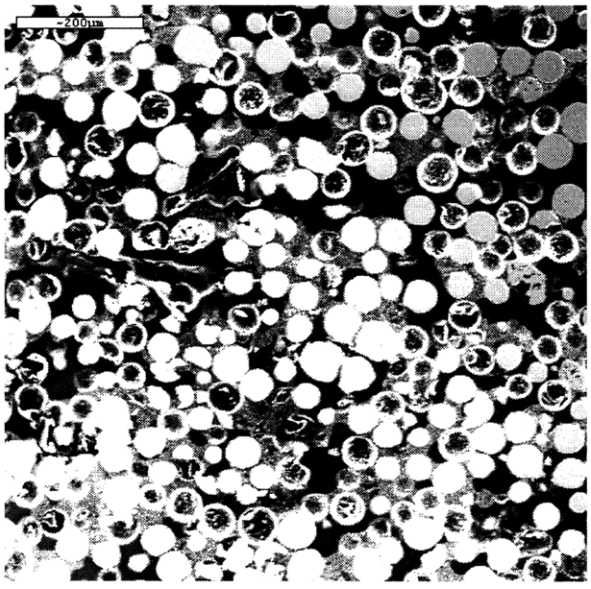

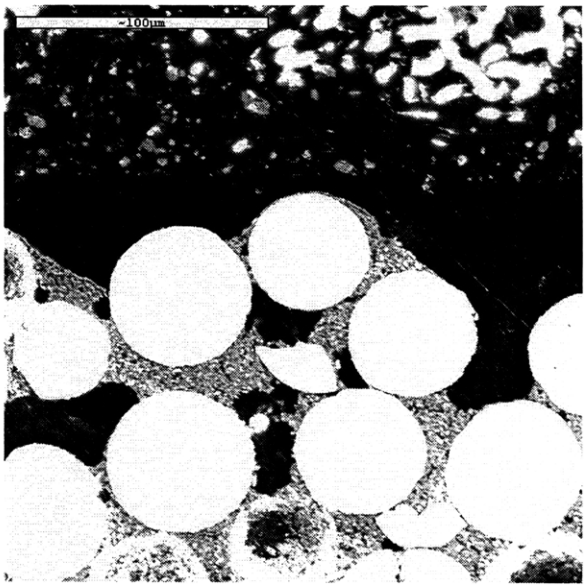

Figure 4.16 i) 7 mil, Double Printed Molybdenum-TiC Section; 200 micron scale bar.

j) Top Surface of 7 mil, Double Printed Molybdenum-TiC Section; 100 microns scale bar.

(All samples printed at 170 micron line spacing)

Sample Process Conditions	Estimated Green Density (assuming initial 60% packing)	TiC on Surface?	Obvious Periodicity?	Comments
7 mil, Single Print	0.66	No	Yes	No apparent interlayer defects
7 mil, Double Print	0.73	No	Yes	No apparent interlayer defects, but uneven packing.
5 mil, Single Print	0.68	No	Yes	No apparent interlayer defects
4 mil, Double Print	0.83	No	Not Periodic	No apparent interlayer defects

Table 4.4 Summary of Alpha Machine Printed Coupons

For completeness, 4 and 7 mil Molybdenum controls (without TiC) were printed with the Acrysol binder. The 4 mil sample also demonstrated the part shifting phenomena that had been previously observed. SEM images of the 4 and 7 mil samples are provided for comparison (See figure 4.17 a, b). As expected, with the diamond paste, there was evidence of pullouts.

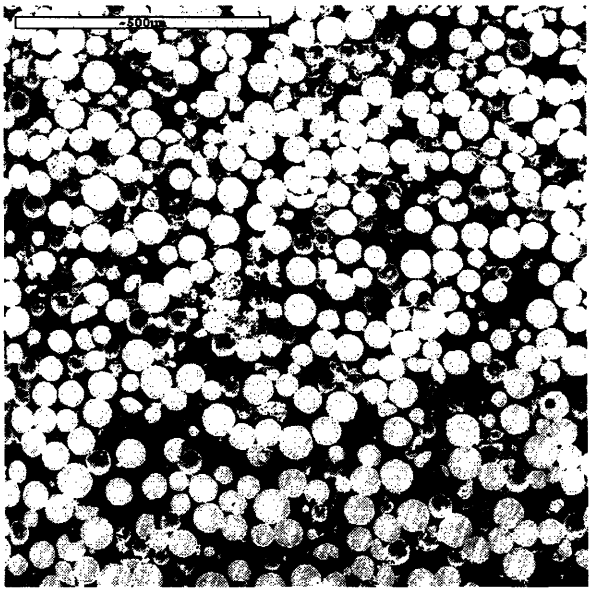

Figure 4.17 a) 4 mil layer, Molybdenum Control Sample, bound with Acrysol. (500 micron scale bar).

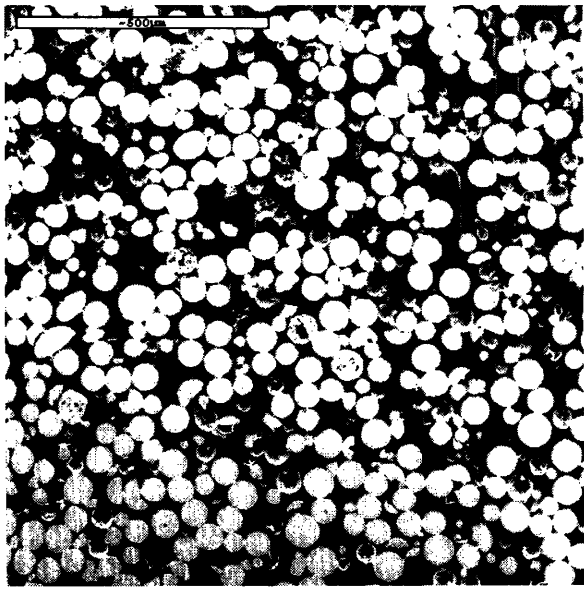

b) 7 mil layer, Molybdenum Control Sample, bound with Acrysol. (500 micron scale bar).

4.3.3.4 Alpha Machine Coupons Revisited

Due to the difficulty associated with spreading thinner 4 mil layers, an attempt was made to achieve the same penetration effects at the standard, 7 mil layer thickness. The slurry flow rate was increased by a factor of 7/4 to compensate for the larger layer size while the line spacing was left unchanged at 170microns. This effectively added the same total volume of slurry as had been previously added to the 4 mil layers. The dramatic increase in flow rate increased the risk of introducing bleeding and edge definition problems since layer saturation limits had been exceeded. The hope was that the slurry would migrate downward at a faster rate than it would spread sideways. Bleeding proved to not be an issue as the edges of the coupons were well defined. However, unlike with the 4 mil layer samples, double printing was not possible as slip casting was evident on the top surface after the second application. Since the total volume of slurry added was the same in both cases (7 mil vs. 4 mil), some of other variable had changed to explain the casting effect. Two possibilities exist here. The most likely possibility is that packing fraction was lower on the 4 mil samples because of the thin layer spreading problem. This would leave more open space that could be filled on the second pass in the 4 mil sample than the 7 mil sample. The second possibility was that (in the case of the 7 mil layer sample) fine particles in the slurry were essentially being filtered out at certain depth and did not reach the open space below on the second pass and simply built up close to the surface.

The 7 mil, saturated sample was subsequently sectioned an observed in the same manner previously discussed (4.3.2.1.l). The results are shown below in figures 4.18 a, b. They indicate that though there is no clear vertical periodicity (Figure 4.18 a) or TiC on the surface (Figure 4.18 b), the fine TiC powders are quite clustered and unevenly distributed. This suggests that spreading thinner layers and having a lower flow rate, though conceptually similar, is better for uniformity and hence are a better option whenever possible.

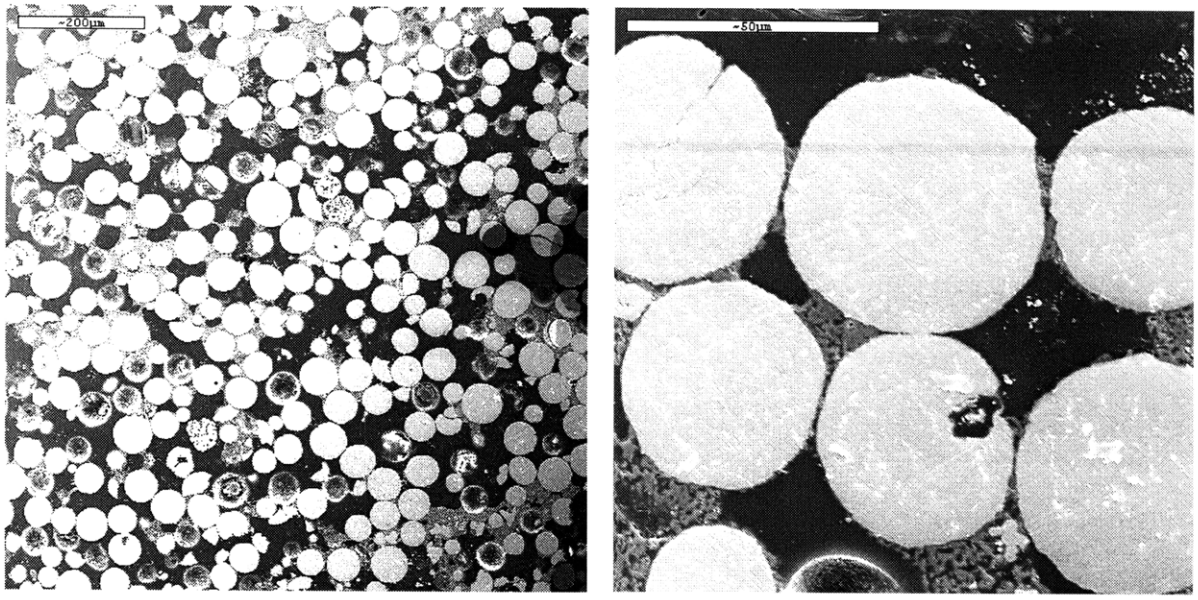

Figure 4.18 a) 7 mil, Single Printed Molybdenum-TiC Section; 200 micron scale bar. **b)** 7 mil, Single Printed Molybdenum-TiC Section; 50 microns scale bar.
(All samples printed at 7 mil/170 micron line spacing)

4.4 Summary

Chapter 4 documents the determination of printing parameters for the fabrication of high density, homogeneous bimodal parts free of interlayer defects. In addition, issues related to the subsequent infiltration of bimodal parts were extensively explored. The issue of trapped gas caused by differing infiltration rates in bimodal parts was explored, using Titanium Carbide and Tungsten Carbide bimodals as case studies. The effect of varying the relative concentration of large to fine powders in bimodal samples was also investigated in the context of these case studies. Finally, basic observations were made about the deposition pattern of printed fine TiC particles in large powders.

Chapter 5: Development of Bimodal Systems

5.1 Background

Alongside with the work on developing a reliable dispersion of titanium carbide particles for printing, significant effort was devoted to developing a complete material system. By material system, I refer to the combination of sintered titanium carbide, base powder compact and to the infiltrant added in the latter step.

5.2 TiC-TiC Systems

5.2.1 Motivation

After some initial experimentation with Steel-TiC based systems, much of the early materials work focused on developing a TiC-TiC system, i.e. a sintered bimodal titanium carbide mixture, infiltrated with a copper alloy. Limiting the scope in this manner was done to eliminate the complexity associated with developing material systems based on dissimilar powders. Prior to this, the obstacle had been finding a suitable infiltrant that was minimally reactive and still demonstrated good wetting properties with the powders. Focusing on TiC bimodals afforded more flexibility when it came to the reactivity issue.

5.2.2 Sintering TiC-TiC Bimodals

Sintering of the bimodal titanium carbide mixtures was undertaken by drawing upon the reactive binding concept first investigated by Helen Yoo. Yoo demonstrated that fine iron carbonyl powders (as slurry) could be selectively printed into large steel powders and the entire bed fired to a temperature sufficient to sinter the carbonyl rich region only. The result was a compact that was "reactively bound" and could be removed from the powder bed for subsequently infiltration. An analogous procedure was possible with the fine TiC slurries and large TiC base powders. The mechanism would in fact be simpler, because

no chemical reaction would take place since the powders were of the same type. It was a simple matter of sintering the fine powders to hold the compact together.

To fully understand the mechanism, a brief background on sintering theory is offered below:

Sintering is a diffusion driven process, were the individual particles in contact develop necks and bond at elevated temperature with minimal shrinkage and distortion. Sintering can be broken up into three stages based upon the degree of neck formation and pore characteristics. The key parameter of interest, is the neck to size ratio (see figure 5.1)

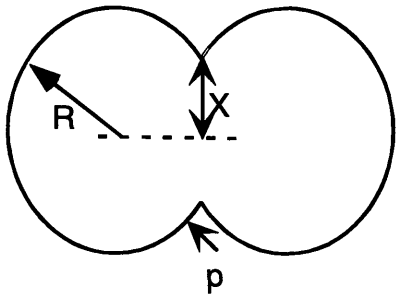

Neck to size = X/R

Curvature (p) = $X^2/2R$

Figure 5.1 Illustration of Sintering with essential geometric relations

The initial stage is dominated by interconnecting pores and a neck size ratio of less than 0.3 while the intermediate and final stages are characterized by cylindrical and circular pore structures respectively.

The initial sintering stage is the key stage of interest in minimizing the shrinkage of the part and maintaining its geometry. This is because the dominant mass transport mechanism during the initial stage of sintering is usually surface transport. Surface transport involves migration of mass at the particle's surface and slight dimensional change but results in satisfactory neck formation. In addition, because the compact's pores remain "open and fully interconnected" in the initial stage, subsequent infiltration is not hindered. Neck growth during the initial phase is usually modeled as a sum of terms of the following form, each representing a particular mechanism of mass transport, i.e. surface diffusion, grain boundary diffusion etc (German, 250-251).

$$\left(\frac{X}{R}\right)^n = \frac{Bt}{R^m} \qquad 5.1$$

These particular relationships are valid for neck size ratios below 0.3. Further more, these relationships also illustrate the significant role that particle size plays in sintering. Simply put, fine particles sinter at a substantially faster rate than large particles. This is due to the exponential nature of the relationship.

For extremely fine powders (sub-micron), surface diffusion plays an even more dominant role in determining the sintering rate during the initial stage, and usually determines much of the sintering rate. However, to get an accurate picture of the degree of sintering, all sintering mechanisms must be taken in concert. By identifying the mechanisms at work for a given particle size and temperature range, it is possible to build a material's overall sintering map. Chermant et. al. undertook this exercise and were able to build sintering maps for Titanium Carbide particles of various sizes (See figures 5.2 a, b).

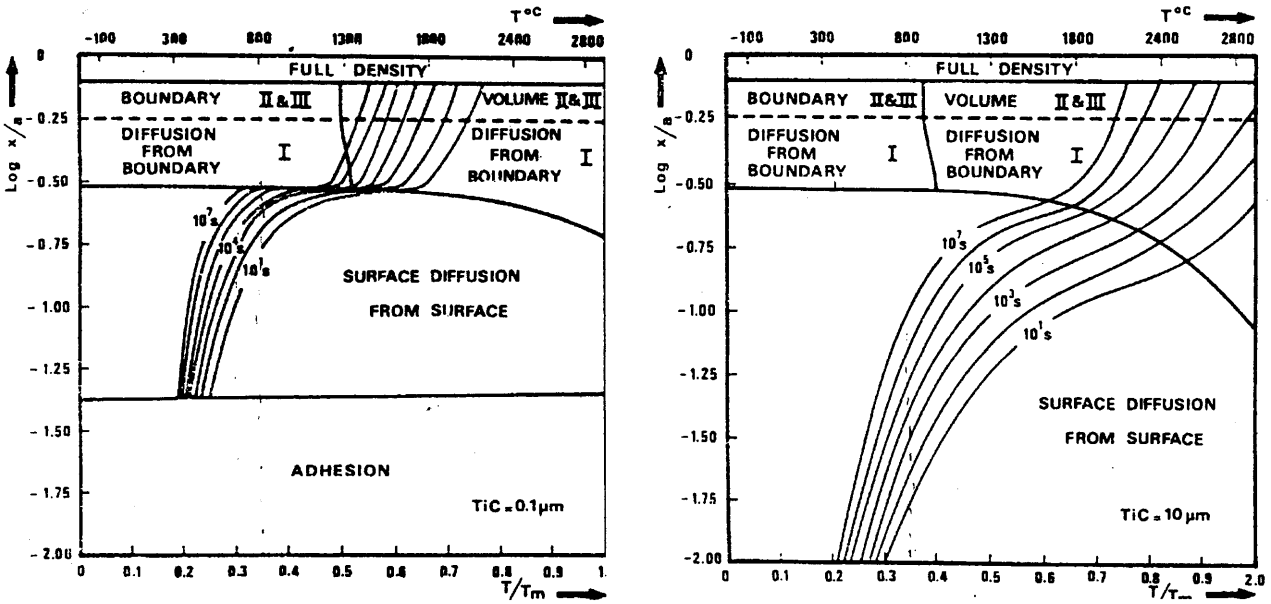

Figure 5.2 a) Sintering Map for 0.1μm Titanium Carbide. **b)** Sintering Map for 10μm Titanium Carbide. (Courtesy Chermant, et. al, 173)

These maps provide an excellent guide for selecting an appropriate temperature and time recipe for sintering titanium carbide particles. They plot the logarithm of the neck size ratio (the vertical axis) as a function of T/T_m, the ratio of temperature to melting point,

with the time held constant. The time is frequently expressed in seconds. Also included in the plots are indications of the regimes in which particular sintering mechanisms are dominant.

As mentioned before, the region of interest is the regime in which surface diffusion is dominant. However, because these maps are for given mean particle size, it was necessary to generate sintering maps or at least representative curves for the particular sizes of the slurry powder and the base powder. Figure 5.3 is a plot of temperature vs. the predicted neck growth ratio for both powders, after a thirty minute sintering treatment.

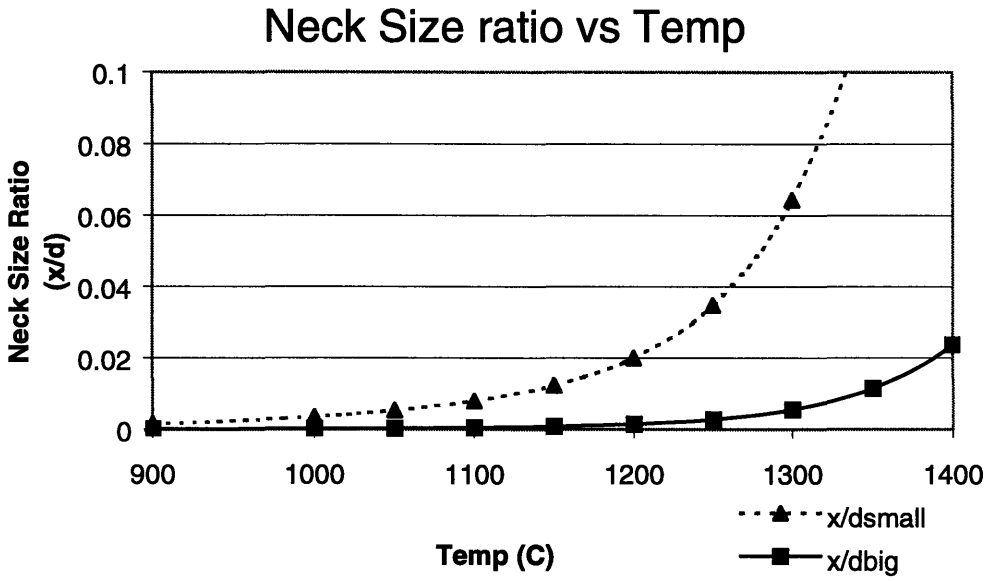

Figure 5.3 Predicted Neck Size ratio vs. Temperature for 0.8 micron and 74 micron Titanium Carbide particles (Sintered for 30 minutes)

A more detailed summary of the procedure to generate similar curves, including the specific relations and material property data is offered in Appendix B.

With this scheme in place, the next step is to convert the predicted neck size ratio to an equivalent prediction for the shrinkage of a compact (See figure 5.4) using the following geometric relationship (German, 252):

$$shrinkage = -\frac{\Delta l}{l} = \left(\frac{x}{r}\right)^2 \qquad 5.2$$

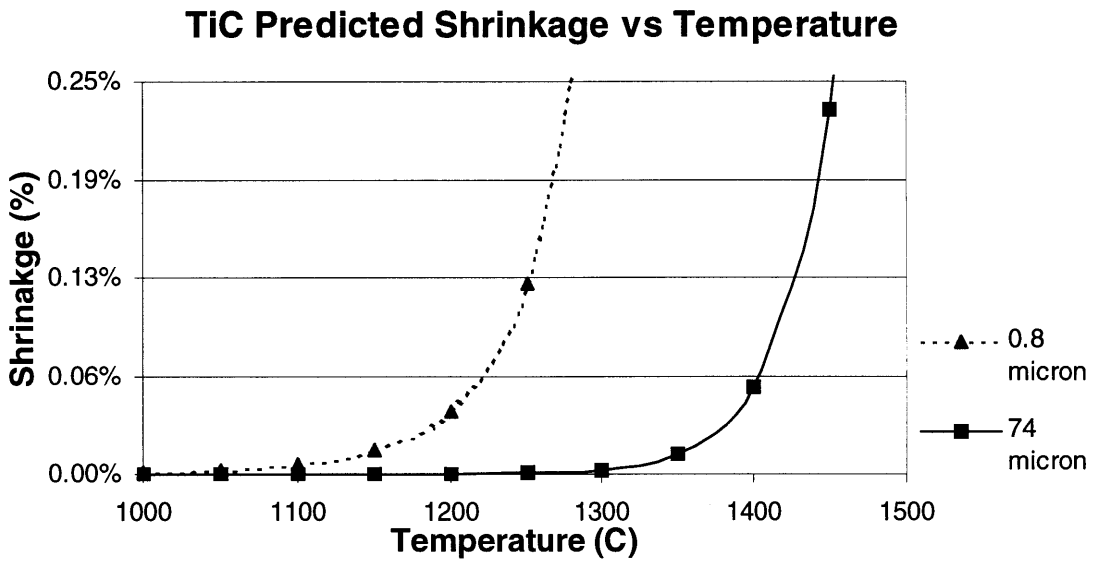

Figure 5.4 Predicted Shrinkage vs. Temperature for 0.8 and 74 micron TiC powders (30 minute sintering time).

The shrinkage predictions indicate that the onset of sintering occurs at approximately 1050 – 1100°C and 1300 – 1350°C for the 0.8 micron and 74 micron TiC powders respectively. As such, there was at least a two hundred degree window, giving us sufficient cushion before the unprinted region would begin to sinter. Furthermore, the predicted values assume a uniform bed of fine particles, as opposed to the bimodal bed that results after pipetting in the TiC slurry. Thus this is a high estimate for the shrinkage, and the sintering window is in fact larger.

To prove the accuracy of the model and demonstrate the process, a basic sintering experiment was devised. Tiny silicon carbide posts (approximately 4 mil in diameter) were embedded in a bed of loose 74 micron TiC powders. A 15 volume fraction titanium carbide slurry was subsequently pippetted into the region between two adjacent posts to

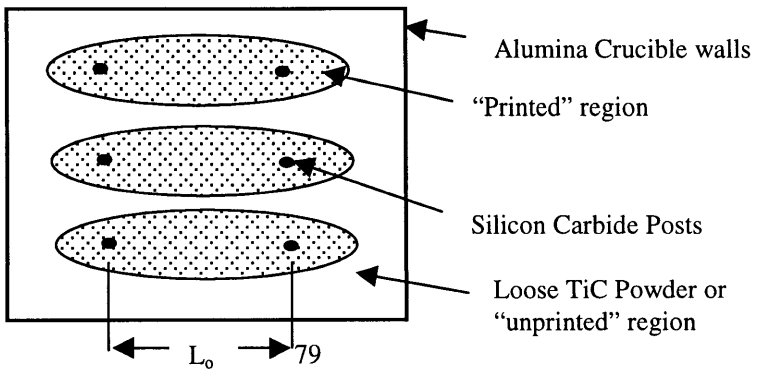

Figure 5.5 Pin Layout of TiC shrinkage experiment in powder bed

form a "printed" region (See figure 5.5). The distance between the posts was recorded for later shrinkage calculations and the entire bed was fired at 1100°C for 30 minutes in Forming gas (5% Hydrogen, 95% Argon).

After firing, the bound printed regions was easily removed from the powder bed and demonstrated exceptional strength. As a qualitative strength measure, the compacts were ultrasonicated to promote failure or breakage. No failures occurred and the compacts were pronounced sound. The distances between the silicon carbide pins were also measured and shrinkage values calculated. The results, summarized in table 5.1, indicate shrinkages on the order of hundredths of a percent, corresponding well with the predicted values. It should be noted however, that the error in measurement was approximately a tenth of a percent, limiting the accuracy with which we could relate the predicted shrinkage values to the experimentally determined values.

Sample #	Recorded Shrinkage (-ΔL/L) (3 measurements/sample)	**Average Shrinkage +/- error**
A	0.035%	0.07% +/- 0.1%
	0.110%	
	0.069%	
B	0.019%	0.00% +/- 0.1%
	0.045%	
	-0.077%	
C	-0.028%	0.05% +/- 0.1%
	0.070%	
	0.105%	

Table 5.1 Shrinkage results for bimodal TiC compacts fired at 1100C for ½ hr

5.2.3 Infiltration of TiC-TiC Bimodals

Once the binding/sintering mechanism had been investigated to satisfaction, the next step was infiltrating the sintered TiC-TiC bimodal compacts to full density. The key issue was identifying an appropriate metal infiltrant that would wet the TiC surface. Briefly, the

degree of wetting is determined by the contact angle (θ) of the liquid on the solid surface, expressed in Young's equation (Goetzel, 551):

$$\sigma_{SV} - \sigma_{SL} = \sigma_{LV} \cos \theta$$

where σ_{SV}, σ_{SL}, and σ_{LV} are the surface energies associated with the solid-vapor, solid-liquid, and the liquid-vapor interfaces. Good wetting is exhibited by solid-liquid interactions that result in contact angles close to zero. Poor wetting is indicated by large contact angles, typically greater than 90 degrees.

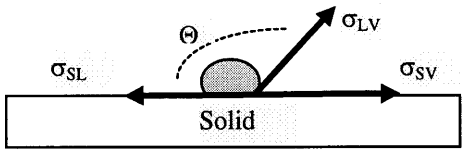

Figure 5.6: Surface forces acting on a liquid resting on a solid

In an effort to determine an adequate infiltrant, a focused series of infiltration experiments were performed with sintered, porous titanium carbide compacts and various copper alloys. The copper alloys were selected based on existing industrial practice and a literature review.

5.2.3.1 Description of Infiltration Procedure and Results:

All infiltration tests were performed in a tube furnace for 1/2 hour at temperatures ranging from 1120-1150°C in a 95% Argon, 5% Hydrogen atmosphere. Furnace ramp rates during all infiltration tests were held fixed at 5 °C/min.

Infiltrant Candidate	Infiltrates TiC (Y/N)	Infiltrant Melting Point (^{o}C)	Infiltration Temp (^{o}C)	Comments
Copper Shots	N	1083	1150	Wet Surface, didn't penetrate.
Cu-20Mn-20Ni Alloy	Y	1080	1120	Excellent Wetting, Complete infiltration.
Cu-20Ni Alloy	N	1180	1200	Wet surface, didn't penetrate.
3DP Bronze (90Cu-10Sn)	N	1020	1120	No Wetting.

Table 5.2 Results of Infiltration experiments

From these results, a copper-nickel-manganese alloy was selected. A cross-section of the resulting microstructure is shown in figure (5.7) along with a summary of the processing

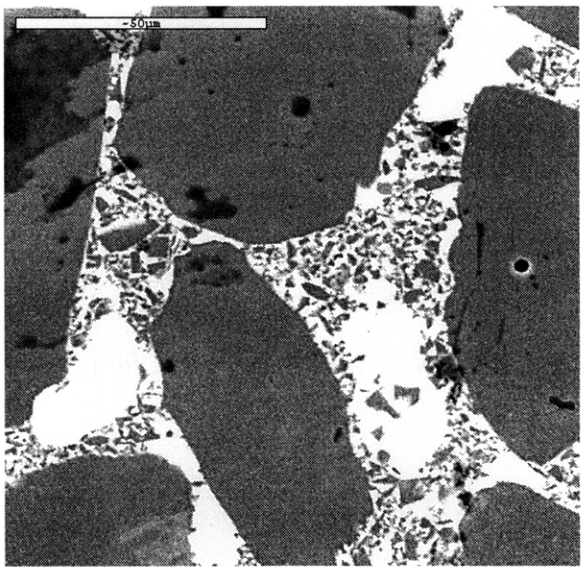

Figure 5.7 Bimodal TiC infiltrated with Cu-Ni-Mn alloy in vacuum (50 micron scale bar).

steps (figure 5.8). Note that the sample shown and the processing steps indicate that vacuum infiltration is preferable. This refinement on the existing infiltration scheme was

necessary after tiny voids were found in some samples infiltrated in forming gas (see section 4.2.1).

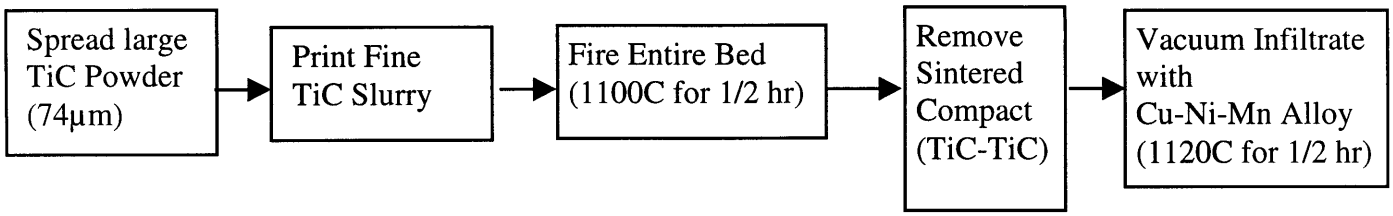

Figure 5.8 Process Overview for Infiltrated Bimodal TiC

5.2.3.2 Age Hardening Response of Infiltrated Bimodal TiC Composites.

An additional benefit of using copper-nickel-manganese as an infiltrant was its age hardening property. After a 12 hour heat treatment at 400°C, the alloy can be hardened from 80 Rockwell B to approximately 35 Rockwell C (Zubin Irani, personal communication). This offered the potential of fabricating hard bimodal tools. A summary of the hardening response is provided below in table 5.3.

Macro Hardness after Infiltration	28-31 RC
Macro Hardness after aging	41-43 RC

Table 5.3 Hardening response of Infiltrated Bimodal TiC Samples

5.2.3.3 Dimensional Change after Infiltration

With an appropriate infiltrant identified, the next step was quantifying the dimensional change that would occur due to the infiltration step. This was done in a similar manner to the shrinkage experiments previously performed with 4 mil silicon carbide pins embedded in bimodal TiC-TiC compacts. The experiments were performed at 1120°C in a forming gas atmosphere. The results are summarized in table 5.4.

Sample #	Recorded Expansion (4 measurements/sample)	**Average Expansion +/- error**
A	0.24%	0.2% +/- 0.1%
	0.12%	
	0.32%	
	0.08%	
B	-0.04%	0.1% +/- 0.1%
	0.09%	
	0.17%	
	0.04%	
C	0.20%	0.3% +/- 0.1%
	0.28%	
	0.36%	
	0.32%	

Table 5.4 Expansion results for bimodal TiC compacts infiltrated at 1120C for ½ hr

Taking into account the shrinkage experienced by the samples after sintering (Table 5.1), the net dimensional change experienced by the Bimodal TiC samples was 0.2%.

5.3 420 or 316L Stainless Steel – Titanium Carbide Systems

5.3.1 Sintering TiC and Stainless Steel Powders

The key issue to be determined prior to conducting any sintering experiments with TiC and Stainless Steel was the degree of chemical interaction between the powders at high temperature. It was hoped that there would be negligible reactivity in order to minimize the shrinkage. Therefore, a phase diagram was generated using a thermodynamic simulation package (see Figure 5.9).

The phase diagrams indicated no depletion of the concentration of pure Titanium Carbide in the composite up to a temperature of 1400 °C. This essentially established an upper bound on the sintering temperature.

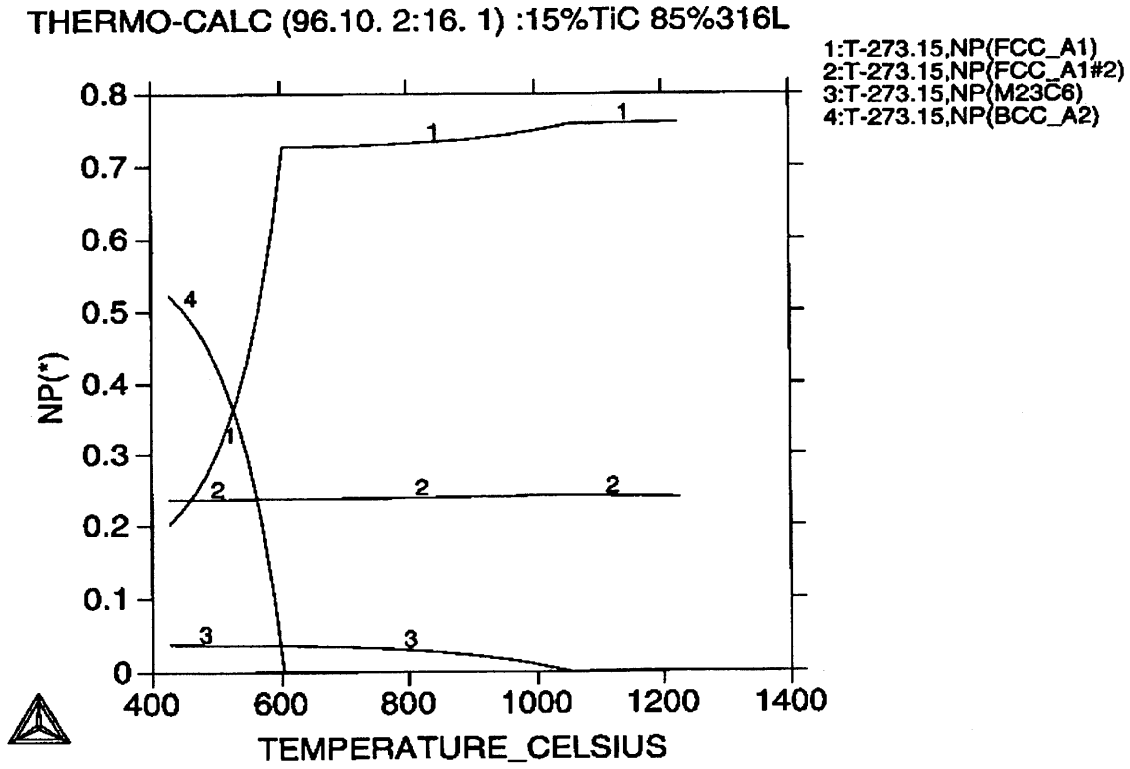

Figure 5.9 Computer Generated phase diagram for Stainless Steel and Titanium Carbide.

With this as a guide, a series of sintering experiments were performed using 15/85 (by wt. %) TiC-Steel cast samples to determine the minimum temperature necessary to create a strong compact. Strength was gauged qualitatively by ultrasonicating the sample to see if it wore away or came apart. All experiments were performed in a forming gas atmosphere, a ramp rate of 5°C/min, and 45 minute holds at temperature. Beginning at 1150°C and increasing by 25 degree intervals, 1250°C was quickly established as the minimum temperature for satisfactory strength of the SS-TiC skeleton. SEM images of the cross sections confirmed the necking behavior between the large Stainless-Steel powders (See figure 5.10).

As expected, the fine TiC powders do sinter to each other, but not noticeably to the large steel powders. They appear to be physically "trapped" at the necks as the Stainless Steel powders sinter around them. This tendency to inhibit sintering between larger powders

had previously been seen by Yoo with Iron Carbonyl-TiC co-dispersions printed into Stainless Steel (73-85).

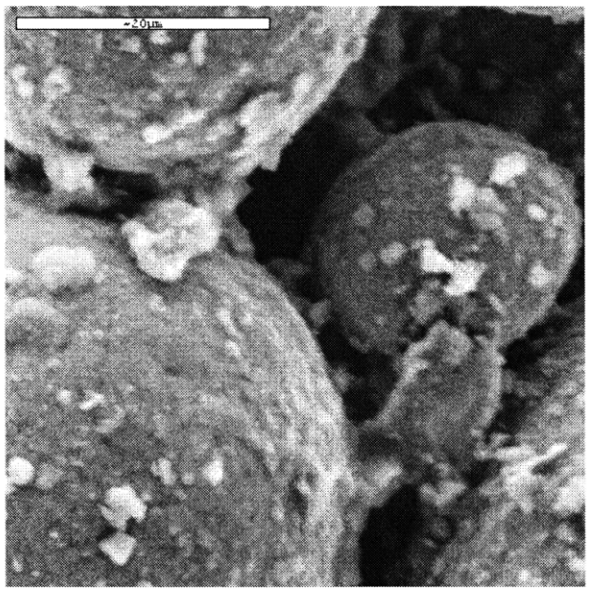

Figure 5.10 316L-TiC necks (20 micron Scale bar). Sample Fired at 1250C for 45 minutes.

5.3.1.1 Dimensional Change after sintering

Once the sintering recipe had been determined, it was necessary to quantify the shrinkage of cast samples due to the heat treatment. Using the trusty technique of embedding tiny silicon carbide wire posts into a sample (See Section 3.1.2), data was collected for samples fired at 1250°C for 45 minutes. These experiments were conducted at varying concentrations of Titanium carbide. The data is presented in figure 5.11.

The results of the shrinkage seemed to indicate that the fine TiC particles, at low concentration, had the effect of inhibiting shrinkage. However, at higher concentration, the fine TiC particles increased the shrinkage. The interpretation was that at higher concentrations, the TiC particles, because they sintered more readily with each other than the Stainless Steel powders, now had a dense enough concentration and enough particle contacts to draw the Stainless Steel powders inward. Though this result was not quite encouraging, the magnitude of the shrinkage was on par with the shrinkage experienced by the traditional 316L or 420 Stainless Steel 3DP material system (typically 1-2%).

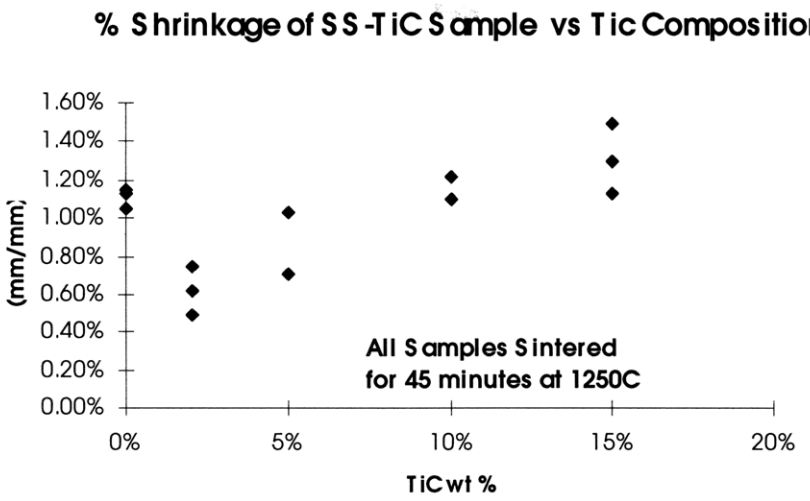

Figure 5.11 316L SS – TiC Shrinkage as a function of TiC Concentration

5.3.2 Infiltration of TiC-Steel Composites

The first attempts at infiltrating sintered Steel-TiC compacts were with the usual 3DP copper-tin infiltrant. The process conditions were dutifully duplicated, i.e. 30 minutes at 1150°C. These early trails met with little success. The problem was largely due to poor wetting of the TiC portion of the matrix by the infiltrant. Frequently, the infiltrant would not penetrate the Steel-Tic compacts and merely coat the surface. SEM imaging of the composites that had been partially infiltrated illustrated the problem quite readily, with voids evident in the darker, Titanium Carbide rich regions (Figure 5.12)
The wetting problem was further highlighted during infiltration experiments with porous TiC compacts. The copper-tin alloy failed to wet the TiC compacts (See Table 5.2).

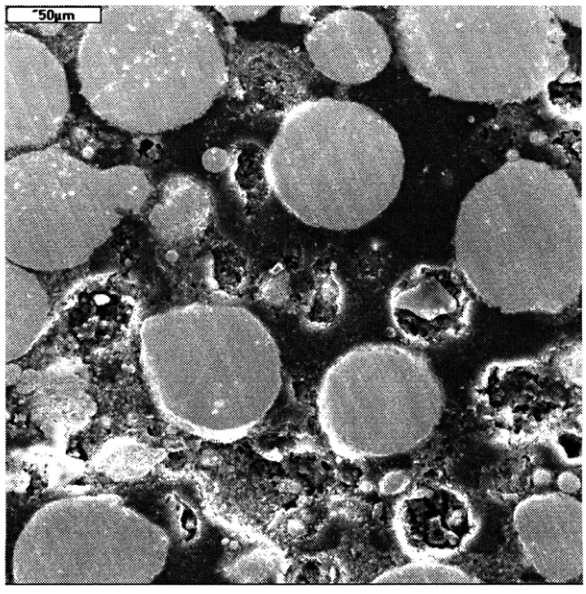

Figure 5.12 Poor Cu-Sn infiltration of 316L-TiC compact

Therefore, a new infiltrant was sought. Experiments were then conducted with candidate infiltrants suggested by literature and some industry representatives (Ed Oles, Personal Communication). A summary of the work is provided below.

Copper alloy	Wets Matrix (Y/N)	Infiltrates Matrix (Y/N)	Temp. (°C)	Comments
Cu-20Mn-20Ni Alloy	Yes	No	1120	Infiltration stopped halfway through compact.
53Cu-15Ni-24Mn-8Zn-trace	Yes	Yes	1150	
Cu-24Ni-24Mn-2Zn	Yes	Yes	1150	
Cu-20Mn-10Sn	Yes	Yes	1200	

Table 5.5 SS-TiC Infiltration experiments

Buoyed by the success of having three successful infiltrants, further work was performed with the Cu-Ni-Mn alloy that wet the compact but failed to fully infiltrate. Due to the age hardening properties of the alloy, it was more desirous as an infiltrant. The alloy could be hardened simply by a low temperature heat treatment for 12 hours at 400°C, without any quenching. This sort of hardening (without quenching) minimized dimensional changes. Following a suggestion that had been made by a fellow group member to attempt the infiltration at a higher temperature (Zubin Irani, Personal communication), success was achieved. Irani believed that some form of solidification was occurring at the interface to inhibit infiltration. Moving to a temperature of 1200°C eliminated any possibility of infiltrant solidification and produced excellent results (See figure 5.13).
Unfortunately, no age hardening response was recorded after the samples were heat-treated. The Macro-hardness of the composite remained at approximately 80 and 84 Rockwell B for the 316L and 420 SS infiltrated systems respectively. The likely culprit for the lack of hardening behavior is the diffusion of nickel into the Stainless Steel – TiC skeleton. Any depletion of the nickel concentration in the infiltrant would ensure a softer system upon age hardening. This is because the hardening effect in the infiltrant was the

consequence of an ordering reaction that formed a hard Mn-Ni phase (Guo, 50-51). This depletion of nickel had previously been seen by Guo, in his work with 420 SS and Cu-Ni-Mn (60-61).

In addition to the lack of hardenability of the composite, there were a few unexplained regions in the samples, that were devoid of fine TiC particles. One such region is highlighted in figure 5.13.

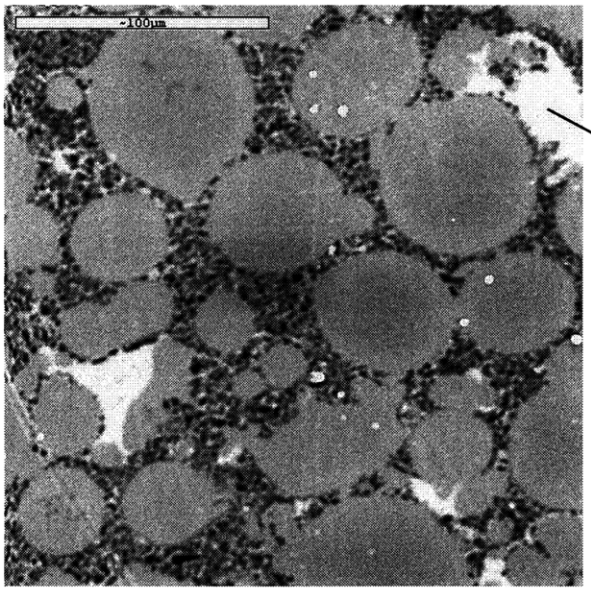

Figure 5.13 420 SS–TiC infiltrated with Cu-Ni-Mn (100 micron Scale bar)

5.4 Molybdenum–Titanium Carbide systems

5.4.1 Sintering TiC and Molybdenum Powders

As with the Stainless Steel-TiC systems, the first order of business was getting a sense apriori of the chemical interaction between Molybdenum and Titanium carbide at high temperature. As before, a phase diagram was constructed for this purpose (See figure 5.14). The phase diagram indicated minimal reaction between the TiC and Molybdenum, illustrated by the fairly constant concentration of the BCC Molybdenum phase.

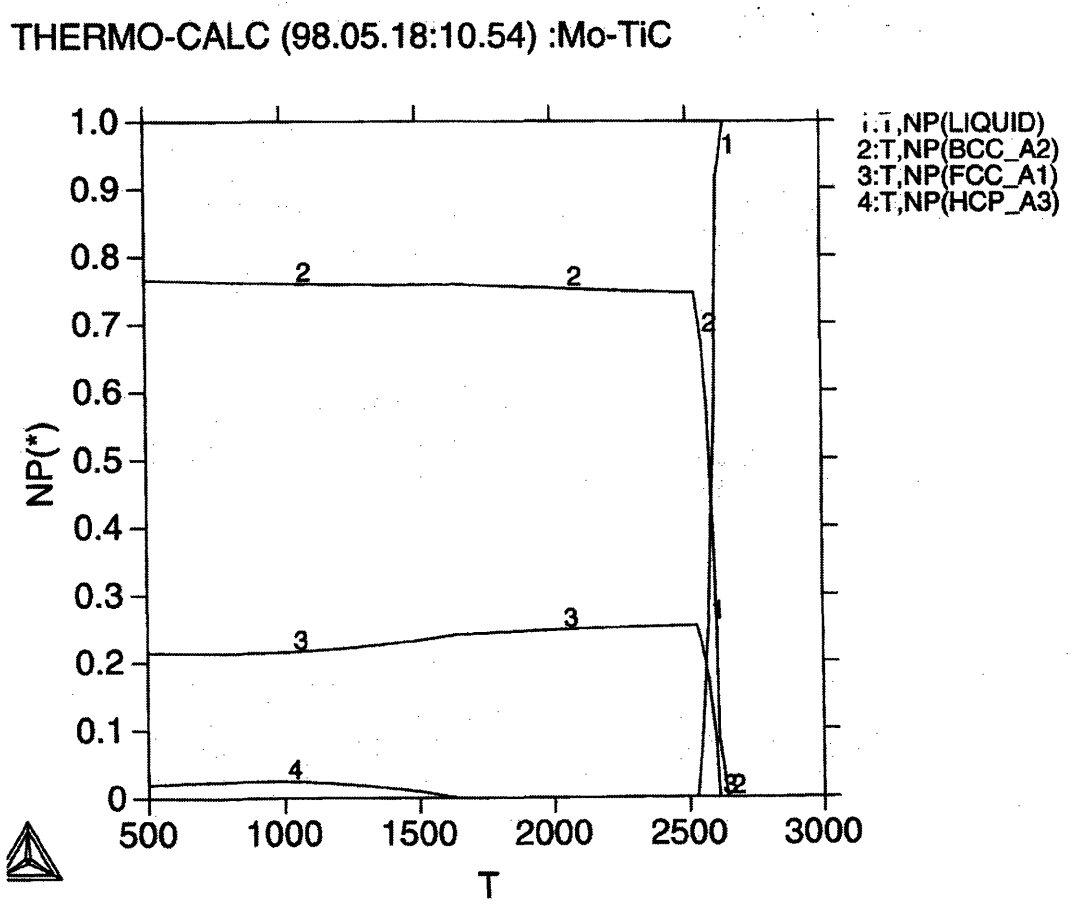

Figure 5.14 Molybdenum-TiC Phase diagram (85/15 wt %), Temperature axis is in Kelvin. Courtesy Zubin Irani.

Sintering experiments were then performed to determine the minimum temperature necessary to produce a compact that would survive infiltration. Again, this was assessed qualitatively and equated to whether or not the sample would remain intact during ultrasonication. Using cast samples (15 wt. % TiC, 85 wt. % Molybdenum), experiments were performed first at 1250 °C, and later at 1300 °C for 45 minutes.1300°C proved to be the appropriate temperature for adequate strength. Rigorous shrinkage test were not performed with the Molybdenum-TiC samples, because no shrinkage was visually apparent. After sintering, the samples did not pull away from the walls of the crucible, indicating minimal shrinkage. A representative SEM of a fracture surface of the composite is provided below (See figure 5.15).

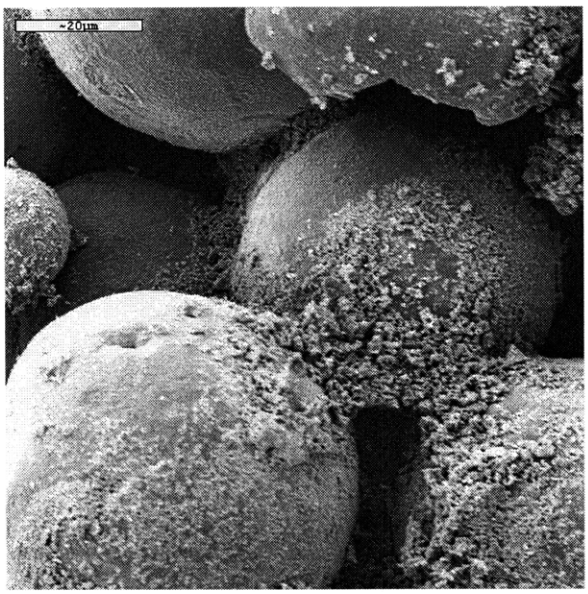

Figure 5.15 Sintered Molybdenum-TiC Sample (20 micron scale bar).

5.4.2 Infiltration of TiC-Molybdenum Composites

Based on experience with the Stainless Steel-TiC, and the desire for age-hardenability, the copper-nickel-manganese alloy was selected for infiltration experiments. Initial experiments were conducted in a forming gas atmosphere at 1120°C for 30 minutes. As with the Stainless Steel-TiC compacts, the Cu-Ni-Mn alloy wet the surface of the Molybdenum-TiC compact but failed to significantly penetrate it. These "infiltration barrier" phenomena had been overcome in the previous Stainless Steel-TiC case by raising the infiltration temperature to 1200 °C for 30 minutes. Repeating this technique provided similarly stellar results for the Molybdenum-TiC system (see Figure 5.16).

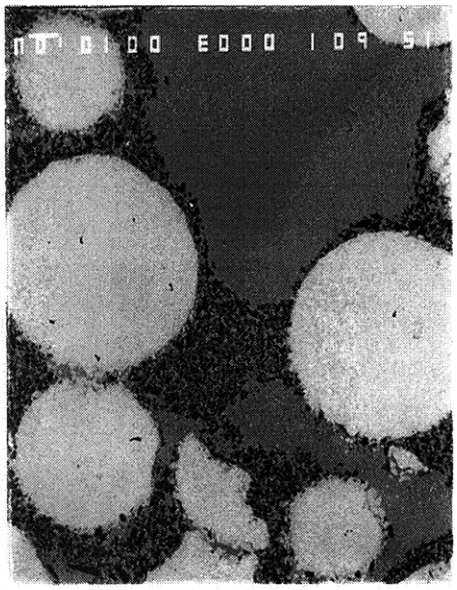

Figure 5.16 Micrograph of Molybdenum-TiC infiltrated with Cu-Ni-Mn (600x Magnification).

5.4.3 Evaluation of Interaction between composite phases.

Despite the success of the infiltration at 1200°C, there was still the unanswered question of why the Cu-Ni-Mn failed to infiltrate the porous compact at the lower temperature and yet still demonstrated excellent wetting properties. Two possible causes for the "infiltration stop" phenomena had been postulated. The first possibility was the formation of thin oxide layer/skin on the liquid infiltrant that formed a physical barrier that had to be overcome. At a higher temperature, the skin could be thinner due to a less viscous infiltrant or more likely, be present in a significantly lower concentration because of the increased propensity for the oxides to be reduced by the forming gas atmosphere. The second possibility had to do with the solubility of Molybdenum in the liquid infiltrant, even a slight solubility would raise the infiltrant's melting point above 1120°C. The infiltrant would then solidify on the surface and fail to penetrate. To see if indeed the latter was a credible cause of the infiltration barrier phenomenon, microprobe analysis was performed on the Molybdenum-TiC samples infiltrated with Cu-Ni-Mn. The purpose of this analysis was to measure the constituent concentrations at the various points in the sample and discern if any significant interactions had occurred between Molybdenum and the infiltrant. The results are documented in Table 5.4, along with the associated probe location within the sample.

	Nickel	Copper	Manganese	Molybdenum	Titanium	Carbon
Bulk Infiltrant Rich Region	23.6	54.1	21.9	0.06	0.17	0
Interface of Infiltrant-Molybdenum-TiC	20.0	58.1	20.3	0.09	0.26	1.1
1 micron into a Molybdenum Powder Particle	0.6	1.7	0.5	96.8	0.26	0

Table 5.6 Atomic % of elements in infiltrated Molybdenum-TiC at various locations

The results of Table 5.4, indicate minimal reactivity between Molybdenum and the infiltrant, and seem to point away from the infiltrant solidification argument. This interpretation stems from the negligible amount of infiltrant approximately 1 micron into the Molybdenum particle and the correspondingly insignificant amount of Molybdenum in the bulk infiltrant region.

5.4.4 Age Hardening Response of Infiltrated Molybdenum-TiC composites.

As with the bimodal TiC system, the benefit of using copper-nickel-manganese as an infiltrant, was its age hardening property. Following a 12 hour heat treatment at 400°C in a forming gas atmosphere, the following Macro hardness data was recorded (Table 5.5).

Macro Hardness after Infiltration	85-90 RB
Macro Hardness after aging	23-25 RC

Table 5.7 Hardening response of Infiltrated Molybdenum-TiC Samples

5.5 Summary

The development of three materials systems is described in chapter 5. Each system utilizes a Cu-Ni-Mn alloy as an infiltrant. The first system, a bimodal system of large TiC and fine TiC powders, exhibits good dimensional control (net shrinkage of 0.2%) and age-hardening properties. The second system, a bimodal system of large Stainless Steel and fine TiC powders, is characterized by modest dimensional control (less than 2%) but failed to exhibit similar hardening behavior. The third system developed, large Molybdenum powders and fine TiC powders, displayed similar hardening behavior to the bimodal TiC system.

Chapter 6: Conclusions

6.1 Summary of work

The important contribution of this work has been to identify a technique by which defect free, high density bimodal parts can be fabricated using the Three Dimensional Printing Process. In this method, fine powder slurries are printed into a bed of large powders to fill the voids and form a dense bimodal green part (See figure 6.1).

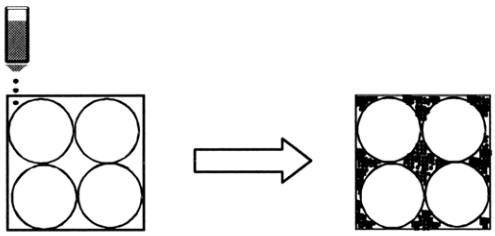

Figure 6.1 Slurry Printing bimodal densification mechanism

This technique of bimodal densification via slurry printing was demonstrated by printing a 20 volume fraction slurry of sub-micron Titanium Carbide powders into a bed of large Molybdenum powders (52 micron avg.). To ensure the uniformity of the microstructure, thinner layers were spread (4 and 5 mils) and multiple application printing was employed, i.e. double printing. As a result, sample coupons with estimated green densities of up to 83% were obtained.

In addition, attempts have been made to answer the questions raised at the beginning of this investigation (See Section 1.4.2) associated with printing slurries into powder beds.

6.1.1 Slurry Development

Two stable dispersions of Titanium Carbide powders were developed in the course of this work. A formulation containing a binder, and a binder free formulation. The slurries were

characterized by a settling rates of less than 0.1mm/hr, and viscosities of less than 10 centipoise. In addition, the suitability of the TiC slurries for printing was summarily investigated, with the removal of agglomerates larger than 10 microns established as a necessary condition for stable break-off and droplet generation.

6.1.2 Deposition Pattern and its Effect on Infiltration

Observations about the deposition pattern of fine particles were used to answer the questions posed at the beginning of this work about infiltrating bimodals and possible pitfalls. The primary observation made was that fine powders gather preferentially at the necks of the large powders and tend to coat the surfaces of the large powders when printed. Preferential deposition can have an adverse effect on post-sintering infiltrations performed in gas atmospheres. Frequently, fine porosity was observed at interface regions between large and fine powder clusters, and at interfaces of infiltrant and fine powder clusters. The cause of this porosity was identified as a trapped gas phenomenon caused by differing infiltration rates within the bimodal compact. This was determined after a comparison between samples infiltrated under vacuum conditions and in a forming gas atmosphere. The vacuum infiltrated samples failed to exhibit similar patterns of porosity.

In addition, the effects of different bimodal concentrations and size ratios on porosity were explored under vacuum conditions with two bimodal-infiltrant systems (WC and Cu, TiC and Cu-Ni-Mn). The TiC samples failed to exhibit any appreciable variation in porosity levels due to changes in size ratio or concentration. The WC samples demonstrated slightly higher porosity when the bimodal size ratio was large, but no link was established between porosity and the concentration of the bimodal constituents.

6.1.3 Effect of Fine Powders on Sintering and Shrinkage.

To answer the question posed in the introduction regarding the sintering effects associated with having fine, relatively inert powders at the necks between the large base powders, shrinkage data from the Stainless Steel – TiC system was drawn upon (Figure 5.11). The results indicate that an initial reduction in shrinkage should be expected at low, fine powder concentrations, but as the concentration of fine powders increases, the shrinkage also increases. This added shrinkage is caused by the fine powders sintering more readily to each other, and pulling the larger particles together. At low concentration, the inert particles, mainly in contact with the large powders, act as shrinkage inhibitors.

6.1.4 Selection of Process Parameters for a Uniform Microstructure.

Another question posed in section 1.4.2 had to do with the manner in which printing should be undertaken for a uniform, defect free microstructure, i.e. randomly distributed fine powders in a matrix of larger powders, to result. To ensure this, two types of defects had to be avoided. The first defect had to do with the slurry penetration depth and the layer thickness. If the layer thickness was not smaller than the slurry penetration depth, periodicity would result in the final part. The TiC powders would then be deposited in equidistantly spaced bands within the part. An example is provided in figure 6.2.

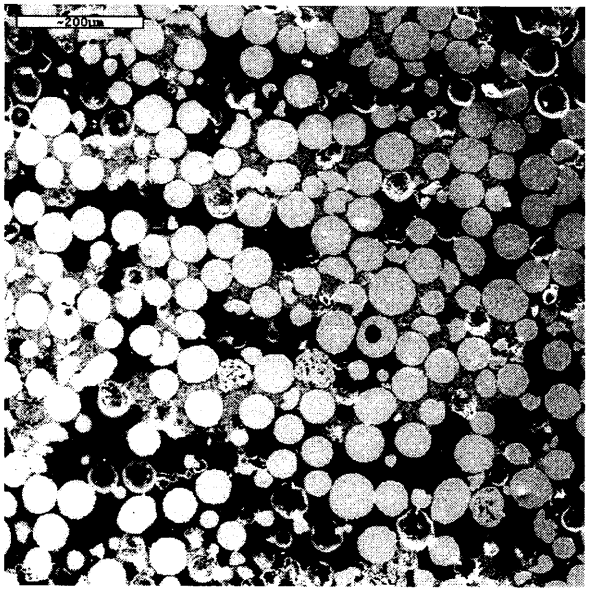

Figure 6.2 Section of Molybdenum-TiC infiltrated with epoxy. 7 mil layer thickness, 172 micron line spacing, double print. (200 micron scale bar)

The second type of defect, is the interlayer defect. An interlayer defect is the absence of large powder particles at the interface between two adjacent layers. These defects had been seen by Gregorski, in his work with spreading and compacting bimodal powders. An example of this is shown in figure 6.3.

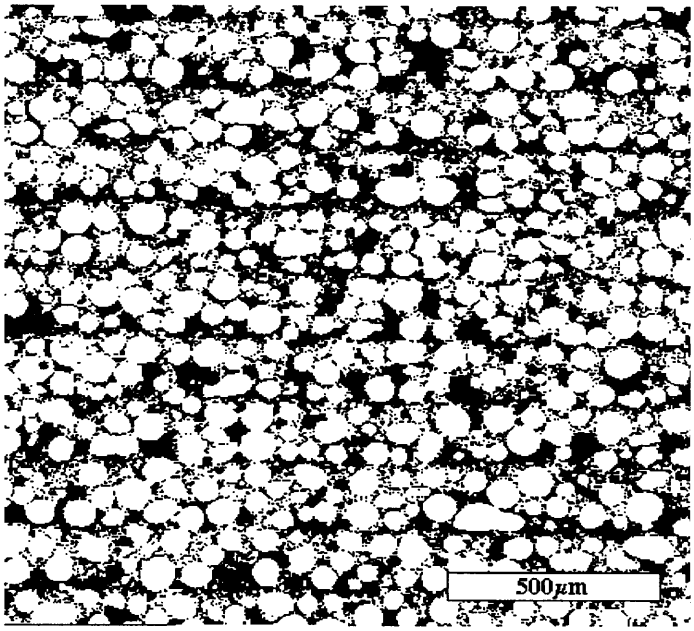

Figure 6.3 Microstructure of 71/9 µm printed bimodal baseline sample. (Courtesy: Steve Gregorski, 40).

This condition could be avoided if the fine printed powders did not remain at layer surface, i.e. slip cast, and instead penetrated into the layer.

To avoid these two defects, systematic experimentation was undertaken with thinner layers and different dosages (single vs. double printing). The resulting microstructures were examined for evidence of periodicity and fine TiC powders at the surface of the parts. Success was attained when process conditions that resulted in defect free samples were identified. Figure 6.4 a, b are images of a defect free sample.

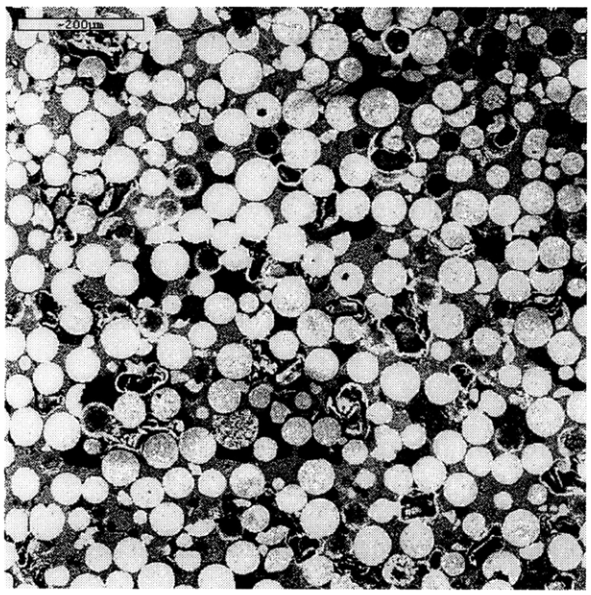

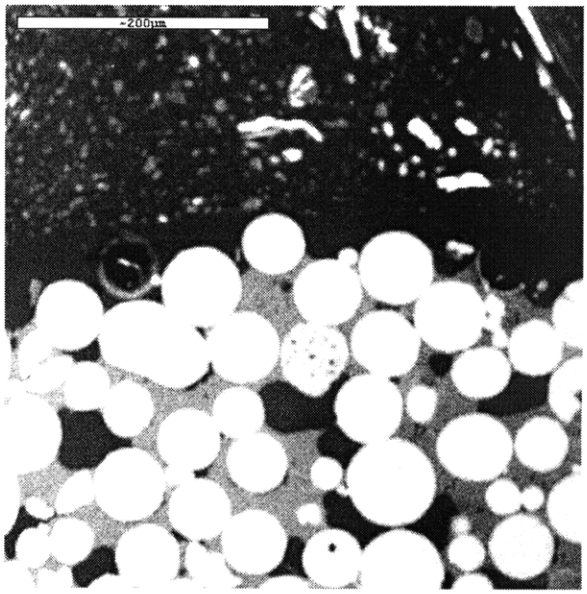

Figure 6.4 a) 4 mil, Double Printed Molybdenum-TiC Section; 200 micron scale bar.

b) Top Surface of 4 mil, Double Printed Molybdenum-TiC Section; 200 microns scale bar.

A few words about some other printing parameters such as multiple printing vs. single printing and drying. If thinner layers are spread, multiple prints do not appear to have significant advantages over single prints when it comes to obtaining a defect free structure (i.e. less interlayer defects or stratification). Its main benefit is to deposit more material and move you closer to the 86% bimodal green density limit. Samples close to the limit will however demonstrate the most uniformity just because no more material could possibly be added. If one can get to the bimodal limit in a single application, it

would suffice. Drying is also necessary between multiple applications as it maximizes the available volume for the freshly printed volume to occupy.

6.1.5 Material System Development

To fully take advantage of the capability to deposit fine Titanium Carbide particles in a powder bed, three materials systems were concurrently developed. Each system utilized a Cu-Ni-Mn alloy as an infiltrant, with different age-hardening properties. Age-hardening in this case involves a temperature treatment at 400 °C for 12 hours. The first system, a bimodal system of large TiC and fine TiC powders, exhibits good dimensional control (net shrinkage of 0.2%) and age-hardening properties (up to 43 HRC). The second system, a bimodal system of large Stainless Steel and fine TiC powders, is characterized by modest dimensional control (less than 2%), but does not exhibit any age-hardening behavior. The third system developed, a bimodal system of large Molybdenum powders and fine TiC powders, can be hardened up to 25 HRC with a 12 hour, 400 °C treatment.

6.1.6 Binding the Part: sintering fines vs. additional binding agent.

A final question left unanswered, is whether or not to incorporate an additional binding agent into the dispersion of fine powders as opposed to sintering the fine powders to hold the compact together (if possible). Both mechanisms were explored in this work, with the bimodal TiC-TiC system an example of the latter, while the bimodal Molybdenum-TiC is an example of the former. There seems to be little difference between the two in terms of the deposition trends, i.e. fine powders still gather at the necks, etc. The main argument for the sintering of fines approach, is the difficulty associated with formulating a stable co-dispersion (dispersant and binder). This route could easily be a lengthy undertaking. Instead, analogous situations to the Bimodal TiC-TiC systems should be sought. The only obstacle is the fine powder availability of the material in question (sub-micron is preferred). Sub-micron powders are necessary for an appropriate temperature cushion before the larger base powders begin to sinter and alter the previously defined geometry.

6.2 Recommendations for Future Work

To fully develop the capability to fabricate high density bimodal parts with TiC, work must be pursued on three fronts. The first front is the development of a reliable fluid system for delivering slurries to the nozzle without the bubbling phenomenon observed during this work. The second avenue of pursuit is increasing the maximum part build size when thin layers are being spread. This limitation is primarily due to the inability of some large powders to effectively compact to the thin layer size. An easy means of overcoming this obstacle is moving to a slightly finer, "large" powder that would readily compact to allow for thinner layers to be spread. Other possibilities include, using slower roller traverse rates and higher vibration frequencies while spreading the large powders. Preliminary work using slower traverse rates (0.005 m/s instead of 0.05 m/s) did not yield improved results however. The third avenue of pursuit is attempting to achieve the same multiple layer penetration effects at the standard, 7 mil layer thickness. This was briefly explored and may need to be revisited if thinner layers are unable to be spread. To do this, higher flow rates are necessary to compensate for the larger layer size.

REFERENCES

Baker, Peter J. "Three Dimensional Printing of Fine Metal Powders", MS thesis, Massachusetts Institute of Technology, Cambridge, 1997.

Barnes, H., Holbrook, S.: "High concentration suspensions: preparation and properties." *Processing of Solid-Liquid Suspensions.* P. Shamlou (Ed.) London: Butterworth-Heinenmann Ltd., 1993. 231-245.

Caradonna, Michael A.: "The Fabrication of High Packing Density Ceramic Powder Beds for the Three Dimensional Printing Process," MS thesis, Massachusetts Institute of Technology, Cambridge, 1997.

Chermant, J. L. "Sintering and Grain Growth in Titanium Carbide." *Science of Sintering.* Vol. 12, n 3

Chijioke, Akobuije. Personal Communication, March 1998.

Eremenko, B.V., Malysheva, M.L., Sambur, V.P.: "Stability of dispersions of Titanium Carbide micropowders in aqueous solutions of polyoxyethlene in the presence of Electrolytes". *Colloid Journal of the USSR.* Vol. 51 n1 Jan-Feb (1989). 23–30.

Fan, Tailin: "Droplet – Powder Impact Interaction in Three Dimensional Printing," Ph.D. thesis, Massachusetts Institute of Technology, Cambridge, 1995.

German, Randall M.: *Powder Metallurgy Science.* Metal Powder Industries Federation. Princeton, NJ, 1984.

Goetzel, Claus: "Infiltration", *Metals Handbook Ninth Edition,* Powder Metallurgy, vol. 7, American Society of Metals, Metals Park, OH, 1984.

Gregorski, S.: "High Green Density Metal Parts by Vibrational Compaction of Dry Powder in the Three Dimensional Printing Process," Ph.D. thesis, Massachusetts Institute of Technology, Cambridge, 1996.

Guo, Honglin: "Alloy Design for Three Dimensional Printing of Hardenable Tool Materials," Ph.D. thesis, Massachusetts Institute of Technology, Cambridge, 1998.

Irani, Zubin: MIT Internal Communications. Feb-Apr 1998.

Koch, Stefan: "Preparing and Jetting Highly Loaded Slurries for the Three Dimensional Printing Process." MS thesis, Technischen Hoshschule Aachen & MIT, October, 1997.

Sachs, E. Cima, M., Williams, P., Brancazio, D., Cornie, J.: "Three Dimensional Printing: Rapid Tooling and Prototypes Directly form a CAD Model," *Journal of Engineering for Industry*, Vol. 114, Nov. 1992, pp. 481-488.

Serdy, J.: Personal Communication, June 1997.

Washburn, Edward W.: "The dynamics of capillary flow." *The Physical Review, 2nd Series*, Vol. 17 (1921). 273-283.

Yoo, Helen J.: "Reactive Binders for Metal Parts Produced by Three Dimensional Printing," MS thesis, Massachusetts Institute of Technology, Cambridge, 1997.

Appendix A: Powder Database and Sources

420 Stainless Steel

Shape: Spherical

Size: –170/+325

Manufacturer: Anval

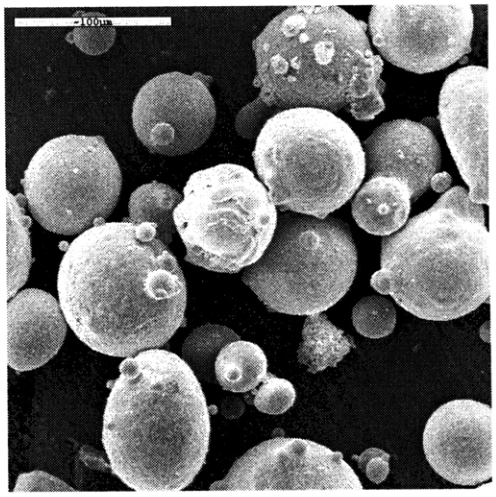

Titanium Carbide

Shape: Coarse

Size(s): 0.8 - 1 micron

Manufacturer: Kennametal

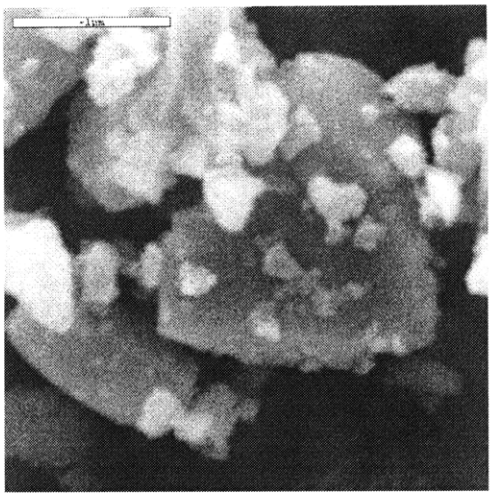

Molybdenum

Size: 52 micron avg.

Shape: Spherical

Manufacturer: Osram Sylvania

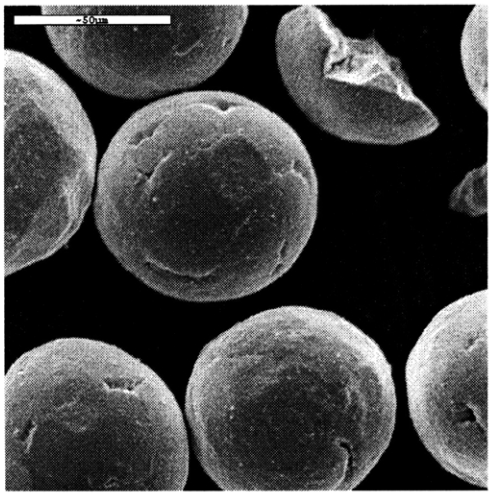

Other Powders used:

316L Stainless Steel

Shape: Spherical

Size: –80/+325 Mesh

Manufacturer: Anval

Titanium Carbide(s)

Shape: Coarse

Size(s): 74-105 microns

Manufacturer: Kennametal

Shape: Coarse

Size: -325 mesh, typically 10 microns.

Manufacturer: Cerac

Tungsten Carbide(s)

Shape: Coarse

Size: 0.8 micron avg.

Manufacturer: Valenite

Shape: Coarse

Size: 10 micron avg.

Manufacturer: Kennametal

Shape: Coarse

Size: 70 micron avg.

Manufacturer: Cerac

Appendix B: Generating sintering maps to predict shrinkage.

B.1 Background and Method

As discussed in Chapter 5, sintering can be broken up into three stages based upon the degree of neck formation and pore characteristics. An initial stage, an intermediate stage, and a final stage. The parameter used to separate these stages, is the neck to particle size ratio (see figure B.1)

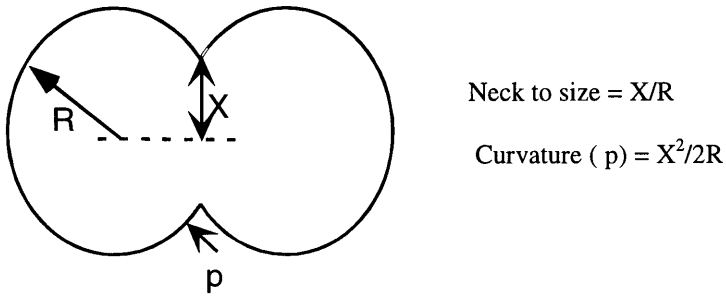

Figure B.1 Illustration of Sintering with key geometric relations

The initial stage is dominated by interconnecting pores and a neck size ratio of less than 0.3, while the intermediate and final stages are characterized by cylindrical and circular pore structures with the neck size ratio increasing.

In the initial stage, sintering is usually modeled as an isothermal process, with several diffusion mechanisms acting in concert. The contribution from these mechanisms, surface diffusion, bulk diffusion, etc. can be expressed as a sum of terms that contribute to the neck size ratio:

$$\sum \frac{X}{D} = \left(\frac{X}{D}\right)_{\substack{Surface \\ Diffusion}} + \left(\frac{X}{D}\right)_{\substack{Volume \\ Diffussion}} + \ldots \qquad \text{B.1}$$

These terms, each vary with the holding time (t), particle radius (R), and mechanism specific exponents (m, n):

$$\left(\frac{X}{R}\right)^n = \frac{Bt}{R^m} \qquad \text{B.2}$$

The parameter (B), depends on the diffusion constant of the sintering mechanism under consideration (which varies exponentially with temperature), and various constants relating to the mechanism. Using surface diffusion as an example, the parameter for surface diffusion (B_s) and the associated diffusion constant (D_s) would vary as shown below,

$$B = 56\, D_s \gamma \Omega^{4/3}\, kT \qquad \text{B.3}$$

$$D_s = A_s \exp(-Q_s/RT) \qquad \text{B.4}$$

Where γ, Ω, A_s , Q_s are the surface energy, atomic volume, frequency factor and activation energy for surface diffusion, respectively. The symbols R, k, T refer to the Gas constant, Boltzman's constant, and temperature.

Once the individual contributions to the neck growth have been accounted for and combined (typically in a spreadsheet), the next leap is to predict the shrinkage. German (PM Science,252), has presented an approximate relationship between the neck size ratio, and the shrinkage:

$$\Delta L/L_o = (X/R)^2 \qquad \text{B.5}$$

This relationship can then be used as a guide in selecting time and temperature cycles for sintering and shrinkage experiments.

A summary listing of the appropriate relations to use for the different sintering mechanisms is presented in Table B.1 (German, 251):

Sintering Mechanism	**Diffusion Constant**	**B**	**N**	**m**
Surface Diffusion	$D_s = A_s \exp(-Q_s/RT)$	$56\, D_s\gamma\Omega^{4/3}\, kT$	7	4
Volume Diffusion	$D_v = A_v \exp(-Q_v/RT)$	$80\, D_v\gamma\Omega/kT$	5	3
Grain Boundary Diffusion	$D_{gb} = A_{gb} \exp(-Q_{gb}/RT)$	$56\, D_{gb}E_{gb}\,\Omega/kT$	6	4
Plastic Diffusion	$D_p = A_p \exp(-Q_v/RT)$	$9\pi\gamma bD_v\Omega/kT$	2	1

Table B.1 Relevant relationships for each Sintering mechanism.

Material property data used to generate the sintering and shrinkage plots in Chapter 5 is also listed in Table B.2 (Chermant, et al., 172)

Name	Symbol	Value	Units
Atomic Volume	Ω	2×10^{-29}	m^3
Burgers vector	b	3×10^{-10}	m
Density	ρ	4.940	Kg/m^3
Shear Modulus at 300K	G	1.92×10^{11}	Mn/m^2
Temperature dependence of shear Modulus	-	1.60×10^{-1}	-
Melting Temperature	T_m	3212	K
Grain Boundary Energy	E_{gb}	0.5	J/m^2
Surface energy	γ_s	1.19	J/m^2
Pre-exponential term for volume diffusion	A_v	4.4	m^2/s
Activation energy for volume diffusion	Q_v	737.4×10^3	J/mole
Pre-exponential term for Boundary diffusion	A_{gb}	9.6×10^{-14}	m^3/s
Activation energy for Boundary diffusion	Q_{gb}	543.4×10^3	J/mole
Pre-exponential term for surface diffusion	A_s	6×10^{-14}	m^3/s
Activation energy for surface diffusion	Q_S	288.4	KJ/mole

Table B.2 Material Property data for Titanium Carbide.